Faculté des Sciences
Département de Physique - Unité de recherche CESAM
Group for Research and Applications in Statistical Physics

How grooves control droplet growth, transport and release

Dissertation présentée par

Matteo Leonard

en vue de l'obtention du titre de

Docteur en Sciences

Université de Liège
Année académique 2025-2026

Acknowledgments

First of all, I would like to warmly thank all members of the jury who took the time to read this work: Pr Bastin, Pr Bico, Pr Brau, Pr Carlson, Pr Dreesen, and Pr Vandewalle. I hope you will enjoy it.

Ensuite, j'aimerais remercier Jeff (et Valsem Industries SAS) pour avoir financé cette thèse (évidemment!) mais surtout pour avoir cru en moi et m'avoir poussé toujours plus dans mes réflexions personnelles. J'ai énormément appris à ses côtés et ai découvert le monde de l'entreprise, mais surtout, et à une échelle plus humaine, celui d'une usine. Quel grand écart avec le contexte abstrait de l'université qui m'entoure depuis plus de 10 ans. Je le remercie d'autant plus qu'il m'a entouré de personnes de qualité dans ma tâche.

Au premier rang de celles-ci, Daniel, à qui je dois une grande partie de mes connaissances sur la condensation, que ce soit au travers de mes échanges réguliers avec lui ou au travers du livre qu'il a écrit, *Dew Water*. J'ai découvert une personne pleine de curiosité, mais également très généreuse, qui a toujours su interroger mes résultats pour en approfondir la compréhension.

Vient ensuite Raphaël, qui m'a introduit à la structuration de projet. J'ai, petit à petit, au fil des réunions avec lui, appris à m'extirper du labo pour tenter de transformer un résultat en un produit. Le chemin s'est révélé long, semé d'inconnues et s'éloignant petit à petit de l'objectif initial. Malgré tout, j'ai appris la méthode et la résilience à ses côtés.

Finalement, je remercie Fred, sans qui beaucoup de discussions ne seraient peut-être pas retombées sur Terre. Son aspect pratique et concret nous a continuellement poussés à respecter les contraintes et à garder l'objectif dans le viseur.

Revenons à l'Uliège à présent, j'aimerais remercier mon directeur de thèse, M. Vandewalle, pour ses relectures multiples et critiques de mes travaux, ainsi que son appui scientifique et administratif. Je remercie également mes collègues avec qui j'ai partagé de nombreux moments, que ce soit au labo, chez Brico, à Aquagarden ou encore chez le glacier. Je pense évidemment à Megan(t), qui a rayonné de par son côté humain et chaleureux sur le labo, ainsi qu'à Adri, d'apparence un peu en retrait, mais l'œil toujours collé à la lunette, prêt à décocher une bonne blague inattendue. Je remercie également Joséphine, avec qui j'ai eu la chance de collaborer, dont l'optimisme et la bonne humeur ne faisaient jamais défaut. Merci également à Éric et Martial ainsi qu'à la paire du fond: Bédrien et Axel, mais aussi Filip, Fancy Fan, David et Jocelyn.

Si l'on traverse le couloir, je me dois évidemment de remercier tout le personnel de l'atelier. Merci à Med, avec qui j'ai affronté un nombre incommensurable de problèmes et défis techniques. Merci de m'avoir fait découvrir ton monde, il était difficile pour moi d'entrer dans ton bureau sans t'interroger avec curiosité sur l'une ou l'autre chose qui s'y trouvaient. Tu m'as fait prendre conscience que la solution à mon problème existe probablement déjà, simplement dans un domaine que je

n'aurais jamais envisagé de prime abord. Merci également à Sam pour sa patience à mon égard, la qualité de ses réalisations, ainsi que sa connaissance des industries aux alentours. Merci également à Chouaib, avec qui j'ai discuté de nombreuses heures de sport, ainsi qu'à Michel.

Si l'on continue la promenade à l'étage, je ne peux/veux pas oublier Stéphane! Ça a été un réel plaisir d'échanger avec toi. Je rentrais systématiquement dans ton bureau avec des idées aussi bouillonnantes que désordonnées et j'en sortais avec toujours plus d'idées et encore moins d'ordre. Ton temps, ta patience et ton expertise m'ont été inestimables au cours de ces trois années.

J'en profite également pour remercier Jean-Yves et Hervé avec qui, accompagnés de Steph et Med, j'ai partagé tous mes cafés matinaux. Ces discussions légères et souvent absurdes mettent mieux en jambe que le café lui-même! Merci également à Cyril et Thomas, avec qui j'ai eu quelques conversations sans queue ni tête durant de longues minutes, ainsi qu'à Geoffroy. Si l'on descend de deux étages, merci à tout le personnel administratif pour avoir effectuer un travail discret mais essentiel au bon déroulement de la thèse, merci à Florence, Alexis, Carine et Christine. Si l'on traverse la rue, on trouve certes un emploi mais également Baptiste, Jona et Thomas, et vu le nombre de fois où je me suis incrusté à vos pauses café, je me devais également de vous remercier pour votre accueil.

Flying over the Mediterranean and along the Red Sea, I would like to sincerely thank Tadd and Dilip for their warm welcome during the three weeks I spent at KAUST. What began as an email sent into the void turned into the opportunity to develop one of my secondary experiments, ultimately leading to Chapter 5 of this thesis. Those three weeks were intense and demanding, yet an absolute joy to experience. I discovered a new way of holding meetings, armed with markers and erasers, where questions flew from every direction, where we got lost in obscure calculations, and where everyone gave their best to move the research forward. A special thanks goes to Tadd, who proved to be an exceptional person: thoughtful, kind, and smiling in every situation. I still vividly remember the sunrise stretching over a glassy sea, as well as the sunset framed by the rocky peaks of the desert.

Revenons un instant sur le campus, où j'aimerais prendre le temps de remercier tout particulièrement deux autres personnes. Celles-ci m'accompagnent depuis presque dix ans dans mes aventures universitaires. Il s'agit évidemment du K et du S. Tout d'abord, le K. Je ne compte plus les heures que l'on a passées ensemble, que ce soit à l'unif, au Colruyt, à démonter une machine à café, ou sur un sentier. Pour toutes les fois où tu as accepté de me suivre dans mes délires, que ce soit un projet de méthode numérique ou de phy stat, la présidence du CSP ou une randonnée d'enfer, je me dois bien de le reconnaître: t'es pas net. Si l'on ajoute à cela ta fourberie et ta volonté d'aller à l'encontre des règles établies, je pense qu'on a tout ce qu'il faut pour comprendre notre profonde et tumultueuse amitié. Bien que ce doctorat ait été pour moi un long sprint solitaire, tu étais la personne avec qui je pouvais évacuer la tension au cours d'une course ou d'une aventure. Je t'en remercie.

Le S à présent. Une semaine suffit à résumer la profonde affection que l'on se porte. Une semaine à faire tourner une manip 21 h/24 h, avec un impératif toutes les 50 minutes: relancer la manip. Non seulement tu as été le seul à me pousser à le faire, mais tu m'as aussi accompagné. On a dormi à côté de la manip, dans le vacarme chaotique de la chambre climatique, avec des lumières suspectes qui s'allumaient toutes seules durant la nuit. Cette semaine est le fondement du

Chapitre 3. On a traversé tellement de choses ensemble, tant dans nos vies privées que professionnelles, et tu as toujours été là, que ce soit pour me remettre sur pied, m'encourager ou calmer mes ardeurs. Malgré mon entêtement certain, tu as toujours été capable de trouver les mots qui me permettent d'exprimer le meilleur de moi-même, je mesure la chance de t'avoir rencontré.

Quittons à présent l'université et revenons en secondaire, où s'est formé il y a plus de 15 ans un cercle d'amis. Malgré les aléas, malgré les disputes, malgré la distance, ce cercle s'est adapté et a perduré. On trouve de tout dans le Club, mais surtout des gens sur qui compter, cela suffit pour le rendre inestimable. Parmi eux, j'ai particulièrement apprécié et abusé du temps de deux personnes: Pabz et Doc Denz. Que ce soit pour partager une pizza, venir me dépanner après une aventure un peu trop ambitieuse avec le K ou encore faire monter la rivalité sur une course, on peut être sûr que Doc Denz répond à l'appel, et avec la manière. Si j'hésite, si j'ai besoin d'un (gros) coup de main, ou si je veux juste me détendre sans me prendre la tête, Pabz est toujours partant, avec moins de manières, certes, mais de façon tout à fait efficace! Ces derniers mois auraient été bien différents sans nos petits rendez-vous hebdomadaires, d'abord au café Brazil et ensuite à l'escalade (notez l'amélioration!).

Vient ensuite ma famille: Uouo, Poloss, Mamma et JPC. J'aimerais d'abord m'excuser, j'ai investi énormément de temps et d'énergie dans cette recherche, cela s'est fait à vos dépends. Ce furent trois années où j'étais à cran, peu disponible, dans un roller coaster émotionnel permanent. Je vous remercie de ne pas m'en avoir tenu trop rigueur et d'avoir cherché à m'aider autant que possible. Je tiens à remercier en particulier mon père, qui a su se rendre disponible pour m'aider sur des tâches aussi diverses qu'adapter la chambre climatique, structurer le projet avec Valsem, monter et démonter les manips en extérieur, et surtout pour s'être improvisé chef de chantier dans notre appartement. Dans cette thèse à flux tendu, tous les tracas qu'il a gérés à ma place m'ont permis d'avancer plus sereinement dans ma recherche.

Je clôturerai par Elea. Nos chemins se sont croisés lorsque la tempête s'est levée dans mon esprit, il y a plus de 6 ans. Tu as assisté à mon décrochage en bac3, mon combat contre la culpabilité lors de mes masters, tu as subi de plein fouet mon acharnement dans cette thèse, acharnement d'autant plus croissant que les intérêts de l'Uliège et de Valsem divergeaient. Alors que je bataille à corps perdu contre moi-même, tu te tiens à mes côtés. Soutenir quelqu'un sans pouvoir l'aider, ça demande du courage et de la patience. Alors que tu en es abondamment dotée par nature, je t'ai mise à rude épreuve, je m'en excuse. Ton caractère, quasi parfaitement opposé au mien, m'a permis de trouver un lieu de paix à tes côtés. Qui sait où je serais si l'on s'était simplement frôlés.

Abstract

Water management on surfaces underpins applications ranging from atmospheric water harvesting to heat exchange and surface cleaning. Many existing strategies rely on chemical coatings or micro-texturing, which can be fragile, costly, or difficult to scale. This thesis explores an alternative approach based on simple geometric features, focusing on whether grooves alone can collect, guide, and release small volumes of water on vertical substrates.

We investigate four representative systems that span different flow configurations and degrees of confinement. On fibers and fiber bundles, we show that grooves naturally appearing between strands reorganize droplet dynamics by modifying the film left behind the droplet, reducing dissipation and increasing sliding speed. Under condensation on a vertical plate, we demonstrate that groove spacing selects the drainage pathway: large spacings favor gravitational shedding, while small ones confine droplets to the plateaus and redirect transport into the grooves. At the lower edge of such plates, groove geometry determines the disposition and frequency of droplet dripping. Finally, in a minimal configuration consisting of two parallel grooves, we show that geometry alone can stabilize a thin water film over more than one hundred capillary lengths. At groove termini, the film breaks and releases a droplet through a cyclic sequence of events.

Across these systems, a common principle emerges: groove acts as a minimal feature that structures the flow. Grooves define where liquid accumulates, how it moves, and when it detaches, enabling robust control without coatings or complex fabrication. These findings suggest that simple geometric design can serve as the foundation for scalable, passive, and durable water-handling surfaces, and they outline the key operations needed for a future geometry-driven millifluidic platform.

Résumé

La capacité à contrôler de petites quantités de fluide à la surface des solides est au cœur de nombreuses applications, de la collecte d'eau atmosphérique aux échangeurs thermiques, en passant par les surfaces auto-nettoyantes. Les approches actuelles s'appuient le plus souvent sur des revêtements chimiques ou micro-texturés. Si ces stratégies sont efficaces, elles présentent aussi des limites importantes : elles peuvent être fragiles, coûteuses, sensibles au vieillissement et difficiles à déployer à grande échelle. Cette thèse explore une voie alternative plus robuste. Elle pose une question simple : des motifs géométriques élémentaires, tels que des rainures, peuvent-ils à eux seuls collecter, guider et libérer de l'eau sur des surfaces verticales ?

Pour y répondre, nous étudions quatre systèmes représentatifs couvrant différents régimes d'écoulement et degrés de confinement. Sur des fibres et des faisceaux de fibres, nous montrons que les rainures qui apparaissent naturellement entre les brins modifient la dynamique des gouttes. En piégeant une partie du liquide, elles réduisent la dissipation et augmentent la vitesse des gouttes. Lors de condensation sur une plaque verticale, l'espacement des rainures devient le paramètre de contrôle central. De grands espacements favorisent un drainage dominé par de grosses gouttes. À l'inverse, de petits espacements confinent la croissance des gouttes aux plateaux entre les rainures et redirigent le transport à l'intérieur de la texture, au point de le rendre presque imperceptible en surface. En bas de l'échantillon, au niveau de la tranche inférieure, cette même géométrie fixe la disposition et la fréquence du gouttage. Enfin, dans une configuration minimale composée de deux rainures parallèles, nous montrons que la géométrie seule suffit à stabiliser un film mince vertical d'eau sur plus d'une centaine de longueurs capillaires, puis à déclencher sa rupture et la libération périodique de gouttes selon un cycle bien défini.

Pris ensemble, ces résultats révèlent un principe unificateur. La rainure agit comme un élément géométrique minimal qui structure l'écoulement. Elle définit comment le liquide se déplace, où il s'accumule et quand il se détache. Ce contrôle est obtenu sans recourir à des revêtements chimiques ni à des procédés de fabrication complexes. Ces travaux montrent ainsi qu'un design géométrique simple peut servir de fondation à des surfaces passives, robustes et programmable de gestion de l'eau. Ils identifient également les opérations fondamentales (capture, transport, stockage, transformation et libération) qui ouvrent la voie à une future plateforme millifluidique pilotée par la géométrie.

Publications

The contributions related to this manuscript are the following

- M. Léonard, J. Van Hulle, F. Weyer, D. Terwagne and N. Vandewalle, *Droplets sliding on single and multiple vertical fibers*, Physical Review Fluids **8**, 103601, 2023. Editors' suggestion.
- J. Van Hulle, C. Delforge, M. Léonard, E. Follet and N. Vandewalle, *Droplet Helical Motion on Twisted Fibers*, Langmuir **40**, 25413, 2024.
- M. Léonard and Vandewalle N., *Grooves spacing govern water retention during condensation*, Physical Review Fluids **10**, 114001, 2025. Editors' suggestion.
- M. Léonard, D. Maity, N. Vandewalle and T. Truscott, *Stretching water between two grooves*, Submitted in Physical Review Fluids. (Preprint version: arXiv:2509.25864, 2025).
- M. Léonard and N. Vandewalle, *Hanging droplets at the bottom edge of a grooved condensing plate*, In preparation.

Contents

0 Introduction

Water sits at the heart of both environmental resilience and technological performance. As climate change accelerates, droughts intensify, arid regions expand, and pressure on freshwater resources grows [1]. At the same time, rising global temperatures and expanding digital infrastructure sharply increase the demand for cooling [2], from everyday air-conditioners to large industrial facilities and data centers. As these systems chill warm air, they inevitably condense water on their cold surfaces, and efficient removal of this condensate becomes essential to maintain effective heat exchange [3]. These two trends converge on the same challenge: managing water more intelligently, whether as a scarce resource to be harvested [4] or as a working fluid for transporting and dissipating heat [5]. Meeting this challenge requires solutions that are passive, robust, and sustainable. Understanding how water interacts with surfaces is therefore an everyday, everywhere necessity for sustainability.

Although sustainability is a large-scale problem, its resolution often hinges on microscale phenomena. Atmospheric water harvesters (fog and dew), for instance, rely on droplets only a few millimeters wide [6]. Their efficiency depends on how long these droplets remain pinned, how they merge, and whether they drain or accumulate [7]. Similarly, in heat exchangers and heat pumps, the contrast between dropwise [8] and filmwise condensation [9] can change significantly heat-transfer rates, and this contrast is governed entirely by the behavior of micrometric films and droplets. These examples show that controlling small amounts of water is not a marginal detail but a key lever for improving large-scale sustainability.

Nature provides compelling evidence that small volumes of water can be manipulated effectively using only structural features as illustrated in Figure 1. Fauna, flora, and other organisms have evolved grooves, ridges, spines, and scales that collect, guide, and release water passively. These natural systems highlight a simple yet powerful principle: geometry and chemistry together determine water behavior. Scale network channel water [10] (Figure 1(a)), cactus spines condense dew [12], and spider silks collect and gather fog droplets (Figure 1(b)) [11]. Engineered sur-

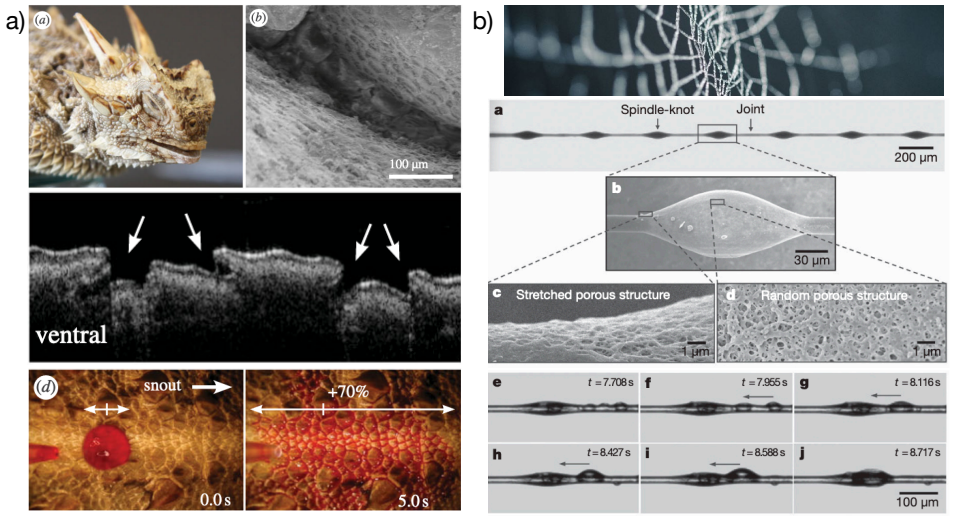

Figure 1: (a) Water-guiding scales on the Texas horned lizard, whose asymmetric microstructure drives directional transport [10]. (b) Spider silk, where periodic spindle-knots and joints collect, coalesce, and shuttle fog droplets along the fiber [11] (credit for top photo: Nicolas Picard). These biological textures illustrate how simple geometric features can passively manipulate small volumes of water.

faces have drawn heavily from these ideas, often reproducing natural designs using coatings or fine-scale texturing. Yet such treatments, while effective, can suffer from aging, contamination, fragility, or high fabrication and environmental costs [13]. The contrast between the robustness of natural systems and the limitations of engineered ones leaves ample room for further research.

Motivated by these observations, this thesis adopts a design philosophy centered on simplicity and robustness. The systems studied here rely on common, raw materials such as acrylic plates and nylon fibers and use only pure water or simple silicone oils as working fluids. Their grooves are created using accessible fabrication techniques like laser engraving or fiber twisting rather than delicate chemical functionalization or fine-scale texturing. This approach avoids the fragility and aging associated with specialized coatings and textures. By focusing on minimal yet controlled structures, we aim to uncover geometric mechanisms that remain effective across scales and robust under real-world conditions.

Decades of research provide a solid foundation for understanding how water behaves on smooth substrates, from plates to fiber. Classical wetting theory describes morphology transitions from droplets to films as functions of flow rate and liquid–solid affinity [14, 15, 16, 17, 18]. Grooved surfaces have also been studied, particularly on horizontal substrates where grooves may absorb [19] or elongate droplets [20], pin contact lines [21], and enable long-range capillary communication between distant droplets [22]. Much less, however, is known about how grooves influence dynamic processes such as condensation and transport [22]. In most existing studies, grooves are treated primarily as tools to create superhydrophilic [9] or superhydrophobic states [21]. This leaves an open fundamental question about the intrinsic role of groove geometry itself: **Can grooves govern droplet growth, transport, and release on vertical surfaces?**

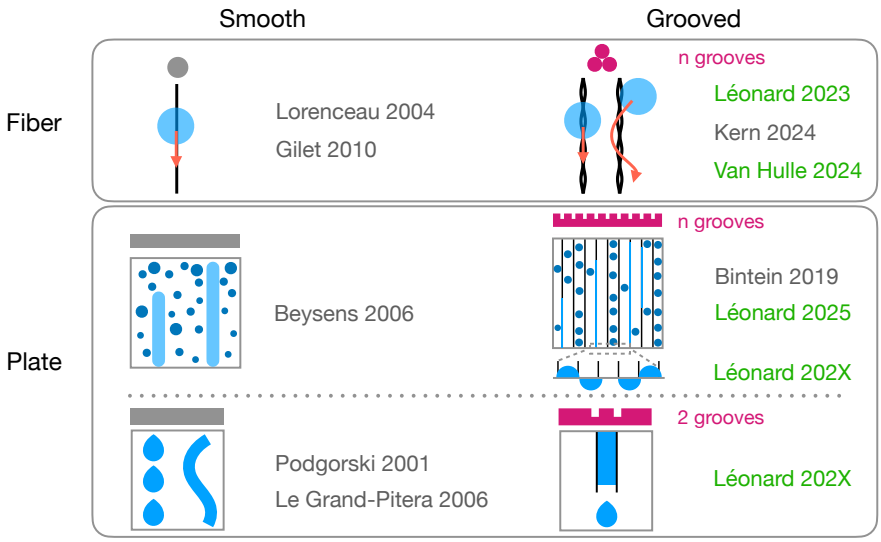

Figure 2: Schematic overview of the thesis structure. The left column summarizes classical studies on smooth vertical surfaces, where droplets, rivulets, or films drain under gravity. The right column presents the three grooved systems investigated in this thesis. We begin with fiber bundles and examine how substructure alters droplet dynamics and fiber coating. We then move to condensation on a vertical plate and show how groove spacing reorganizes drainage and dripping at the lower edge. Finally, we study a minimal configuration in which water is injected between two grooves on a vertical substrate, revealing how this geometric feature stabilizes a thin film and localizes its periodic rupture at groove terminations.

This thesis addresses this gap by examining how grooves influences liquid behavior across three common situations, illustrated Figure 2. First, we analyze how grooves within fiber bundles modify droplet dynamics, dissipation, and coating as droplets descend under gravity. Second, now on a vertical condensing plate, we study how groove spacing controls droplet growth and retention. Then we investigate how grooves influence dripping at the lower edge of this plate, where guided drainage transitions into dripping. Finally, we explore whether a pair of vertical grooves can stabilize thin films of pure water but also trigger their destabilization. Together, these complementary studies reveal how simple geometric elements, acting alone and without special materials or coatings, can define where liquid accumulates, how it moves, and when it is released.

1 Research context

1.1 Water properties

1.1.1 Surface tension

Liquids hold together because their molecules attract one another through cohesive forces [23]. Inside the bulk, this cohesion is balanced: each molecule is surrounded on all sides by identical neighbors, experiencing the maximum number of interactions. But at the interface, the symmetry breaks. Surface molecules have fewer neighbors, leaving them in a higher-energy state (Figure 1.1(left)). The system responds by pulling these surface molecules inward, reducing the total exposed area.

This imbalance is what we perceive as surface tension. Energetically, it represents the cost of creating interface. If a molecule in the bulk has an interaction energy U, a molecule at the surface experiences roughly half of it, $U/2$. Dividing this difference by the molecular surface area a^2 gives a crude estimate of surface tension, $\sigma \approx U/(2a^2)$. For most organic liquids, where van der Waals forces dominate and

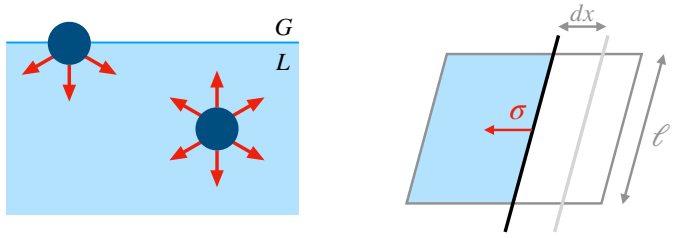

Figure 1.1: (Left) A molecule at the fluid interface experiences roughly half as many interactions with its neighbors as a molecule located in the bulk of the liquid. (Right) Spontaneous motion of a rod driven by a soap film. This motion is a direct consequence of surface tension, which acts to minimize the area of the film.

U is of order kT, this gives $\sigma \sim 20\,\mathrm{mJ/m^2}$ at room temperature ($kT \approx 1/40\,\mathrm{eV}$ at 25°C).

The stronger the molecular bonds, the higher this energy cost. Water, held together by hydrogen bonds, reaches $\sigma \approx 72\,\mathrm{mJ/m^2}$. Liquid metals such as mercury, bound by metallic cohesion, can reach $\sigma \approx 500\,\mathrm{mJ/m^2}$. These wide variations reflect how microscopic interactions (van der Waals, hydrogen, or metallic) govern the macroscopic tendency of a liquid to resist surface creation.

Although surface tension is most familiar at air–liquid boundaries, the same principle applies to any interface separating two immiscible phases. Oil droplets on water, for instance, experience an interfacial tension at their mutual boundary. But when the two liquids are miscible, like fresh and salt water, no stable interface forms, their molecules mix freely, and the interfacial tension vanishes.

1.1.2 Interpretations

Even if surface tension originates from molecular-scale forces, its effects are tangible at the macroscopic scale [23]. A simple experiment makes this visible. Imagine a square frame made of four copper rods, each of length l, with a fifth rod slightly longer serving as a movable bar, see Figure 1.1(right). When the frame is dipped into soapy water, two films form on either side of the mobile rod. If one of these films is pierced, the balance is broken: the remaining film instantly pulls the bar toward itself. The motion is immediate and unambiguous, proof that surface tension acts as a real mechanical force along the rod.

This demonstration also provides a direct way to quantify that force. If the bar moves by a distance dx, the work W done by the film is

$$\delta W = F\,dx = 2\sigma l\,dx, \tag{1.1}$$

where the factor 2 accounts for the two air–liquid interfaces of the soap film. From this relation, surface tension σ appears as a force per unit length acting tangentially to the surface, with units of [N/m].

The same quantity, however, can be viewed through an energetic lens. Liquids spontaneously minimize their surface area to lower their interfacial energy, as the soap film does. At the opposite, increasing that area A requires external work, as when vigorously shaking a vinaigrette to disperse oil into vinegar. Each droplet created adds new interface, and each square meter of it costs an energy σ. Formally,

$$\delta W = \sigma\,dA, \tag{1.2}$$

showing that surface tension can also be expressed as an energy per unit area, $\left[\mathrm{J/m^2}\right]$.

These two perspectives, force and energy, describe the same phenomenon from different standpoints. The mechanical view emphasizes how surface tension acts along a boundary; the energetic one reveals how it governs the system's drive to minimize area.

1.1.3 Laplace pressure

Curvature influences pressure in liquids in ways that often defy intuition. Small bubbles collapse while larger ones grow, as in cappuccino foam, because surface

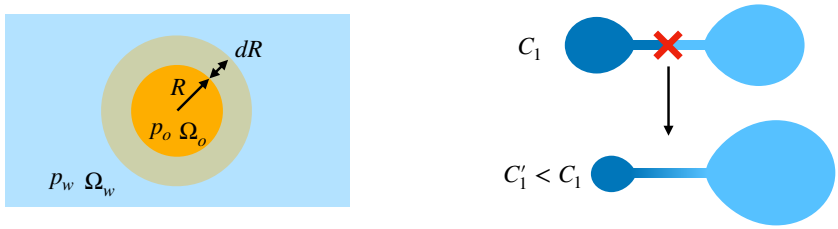

Figure 1.2: (Left) Increase in the surface area of an oil droplet (o) with internal pressure p_o immersed in a water bath (w) at pressure p_w, by expanding its radius R by a small amount dR. (Right) Drainage of a smaller balloon into a larger one due to the pressure difference induced by curvature C, as predicted by the Laplace law (Equation 1.5).

tension couples directly to geometry. This relationship is captured by the Laplace law.

To make this link quantitative, consider a spherical droplet of oil suspended in water (Figure 1.2). Surface tension between the two fluids drives the droplet toward a shape that minimizes its interfacial area, namely a sphere of radius R. Now imagine stretching this droplet slightly, by increasing its radius by dR, as if pulling uniformly from all sides. The required work combines contributions from pressure and surface tension:

$$\delta W = -p_o \, dV_o - p_w \, dV_w + \sigma_{ow} \, dA, \tag{1.3}$$

where p_o and p_w are the pressures inside and outside the droplet, σ_{ow} is the interfacial tension, $dV_o = 4\pi R^2 dR$ the increase in oil volume, $dV_w = -dV_o$ the corresponding decrease in water volume, and $dA = 8\pi R \, dR$ the change in interfacial area.

At equilibrium, the total work vanishes ($\delta W = 0$), leading to

$$\Delta p = p_o - p_w = \frac{2\sigma_{ow}}{R}. \tag{1.4}$$

This is the Laplace law, which states that the pressure inside a droplet exceeds the external pressure by an amount proportional to surface tension and inversely proportional to its radius. In short, the smaller the droplet, the greater the pressure drop.

This imbalance has striking consequences. Connect two balloons of different sizes with a valve, and open it: rather than equalizing, air flows from the smaller balloon to the larger one, as represented in Figure 1.2(right). The small balloon's higher internal pressure, dictated by its stronger curvature C, drives the transfer. As it deflates, the pressure difference grows, accelerating the flow. The same principle governs foams: in a cappuccino or a beer, small bubbles collapse while larger ones expand, leading to gradual foam coarsening.

The Laplace law generalizes to any curved surface:

$$\Delta p = \sigma \left(\frac{1}{R_1} + \frac{1}{R_2} \right) = \sigma C, \tag{1.5}$$

where R_1 and R_2 are the principal radii of curvature, and C is the total curvature. In the case of a sphere, $R = R_1 = R_2$ and we get Equation (1.4) back.

This simple relationship encapsulates a powerful idea: surface tension links geometry and mechanics. Curvature dictates the pressure jump across an interface, influencing how droplets, bubbles, and thin films form and evolve, the very dynamics that will occupy the rest of this thesis.

1.1.4 Plateau-Rayleigh instability

One of the most common demonstrations of surface tension in action is the spontaneous breakup of a liquid thread into droplets, known as the Plateau-Rayleigh instability [24, 25]. Anyone who has watched a thin stream of water falling from a tap has seen it: what begins as a continuous filament soon transforms into a chain of droplets.

Two simple principles underlie this behavior. First, as the filament falls, gravity accelerates it, increasing its velocity. Second, mass conservation dictates that as velocity increases, the cross-sectional area must decrease. The stream therefore thins as it falls. But this thinning exposes a fundamental conflict: a long, narrow cylinder of liquid does not minimize surface area for a given volume, whereas surface tension continually acts to reduce that area. The cylindrical shape is thus intrinsically unstable, it will rearrange itself into droplets, which have the smallest possible surface area for their volume.

This intuition can be made quantitative [23]. Consider a liquid cylinder of radius R and length L that breaks up into n spherical droplets of radius r. Conservation of volume requires

$$\pi R^2 L = \frac{4}{3}\pi r^3 n. \tag{1.6}$$

The total surface area of the droplets is $S_n = n4\pi r^2$, while the original cylinder had $S_c = 2\pi RL$. The breakup is energetically favorable if the surface area decreases

$$\frac{S_n}{S_c} < 1 \quad \Rightarrow \quad r > \frac{3R}{2}. \tag{1.7}$$

This simple criterion shows that once disturbances are large enough, surface tension amplifies the deformation instead of smoothing it. The cylinder then fragments into separate droplets.

1.2 When does surface tension matter?

Surface tension governs the shape and behavior of many fluid systems, but not all. In everyday life, other phenomenons such as gravity, inertia, or viscosity often overwhelm surface tension, masking its effects. Understanding when surface tension matters requires comparing its magnitude with those of competing forces. To do this, dimensionless numbers are used to quantify the relative importance of different physical effects.

1.2.1 Gravity

A small droplet typically maintains a spherical shape on a surface, while a larger one spreads into a shallow puddle, as shown in Figure 1.3 (left). The difference reflects a competition between two forces: gravity, which pulls liquid downward,

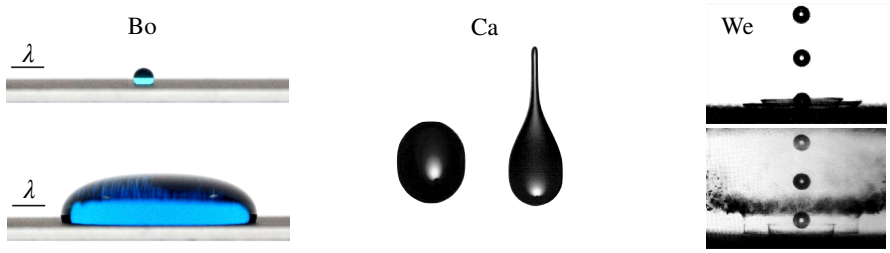

Figure 1.3: When surface tension dominates, the liquid minimizes its surface area: a resting droplet remains spherical (left), a sliding one keeps a circular footprint (center), and even upon impact, the droplet largely preserves its integrity (right). Conversely, when other forces prevail, the behavior changes: strong gravity (Bo $\gg$) flattens the droplet, high viscosity (Ca $\gg$) stretches it during motion, and dominant inertia (We $\gg$) causes it to fragment upon impact. Illustrations, from left to right, from [26, 27, 28].

and surface tension, which holds it together. At small scales, surface tension wins, maintaining compact, curved shapes. As droplets grow, their weight eventually overcomes this cohesion, flattening them against the surface.

This balance is captured by the Bond number, which compares gravitational to capillary forces

$$\mathrm{Bo} = \frac{\rho \mathrm{g} \mathrm{r}^2}{\sigma}, \tag{1.8}$$

where ρ is the liquid density, g the gravitational acceleration, r a characteristic length scale (typically the droplet radius), and σ the surface tension.

When Bo $\ll 1$, surface tension dominates. Droplets remain nearly spherical, as seen with a $3\,\mu$l water drop on a hydrophobic surface (Figure 1.3(left)). When Bo $\gg 1$, gravity takes over: a $500\,\mu$l drop flattens noticeably under its own weight. The transition between these regimes occurs around Bo ≈ 1.

This threshold defines a natural length scale known as the capillary length λ, given by

$$\lambda = \sqrt{\frac{\sigma}{\rho g}}. \tag{1.9}$$

For water at room temperature, with $\sigma \approx 72\ 10^{-3}\,\mathrm{N/m}$ and $\rho \approx 1000\,\mathrm{kg/m^3}$, the capillary length is approximately $\lambda = 2.7\,\mathrm{mm}$. This simple comparison provides a powerful rule of thumb, one that will prove essential in evaluating fluid behaviors on microstructured substrates.

1.2.2 Viscosity

Viscosity is the property that measures how strongly neighboring layers of fluid drag on one another. To see this in action, consider a simple case, the Couette flow. An incompressible fluid is confined between two infinite parallel plates of surface S separated by a gap h. The lower plate is fixed, while the upper one moves steadily at velocity v_0 through an applied force F_x (Figure 1.4). After a short transient, the fluid settles into a steady linear velocity profile

$$v_x(y) = v_0 \frac{y}{h}. \tag{1.10}$$

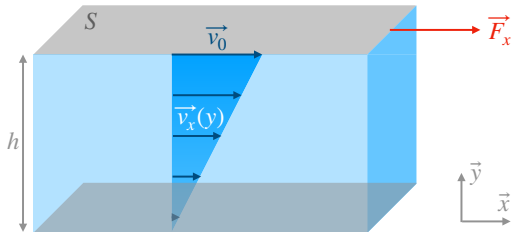

Figure 1.4: Schematic representation of planar Couette flow. An incompressible fluid is confined between two parallel plates separated by a height h. The bottom plate remains stationary while the upper one moves at constant velocity v_0, generating a linear velocity profile. This drawing illustrates how viscous forces govern the transfer of momentum in shear-driven flows.

This velocity gradient generates a shear stress $\tau = F_x/S$, which is proportional to the gradient of velocity across the fluid

$$\tau = \eta \frac{\partial v_x}{\partial y}, \tag{1.11}$$

where η is the dynamic viscosity, expressed in Pa s. High-viscosity fluids, like honey, require large forces to sustain motion; low-viscosity fluids, like water, deform readily under the same stress. Viscosity thus quantifies the internal friction that governs momentum transfer between adjacent layers. Dividing η by the fluid density ρ gives the kinematic viscosity $\nu = \eta/\rho$, with units m^2/s. It characterizes how quickly momentum diffuses through the liquid, and is often reported in centiStokes ($1\,\mathrm{cSt} = 10^{-6}\,\mathrm{m}^2/\mathrm{s}$).

The relative importance of viscous forces compared to surface tension is captured by the capillary number, defined as

$$\mathrm{Ca} = \frac{\eta \mathrm{v}}{\sigma}, \tag{1.12}$$

where v is a characteristic velocity of the fluid. When $\mathrm{Ca} \ll 1$, surface tension dominates and the fluid retains compact shapes. When Ca increases, viscous forces distort the interface.

This interplay is visible in a simple everyday scene. After a shower, small droplets slide down a vertical wall. At low speed, they keep a nearly spherical cap shape, surface tension dominates. As they accelerate, the droplets stretch and develop a tail, signaling that viscous forces now compete with interfacial tension [29, 30], as illustrated in Figure 1.3(center).

1.2.3 Inertia

The Weber number, denoted We, quantifies the ratio between inertial forces and capillary forces acting on a fluid. It is defined as

$$\mathrm{We} = \frac{\rho r v^2}{\sigma}, \tag{1.13}$$

where r is a characteristic length scale (typically the droplet radius).

A classic illustration involves a droplet impacting a horizontal surface [31], as seen in Figure 1.3(right). When the Weber number is high enough, inertia dominates: the droplet flattens violently upon impact, potentially producing splashing, crown-shaped structures, or secondary jets. In contrast, at low Weber numbers, surface tension prevails. The droplet undergoes only slight deformation and quickly relaxes back into a near-spherical shape, minimizing its interfacial energy.

1.2.4 Overview for different liquids

Fluid	ρ (kg/m^3)	η (mPa s)	σ (mN/m)	λ (mm)
Water (5 °C)	1000	1.52	75.6	2.77
Water (20 °C)	998	1.00	72.8	2.70
Water (70 °C)	977	0.41	62.0	2.52
Vegetable oil	910	65–80	32–35	∼2.00
Silicone oil (100 cSt)	965	100	20–21	∼1.45
Ethanol	789	1.20	22.4	1.70
Glycerol (100%)	1260	945	63.4	2.25
Mercury	13 546	1.55	485	1.91

Table 1.1: Physical properties of selected fluids at room temperature [32].

Surface tension varies widely across materials, reflecting the nature of intermolecular forces. Water, held together by hydrogen bonds, reaches about 73.0 mN/m. Metallic cohesion in mercury raises it to 485.0 mN/m, while weak van der Waals forces keep ethanol or silicone oil near 20.0 mN/m. Temperature further modulates these values, warming water from 5 to 70 °C lowers σ from 75.6 to 62.0 mN/m and reduces viscosity by more than a factor of three.

Yet the capillary length λ remains strikingly stable, typically between 1.5 and 2.8 mm. Changes in surface tension are largely offset by corresponding changes in density. This compensation gives the capillary length a special status. It provides a universal reference scale below which surface tension dominates, regardless of whether the liquid is metal, oil or water. In practice, it is the natural ruler of capillary phenomena.

1.3 Droplet on a horizontal surface

1.3.1 Smooth substrate

A droplet of water spreads into a thin film on a glass plate, but remains nearly spherical on a Teflon surface. This contrast is governed by the balance of interfacial energies between the liquid, solid, and surrounding vapor. For a liquid on a smooth, chemically uniform substrate, this balance is expressed by the spreading parameter S [23, 33]:

$$S = \sigma_{SA} - \sigma_{SL} - \sigma, \tag{1.14}$$

where σ_{SA}, σ_{SL}, and σ are the solid–air, solid–liquid, and liquid–air surface tensions.

When $S > 0$, spreading lowers the total interfacial energy: the liquid replaces the solid–air interface with lower-energy solid–liquid and liquid–air interfaces. The

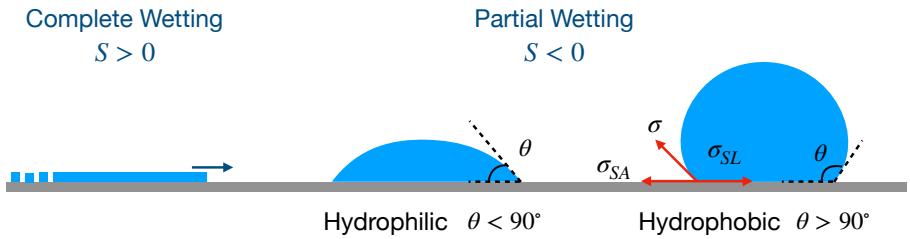

Figure 1.5: The sign of the spreading parameter S, depending of different surface tension σ of the present phases (Equation (1.14)), governs the wetting regime.

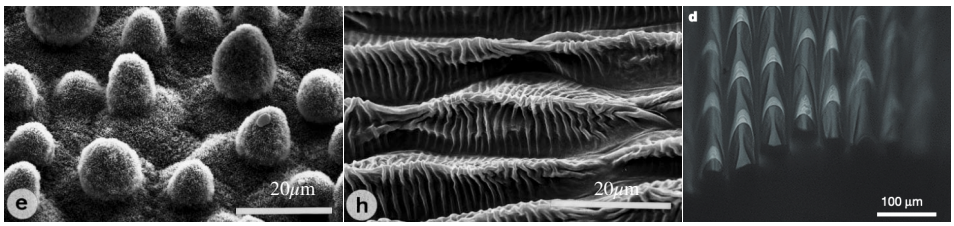

Figure 1.6: Some varieties of natural roughness. Spikes on the leaf of the lotus flower (*Nelumbo nucifera*) (left), folds in the the petals of *Mutisia decurrens* (center)[38], and tiles on the pitcher of *Nepenthes alata* [39].

droplet then expands radially as soon as it touches the surface, as represented in Figure 1.5(left). Its spreading radius follows Tanner's law [34, 35],

$$r(t) \sim \Omega^{3/10} \left(\frac{\sigma t}{\eta} \right), \tag{1.15}$$

where Ω is the droplet volume. In this complete-wetting regime, a subtle feature appears: a nanometric precursor film advances ahead of the visible contact line. Driven by van der Waals forces, it smooths the transition between wet and dry regions and regularizes the contact-line singularity[36].

When $S < 0$, spreading would increase the total interfacial energy. The droplet thus stabilizes at a finite footprint, corresponding to the partial wetting regime (Figure 1.5(center-right)). At equilibrium, three interfaces (solid–air, solid–liquid, and liquid–air) meet at a well-defined contact angle θ that satisfies the Young–Dupré relation [37]

$$\sigma_{SA} = \sigma_{SL} + \sigma \cos\theta. \tag{1.16}$$

This balance of capillary forces at the contact line directly links the measurable contact angle to the surface energies of the materials. Surfaces with $\theta < 90°$ are termed hydrophilic, while those with $\theta > 90°$ are hydrophobic.

1.3.2 Basic texture

Natural surfaces exhibit structural complexity across a wide range of length scales, from the centimeter to the nanometer, and encompass a variety of geometries, from spikes to tiles, as illustrated in Figure 1.6. To investigate the influence of these

structures on liquid behavior, we begin by analyzing two simplified configurations: a droplet interacting with a cylindrical capillary and a rectangular groove.

Capillary rise

A liquid wets a tube only if it lowers the surface energy of the solid, that is, if the dry solid–air energy σ_{SA} exceeds the solid–liquid energy σ_{SL}[23]. The impregnation parameter captures this balance,

$$I = \sigma_{SA} - \sigma_{SL}. \tag{1.17}$$

When $I > 0$, replacing a dry surface by a wet one reduces the total energy, and the liquid spontaneously invades the tube or a porous medium. When $I < 0$, the dry state is favored and the liquid recedes, a phenomenon known as capillary descent if we consider a vertical capillary dipped in a liquid.

Using Young's relation (Equation (1.16)), the condition for impregnation becomes simply $\theta < 90°$. Liquids satisfying this criterion are called wetting, though impregnating is more accurate. The condition $I > 0$ is also much less restrictive than the spreading criterion $S > 0$, since $I = S + \sigma$. This explains why most liquids readily soak porous materials, whereas complete spreading on smooth solids is rare: impregnation replaces one interface, spreading creates two.

If we now consider a vertical capillary, the energy of a liquid column of height h in a capillary of radius R combines the gain in surface energy and the cost in gravitational potential energy:

$$E = -2\pi R h I + \tfrac{1}{2}\pi R^2 h^2 \rho g. \tag{1.18}$$

Minimizing E yields the equilibrium height rise, known as Jurin's height:

$$H = \frac{2\sigma\cos\theta}{\rho g R}. \tag{1.19}$$

This relation holds when $R \ll H$, that is, when the tube radius is small compared with the capillary length.

Once the liquid starts to rise, its dynamics reveal a subtle balance between capillary driving and viscous resistance [23]. In narrow tubes or pores, every molecule lies close to a wall where the velocity must vanish through the no-slip condition. The flow is therefore slow, and inertia can be neglected compared with viscous friction. Neglecting the weight of the liquid column, valid at short times or in horizontal geometries, the balance between capillary suction and viscous drag leads to the description of the meniscus height z as function of time

$$z(t) = \sqrt{\frac{1}{2}\frac{\sigma R\cos\theta}{\eta}}\,\sqrt{t}. \tag{1.20}$$

This relation, known as Washburn's law, shows that the front advances rapidly at first, then slows down with $z \propto \sqrt{t}$.

At very short times ($t \to 0$), however, Washburn's law predicts an nonphysical divergence of velocity ($\dot{z} \propto 1/\sqrt{t}$). The correction comes from inertia: the liquid cannot accelerate instantaneously. The liquid column, connected to a reservoir

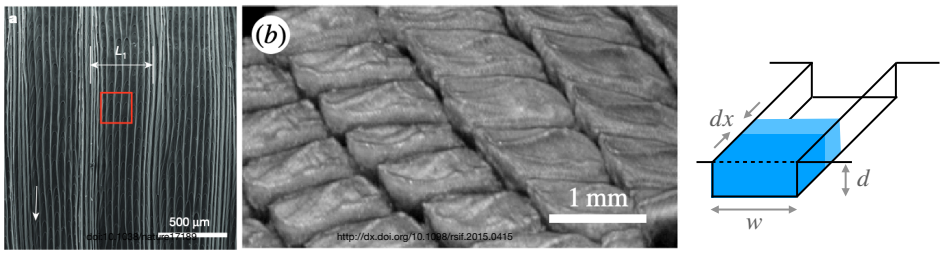

Figure 1.7: Grooves are widespread in nature across many length scales. Grooves and sub-grooves cover the peristome surface of a pitcher plant [39] (left). A network of channels forms between the dorsal scales of the Texas horned lizard [10] (center). Schematic illustrating the advancement dx of a liquid front within a groove of depth d and width w (right).

at rest, is set in motion by a constant capillary force. Solving the corresponding momentum balance gives

$$z(t) = \sqrt{\frac{2\sigma \cos\theta}{\rho R}}\, t. \tag{1.21}$$

For a millimetric tube, this corresponds to an impregnation speed about 100 mm/s. This fast velocity phase lasts only briefly. After a characteristic time

$$\tau \sim \frac{\rho R^2}{\eta}, \tag{1.22}$$

viscous stresses have diffused across the tube, establishing a fully developed flow. Beyond this point, inertia fades, and the system transitions smoothly to the slower, viscous regime governed by Washburn's law.

On vertical systems, gravity eventually balances capillarity. The rise then slows exponentially as the liquid approaches its equilibrium height given by Jurin's law (Equation 1.19). The final stage of capillary rise is thus a gentle relaxation toward this limit, completing the full sequence from inertia-dominated onset to viscous slowing and gravitational equilibrium.

Groove impregnation

As illustrated in Figure 1.7, many solid surfaces, both natural and artificial, exhibit grooves. These grooves can also become impregnated with liquid. However, the condition for impregnation differs slightly from that described in a capillary through Equation (1.32) due to the presence of an additional interface. Consider a single rectangular groove of width w and depth d [33]. For simplicity, we neglect the precise curvature of the meniscus and assume a flat liquid–air interface at the top of the groove, which corresponds to a configuration of minimal interfacial area.

For a liquid to spread into the groove spontaneously, the total surface energy must decrease as the contact line advances (hydrophilic substrate). The solid must therefore gain energy by being wetted ($\sigma_{SL} < \sigma_{SA}$), but this gain must also offset the cost of creating a liquid–air interface of width w at the groove opening.

If the liquid advances by a small distance dx, the corresponding change in interfacial energy per unit length is

$$dE = (\sigma_{SL} - \sigma_{SA})(2d + w)\, dx + \sigma\, w\, dx, \tag{1.23}$$

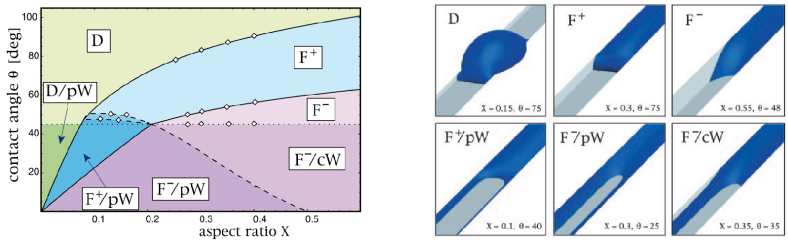

Figure 1.8: (Left) Morphology diagram illustrating the different wetting configurations of a droplet deposited on a grooved substrate as a function of the groove aspect ratio (depth-to-width) and the intrinsic contact angle of the surface. The diagram delineates distinct regimes including spherical-cap droplets, confined filaments, and wedge-shaped corner films. (Right) Schematic representations of the corresponding droplet morphologies referenced in the diagram: (1) isotropic droplet over spilling across ridges, (2) elongated filament confined within a groove, and (3) wedge-shaped liquid films localized in groove corners. Adapted from [40].

where the first term accounts for the newly wetted solid walls and base, and the second for the liquid–air interface created at the top. Neglecting gravity, impregnation is energetically favorable ($dE < 0$) when $\theta < \theta_c$, with a critical contact angle defined by

$$\cos\theta_c = \frac{w}{2d + w}. \tag{1.24}$$

We can also reverse this equation to determine the right groove aspect ratio to allow impregnation knowing the contact angle

$$\frac{d}{w} = \frac{1 - \cos\theta}{2\cos\theta}. \tag{1.25}$$

Seemann *et al.* [40, 41] explore further away the wetting morphologies that emerge on rectangular grooved substrates with curved liquid interfaces (see Figure 1.8). At low aspect ratios and high contact angle, droplets spread isotropically and over spill across ridges. As groove depth increases or contact angle decreases, the groove confine the droplet, forming filaments that extend along the groove while maintaining nearly constant cross-section. The curvature of the air–liquid interface within these filaments plays a critical role: when the internal angle of the groove is greater than 90°, the interface is convex and the Laplace pressure is positive, resisting further infiltration. When the angle drops below 90°, the interface becomes concave, generating a negative pressure that draws liquid inward. This switch in curvature governs whether or not a groove absorbs fluid. At even lower contact angles (below 45°), wetting concentrates in the corners, forming thin wedge-shaped films.

1.3.3 Roughness and heterogeneities

Now that we have a better understanding of the interaction of a liquid with a substrate geometry, let's move on to non perfectly smooth substrate On the micrometer scale, either on natural or processed surfaces, roughness is the rule rather than the exception [33]. Nature offers a wide variety of textures, some of which are shown in Figure 1.6. On the human side, it can arise from fabrication techniques, such as lamination, which leaves behind grooves, or from intrinsic

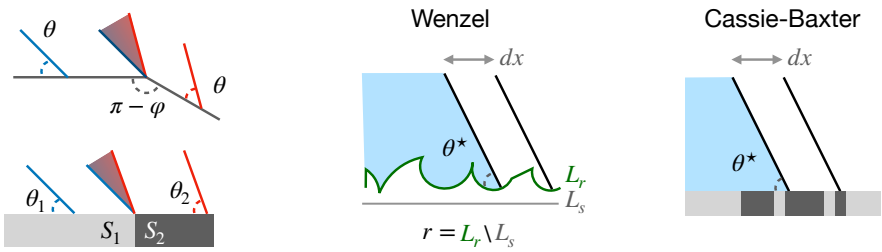

Figure 1.9: (Left) Contact angle hysteresis induced by a topographic defect. A droplet approaching a step experiences different contact angles before and after the edge, which can pin the contact line. (Right) Effect of roughness on the apparent contact angle $\theta^\star$, as predicted by the Wenzel model. Surface topography amplifies the intrinsic wettability depending on the roughness factor r.

microstructures, like compacted grains. In contrast, truly smooth substrates, flat down to the molecular scale, are rare.

Surface roughness plays a decisive role in how droplets move, or fail to move, on solids. As first noted by Gibbs [14], microscopic heterogeneities can pin the contact line, preventing motion even on inclined surfaces. Pinning arises from two main sources: topographical irregularities and chemical heterogeneity.

Consider a small step inclined by an angle φ, as illustrated in Figure 1.9(left). Just before the edge, the liquid meets the solid with a local contact angle θ; just after, the geometry enforces an angle $\pi - \varphi + \theta$. On the edge, between these limits, the contact line can adopt a range of apparent angles $\theta^\star$, giving rise to contact angle hysteresis.

Rough substrate

One of the first quantitative models linking roughness and wetting was proposed by Wenzel [42, 43]. The goal is to determine the apparent contact angle, $\theta^\star$, of a droplet on a rough but chemically uniform surface, assuming that the local angle everywhere obeys Young's law, as represented in Figure 1.9(center). The model applies when the roughness scale is much smaller than the droplet size.

To evaluate $\theta^\star$, we consider a small displacement dx of the three-phase contact line. The corresponding change in surface energy per unit length is

$$dE = r(\sigma_{SL} - \sigma_{SA})\,dx + \sigma \cos\theta^\star\,dx, \tag{1.26}$$

where r is the roughness factor, the ratio between the true and projected surface areas. At equilibrium ($dE = 0$), the energy is minimal. For a smooth surface ($r = 1$), this reduces to Young's law; for $r > 1$, it yields the Wenzel relation

$$\cos\theta^\star = r\cos\theta, \tag{1.27}$$

where θ is the intrinsic Young angle.

This result shows that roughness amplifies the native wetting behavior. Hydrophilic surfaces become more wetting ($\theta^\star < \theta$), while hydrophobic ones become more water-repellent ($\theta^\star > \theta$). Wenzel's law also predicts possible wetting transitions: for large enough r, $|\cos\theta^\star|$ can exceed unity, implying either complete spreading ($\theta^\star = 0$) or complete dewetting ($\theta^\star = 180°$). In practice, however, such extremes are rarely observed, the model breaks down when roughness no longer acts as a simple geometric amplification.

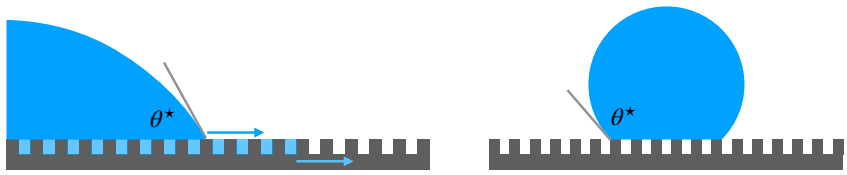

Figure 1.10: (Left) On a hydrophilic substrate, a thin portion of the liquid can seep into the texture ahead of the droplet, so the droplet effectively spreads over a composite solid–liquid surface. (Right) On a hydrophobic substrate, the liquid cannot penetrate the texture, forcing the droplet to rest on a composite solid–air surface instead.

Heterogeneous substrate

The same reasoning applies to chemically heterogeneous surfaces [33, 23]. Consider a flat substrate composed of two materials, as illustrated in Figure 1.9(left), with respective Young angles θ_1 and θ_2. Let f_1 and f_2 be their area fractions, with $f_1 + f_2 = 1$. Once again, we suppose that the chemical patches are small compared with the drop size.

For an infinitesimal displacement dx of the contact line (Figure 1.9(right)), the energy change per unit length is

$$dE = f_1(\sigma_{S_1L} - \sigma_{S_1A})\,dx + f_2(\sigma_{S_2L} - \sigma_{S_2A})\,dx + \sigma\cos\theta^\star\,dx. \tag{1.28}$$

Minimizing this energy and applying Young's relation to each component gives the Cassie–Baxter equation:

$$\cos\theta^\star = f_1\cos\theta_1 + f_2\cos\theta_2. \tag{1.29}$$

The apparent angle is thus a weighted average of the cosines of the intrinsic contact angles. It necessarily lies between θ_1 and θ_2, reflecting the composite nature of the interface.

Impregnation in hydrophilic substrate

Wenzel's law assumes that the liquid perfectly conforms to the surface topography, wetting every asperity. In practice, however, on rough hydrophilic substrates a negligible amount of liquid can infiltrate the texture [33, 23], as illustrated in Figure 1.10(left). As a result, the droplet no longer rests solely on the solid but on a composite surface made of both solid and liquid regions.

For a surface patterned with periodic grooves [19], let ϕ_s denote the fraction of the projected area beneath the droplet that is occupied by solid, while $(1 - \phi_s)$ corresponds to the fraction spanning over liquid. The droplet therefore interacts with a composite surface obeying a Cassie–Baxter-type relation:

$$\cos\theta^\star = (1 - \phi_s) + \phi_s\cos\theta. \tag{1.30}$$

Even with high roughness, total wetting ($\theta^\star = 0$) cannot occur unless the intrinsic angle is $\theta = 0$. In partial wetting ($\theta > 0$), some dry plateaus always remain above the imbibed film.

This description is accurate only if a film develop inside the texture. But for the film to invade the texture, capillary forces must overcome the cost of creating a free liquid–air interface. Let us look closely to that condition. Considering an infinitesimal advance dx of the wetting front gives the energy change

$$dE = (r - \phi_s)(\sigma_{SL} - \sigma_{SA})\, dx + (1 - \phi_s)\sigma\, dx. \tag{1.31}$$

Penetration is favorable ($dE < 0$) when

$$\cos\theta > \frac{1 - \phi_s}{r - \phi_s} = \cos\theta_c, \tag{1.32}$$

defining a critical angle θ_c between 0° and 90°. For $90° > \theta > \theta_c$, the surface remains dry and Wenzel's law applies; for $\theta < \theta_c$, the liquid invades the texture and Equation (1.30) describes the apparent angle.

Thus, Wenzel's law alone cannot capture all rough-surface wetting. The actual regime depends on both geometry and surface chemistry, with θ_c marking the transition between capillary impregnation and classical rough wetting.

Air entrapment in hydrophobic substrate

For hydrophobic substrates ($\theta > 90°$, $\sigma_{SA} < \sigma_{SL}$), the situation reverses. The liquid may not follow the texture but instead trap air beneath it, forming a composite solid–air base [23, 33].

Consider a patterned surface with solid fraction ϕ_s (Figure 1.9). The solid patches have intrinsic angle θ, while the air pockets correspond to an ideal angle of 180° (considering that the droplet size greatly exceeds texture size keeps Laplace pressure uniform and thus the air liquid interface flat). The Cassie–Baxter law then becomes

$$\cos\theta^\star = -1 + \phi_s(\cos\theta + 1). \tag{1.33}$$

This relation predicts much larger apparent angles than Wenzel's law. As ϕ_s decreases, $\cos\theta^\star$ approaches -1 and $\theta^\star$ approaches 180°, although the limit can never be reached since $\phi_s = 0$ or $\theta = 180°$ are nonphysical. In practice, even the most hydrophobic materials ($\theta \approx 120°$) produce apparent angles around 160° for $\phi_s \approx 0.1$. Achieving true superhydrophobicity therefore requires extremely small solid fractions.

Finally, stability determines whether the droplet remains suspended (Cassie) or collapses into the roughness (Wenzel). Equation (1.32) defines a critical angle θ_c. For $\theta < \theta_c$, the Wenzel state is stable; for $\theta > \theta_c$, the air-trapping Cassie state becomes energetically preferred. In practice, Cassie states often appear below the threshold, meaning that they are metastable, artificially maintained by contact-line pinning.

1.4 Fluid dynamic on an inclined surface

When a droplet is gently placed on a tilted surface, it doesn't immediately slide downhill. Instead, it often clings in place, held by forces at the contact line. This apparent stickiness is due to contact angle hysteresis, a difference between the advancing angle θ_A and the receding angle θ_R, both illustrated in Figure 1.11(left).

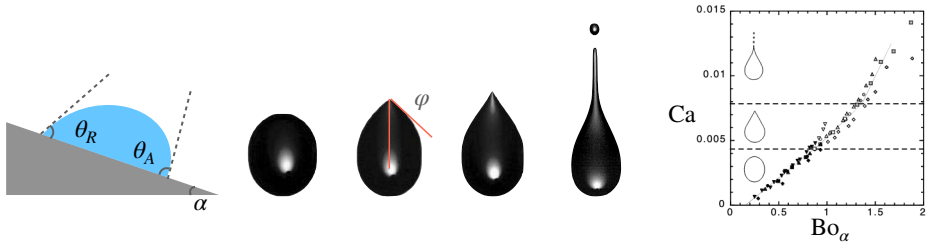

Figure 1.11: Droplet morphologies as speed increases. (Left) Motion begins once the advancing and receding contact angles reach their thresholds value, θ_A and θ_R. (Center) As velocity rises, the droplet first becomes oval, then develops a rear corner and eventually a cusp as the contact line struggles to keep up with the dewetting speed. At the highest speeds, the droplet sheds smaller droplets from its rear. (Right) In the oval regime, the droplet shape follows a robust relation between the capillary number Ca and the Bond number Bo. Pictures and graph from [27].

At rest, the droplet's weight is balanced by capillary forces at the contact line. Specifically, the droplet begins to slide only when the down slope component of its weight, $\rho\Omega g \sin\alpha$, exceeds a capillary threshold:

$$\rho\Omega g \sin\alpha = \beta\sigma(\cos\theta_R - \cos\theta_A), \tag{1.34}$$

where β is a geometric factor that depends on the droplet footprint [14, 44, 45]. As long as this capillary restoring force outweighs gravity, the droplet remains pinned. Its shape remains compact, but visibly asymmetric: the front stretches slightly down slope, while the rear flattens out. Gradually increasing the inclination angle increases the droplet's down slope force. When the balance tips, the droplet begins to slide. This defines a critical Bond number,

$$\mathrm{Bo}_\alpha = \frac{\Omega^{2/3}}{\lambda^2}\sin\alpha, \tag{1.35}$$

which captures the onset of motion.

Once in motion, the droplet reaches a steady velocity v, set by the balance between gravity and viscous dissipation. In this low-speed regime, the droplet shape remains smooth and oval-like (Figure 1.11(center)). Its capillary number, $\mathrm{Ca} = \eta v/\sigma$, increases nearly linearly with Bo_α [29, 30] (Figure 1.11(right)).

As velocity continues to rise, by further tilting the surface, a sharp transition occurs. The rear of the droplet flattens, forming a corner, a pointed shape where two straight segments of the contact line meet at a finite angle φ [30] (Figure 1.11(center)). This transition occurs at a finite critical receding angle θ_c [46]

$$\theta_c = \frac{\theta_r}{\sqrt{3}}. \tag{1.36}$$

This transition is a trick: the inclination of the contact line reduces the normal velocity, delaying the dynamical wetting transition [47]. This is reflected in the scaling $\sin\varphi \propto 1/\mathrm{Ca}$, indicating that the corner narrows further to maintain a fixed normal velocity as the droplet speed increases.

At even higher speeds, the corner sharpens further into a cusp [15] (Figure 1.11). The trick can't be maintain anymore : the receding contact line curves inward, and the rear becomes unstable. The droplet begins to shed smaller droplets, a behavior

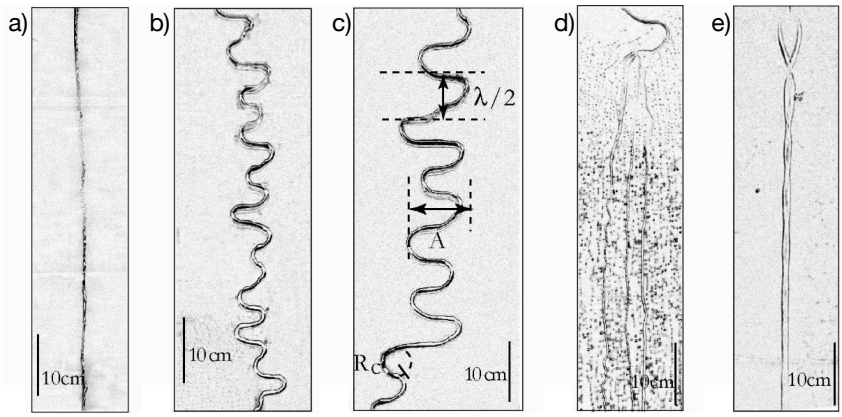

Figure 1.12: Evolution of rivulet morphology as the flow rate increases from left to right. At low flow rates, the rivulet follows a straight down slope path (a). As the flow increases, it develops steady meanders (b–c), which, if we still increase the flow rate, eventually become unstable and break intermittently (d). At very high flow rates, the meander restabilizes, but its width now varies with the down slope distance (e). Pictures from [27].

known as pearling. These satellite droplets remain on the surface while the main droplet moves forward. This process regulate the weight of the drop and thus its speed, the droplet slows down until its rear transition back to a corner. The result is a self-regulating regime that balances mass and speed in real time.

As their speed increases, a series of drops no longer remain independent. They coalesce into continuous streams, a transition driven by energy minimization [48]. Initially, the rivulet forms a straight line along the path of steepest descent. At these low flow rates, surface tension acts like a stretched elastic band, resisting lateral deformation. The contact line remains pinned to surface features, stabilizing the liquid thread [16].

As flow increases, this balance becomes more fragile. Small disturbances, caused by surface defects or flow-rate fluctuations, can destabilize the straight rivulet. The result is a smooth, sinusoidal path: the rivulet meanders. These stationary curves reflect a new balance, where inertial forces are strong enough to challenge pinning and surface tension, but not yet disruptive. The meandering path takes time to settle, but once formed, it persists [16].

With further increase in flow, inertia overtakes stabilizing forces. The rivulet begins to oscillate laterally in real time, losing coherence. It may fragment into sub-rivulets or break up entirely. This dynamic regime reflects a breakdown of order: momentum and fluctuations drive irregular motion, overwhelming surface tension and pinning [16, 49, 50, 51].

Surprisingly, at even higher flow rates, order re-emerges. The rivulet widens, straightens, and stabilizes again, though its edges may undulate slightly. The result is a braided structure, more stable due to the increased volume and contact area [52].

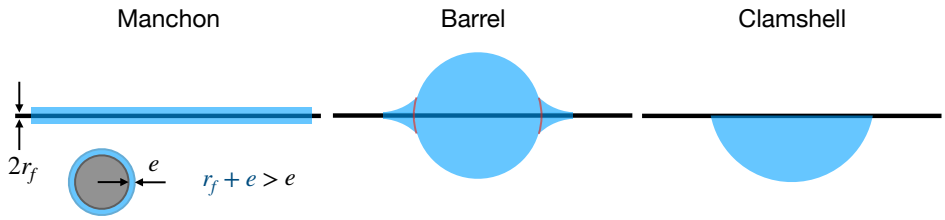

Figure 1.13: Typical liquid morphologies on a fiber. Depending on the balance between capillarity, droplet volume, and fiber radius, the liquid either forms a complete wetting film (manchon) (left), a barrel droplet featuring a inflexion point in red (center), or a clamshell droplet that contacts only part of the fiber circumference (right).

If the flow rate is then reduced, the system exhibits hysteresis. The rivulet narrows but retains its meandering path. Even below the flow threshold where meanders first formed, the pattern persists. This hysteresis is due to contact line pinning, which now resists the return to a straight path [16].

1.5 Droplet on an horizontal fiber

1.5.1 Geometries

Spreading inhibition

When a droplet rests on a flat solid, a positive spreading coefficient S ensures that the liquid spreads into a thin film. On a fiber, however, even for $S > 0$, a droplet may not spread. Brochard *et al.* [53] showed that on a curved substrate, spreading requires S to exceed a critical threshold S_c. The reason lies in geometry: as the liquid spreads along a cylindrical fiber, the liquid–air interface, proportional to $(r_f + e)$ where r_f is the fiber radius and e the film thickness, increases faster than the liquid–solid contact area, proportional to r_f. The extra interfacial area raises the total energy and suppresses spreading unless the gain in solid wetting compensates for it. The critical condition for spontaneous spreading is

$$S_c = \frac{3}{2}\sigma \left(\frac{r}{r_f}\right)^{2/3}, \tag{1.37}$$

where r is the molecular size of the liquid. If this criteria is met, the fluid wet the fiber and forms a manchon, as illustrated in Figure 1.13.

Droplet geometries

Depending on liquid properties, droplet volume, and fiber diameter, droplets adopt one of two distinct shapes (Figure 1.13). Large droplets or thin fibers favor an axisymmetric barrel shape, in which the liquid wraps around the fiber. Smaller droplets or thicker fibers form a clamshell shape, contacting only part of the circumference.

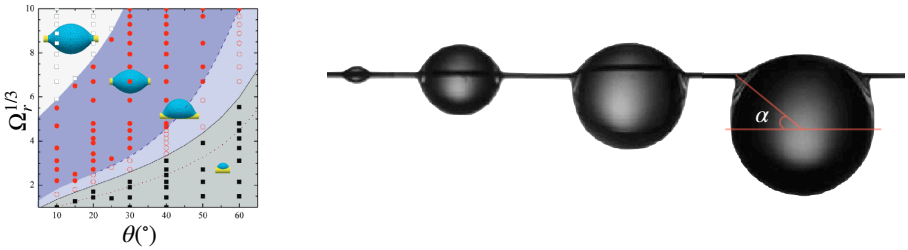

Figure 1.14: (Left) Equilibrium droplet morphologies on a fiber as a function of the reduced volume $\Omega_r^{1/3}$ and the contact angle θ. Transitions between these shapes occur as these parameters vary [59]. (Right) Evolution of a barrel-shaped droplet under increasing gravitational load: the droplet lowers its center of mass, breaking the initial barrel symmetry, until detachment [17].

Carroll [54] solved the Laplace equation for the barrel configuration

$$\Delta P = \sigma \left(\frac{1}{R_1} + \frac{1}{R_2} \right), \tag{1.38}$$

with R_1 and R_2 are the principal radii of curvature at a point in the surface. They neglected gravity and derived an analytical profile satisfying the contact-angle boundary condition. McHale *et al.* [55] used this solution to compute the surface free energy,

$$F = \sigma A_{LA} + (\sigma_{SL} - \sigma_{SA}) A_{SL}, \tag{1.39}$$

where A_{LA} and A_{SL} are the liquid–air and liquid–solid interfacial areas. Barrel droplets exhibit an inflection point along the profile, marked in red on Figure 1.13. This proves that even usual wetting liquids can form stable droplets with zero apparent contact angle on a fiber, in agreement with Brochard's prediction. The clamshell shape, by contrast, cannot be obtained analytically under constant pressure and must be computed numerically [56, 57, 58].

Measuring a contact angle on a fiber is far more challenging than on a flat surface. The tangent to the droplet profile is often ill-defined because of the inflection point. McHale *et al.* [55] derived an expression for the inflection angle θ_i,

$$\tan\theta_i = \pm \frac{n-a}{2\sqrt{an}}, \qquad a = \frac{n\cos\theta - 1}{n - \cos\theta}, \tag{1.40}$$

where n is the ratio of the maximum droplet radius to the fiber radius. The inflection and contact angles coincide only when $n = (1+\sin\theta)/\cos\theta$. In all other cases, they differ, and any experimental measurement based on the droplet tangent likely yields an apparent value between the two.

Roll-up transition

Changing the droplet volume Ω, fiber diameter $2r_f$, or contact angle can induce a roll-up transition, where the droplet wraps around the fiber. Increasing the reduced volume $\Omega_r = \Omega/r_f^3$ promotes the transition from clamshell to barrel, while larger contact angles favor clamshells [60, 61]. Several criteria define the boundary between these regimes. Carroll's metastability criterion, based on Laplace equation identifies the point where pressure perturbations change sign

$$2n^3\cos\theta - 3n^2 + 1 = 0. \tag{1.41}$$

McHale's inflection criterion [55, 57, 58] assumes the transition occurs when the inflection angle equals the contact angle

$$n = 1 + \frac{\sin\theta}{\cos\theta}. \tag{1.42}$$

Finally, a free-energy criterion directly compares the energies of both shapes using Surface Evolver[58]. The resulting stability map (Figure 1.14) defines regions where clamshells, barrels, or both coexist. The coexistence region, within the dotted lines, corresponds to cases where each shape represents a local energy minimum, explaining why experiments often observe both configurations under similar conditions [59].

Gravity effects

When droplets become larger than the capillary length, gravity deforms their shape, transforming barrel profiles into downward-elongated barrels and clam-shells into downward-slanted configurations (Figure 1.14(right)). It may ultimately cause detachment. Lorenceau *et al.* [17] studied the balance between capillary and gravitational forces for oil droplets on horizontal fibers. The droplet detaches when the vertical component of capillary forces, $4r_f\sigma\cos(\alpha/2)$ equals the weight $4\pi\rho g R^3$, with α the angle made by the segment joining the center of the drop and the fiber/drop intersection, as illustrated in Figure 1.14. This yields a critical angle

$$\sin(\alpha) = \frac{1}{3}\frac{r^3\lambda^2}{r_f}, \tag{1.43}$$

and thus a critical drop radius R_d for detachment

$$R_d = \left(\frac{3r_f}{\lambda}\right)^{1/3}. \tag{1.44}$$

Including gravity in numerical models [59] barrel shapes only exist within coexistence zones with clamshell.

1.5.2 Fiber coating

LLD theory

When a fiber is pulled from a liquid, either vertically or horizontally, a thin film of fluid adheres to its surface. The film's final thickness is set by a narrow region near the liquid surface, shown in Figure 1.15, known as the dynamic meniscus of length λ. In this zone, viscous forces draw liquid upward while surface tension resists interface deformation. The balance between these two effects determines the thickness of the deposited film [62].

To quantify this balance, we consider the viscous shear generated by the moving fiber and the pressure gradient arising from the curvature of the interface. The capillary pressure across a film of thickness h coating a fiber of radius r scales as $\Delta P \sim \sigma/r$ if $h \ll r$. In steady motion, this pressure gradient is balanced by viscous stresses, yielding

$$\frac{\eta V}{h^2} \sim \frac{\sigma}{r\,\lambda}, \tag{1.45}$$

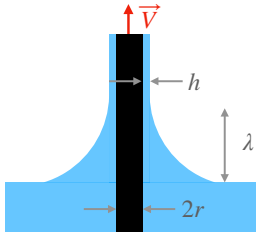

Figure 1.15: A fiber of radius r is withdrawn from a bath at constant velocity $\vec{V}$. As it rises, it entrains a liquid film of thickness h. Near the reservoir, a dynamic meniscus of height λ forms at the interface.

where λ denotes the length of the dynamic meniscus. At this stage, λ is unknown: it must depend on both the geometry and the withdrawal speed.

To determine it, the Landau–Levich–Derjaguin theory [63] introduces a matching condition between the static meniscus in the bath and the dynamic meniscus near the coated region. In the static meniscus, the Laplace pressure vanishes when r is smaller than the capillary length. In the dynamic one, however, the interface curvature contains two contributions: one due to the fiber itself and one due to the bending of the liquid profile. Balancing these two terms gives

$$\frac{\sigma}{r+h} - \frac{\sigma h}{\lambda^2} \sim 0. \tag{1.46}$$

For thin films ($h \ll r$), this reduces to a remarkably simple relation

$$\lambda \sim \sqrt{h\,r}. \tag{1.47}$$

This result captures the geometry of the problem: the dynamic meniscus extends over a length that is the geometric mean of the fiber radius and the film thickness.

Substituting Equation (1.47) into the viscous–capillary balance (Equation (1.45)) removes λ and leaves a single equation for h:

$$\frac{\eta V}{h^2} \sim \frac{\sigma}{r\sqrt{h\,r}}. \tag{1.48}$$

Solving for h yields

$$h \sim r\,\mathrm{Ca}^{2/3}, \tag{1.49}$$

and correspondingly,

$$\lambda \sim r\,\mathrm{Ca}^{1/3}. \tag{1.50}$$

A full asymptotic analysis refines these dimensional arguments and provides the numerical prefactor [64]

$$h = 1.34\,r\,\mathrm{Ca}^{2/3}. \tag{1.51}$$

This expression, verified experimentally, encapsulates how curvature, viscosity, and surface tension combine to determine the coating thickness on a fiber.

Although the LLD law captures the essence of viscous–capillary coating, the relationship between withdrawal speed and film thickness is far from universal. Depending on the operating conditions, a much wider variety of behaviors can

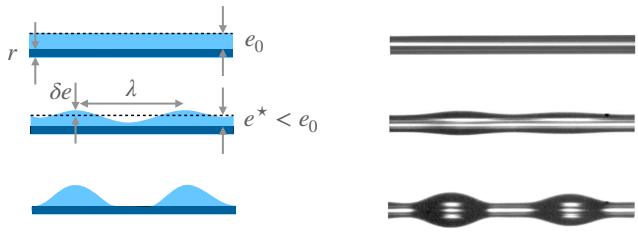

Figure 1.16: Plateau-Rayleigh instability: a liquid sheath gradually destabilizes under surface tension, breaking up into a sequence of droplets that reduces the interfacial area. Images from [69].

emerge. Gravity limits film thickness on larger fibers [65], partial wetting delays it until a threshold velocity is reached [66], and inertia at high speeds can either thicken or suppress the coating altogether [67, 68] . As a result, the film thickness does not vary monotonically with velocity but follows a complex curve shaped by these competing effects.

Plateau-Rayleigh instability

Once a liquid coats a fiber of radius r_f, the story is not over. With time, the initially smooth film rarely remains uniform: it starts to undulate and eventually breaks into a chain of droplets, as shown in Figure 1.16. This transformation, known as the Plateau–Rayleigh instability, arises naturally in liquid cylinders such as fibers wrapped in a thin fluid sheath [23]. The straight coating develops long-wavelength modulations whose amplitude gradually grows until the film pinches off into a regular necklace of drops.

The mechanism is purely geometric. On a cylindrical surface, a sufficiently long undulation reduces the total surface area for a fixed liquid volume, thereby lowering the interfacial energy. To illustrate this, let the local film thickness vary as

$$e = e^* + \delta e \cos(qx), \tag{1.52}$$

where volume conservation imposes $e^* < e_0$. A simple calculation gives

$$e^* = e_0 - \frac{\delta e^2}{4(r_f + e_0)}. \tag{1.53}$$

Assuming weak undulations, the surface energy per wavelength changes by

$$\Delta E = \frac{\pi}{2}\lambda\sigma \frac{(\delta e)^2}{r_f + e_0}\left(q^2(r_f + e_0)^2 - 1\right), \tag{1.54}$$

which decreases ($\Delta E < 0$) whenever $q(b + e_0) < 1$, or equivalently when the wavelength exceeds the cylinder's circumference,

$$\lambda > 2\pi(r_f + e_0). \tag{1.55}$$

This simple criterion, first verified by Plateau in the nineteenth century, marks the onset of instability: only disturbances longer than the cylinder's perimeter can grow.

To capture how the breakup evolves, we focus on the thin-film limit ($e_0 \ll b$), where viscosity dominates inertia. In this regime, the flow results from the competition between capillary pressure, which amplifies curvature variations, and viscous dissipation, which resists them. Linearizing the hydrodynamic equations for this Poiseuille-type flow shows that perturbations grow when $qb < 1$, consistent with the geometric condition above. Among all unstable modes, the wavelength that grows fastest is

$$\lambda^* = 2\pi\sqrt{2}\, r_f, \tag{1.56}$$

with a characteristic growth time

$$\tau^* = 12\frac{\eta r_f^4}{\sigma e_0^3}. \tag{1.57}$$

This timescale can range from seconds to hours depending on the film thickness and viscosity: for instance, a 1 μm oil film ($\sigma/\eta = 0.1\,\mathrm{m/s}$) on a 100 μm fiber may take several hours to rupture, whereas a 10 μm coating breaks up within about ten seconds.

1.6 Drop on an inclined fiber

Huang [70] showed that a droplet on an inclined fiber (of radius r_f) may remain static. He attributed this stability to surface roughness, which delays motion similarly to pinning on inclined planes. Additionally, he identified a critical volume below which droplets can stay pinned even on vertical fibers given by

$$V_c = \frac{4\pi r_f\, \sigma}{\rho g}. \tag{1.58}$$

If we now look at droplet motion, Gilet [18] investigated it on vertical fibers and highlighted a transition in droplet geometry during descent. Initially, the droplet may adopt a clamshell shape, where gravity favors asymmetric spreading on one side of the fiber. However, as the droplet slides downward, it continuously loses volume by depositing a thin film on the fiber surface (LLD law). This volume loss ultimately favorises the emergence of a more symmetric barrel morphology. This transition causes a noticeable decrease in droplet speed due to the abrupt enlargement of the dissipation surface, as visible on Figure 1.17(left).

To describe the barrel droplet's dynamics, Gilet modeled its motion using Newton's second law applied to the center of mass

$$\rho\Omega\frac{dV}{dt} = \rho\Omega g - F_\nu, \tag{1.59}$$

where ρ is the fluid density, Ω is the droplet volume, g is gravitational acceleration, and F_ν is the viscous friction force. The viscous force is given by

$$F_\eta = 2\xi\eta r_f v, \tag{1.60}$$

where η is the fluid viscosity, d the fiber diameter, v the droplet speed, and ξ a geometric coefficient depending on the droplet's shape. This coefficient is expressed as

$$\xi = \pi C_v \gamma \frac{L}{l}, \tag{1.61}$$

where L and l are the droplet's length and width, γ a shape factor, and C_v a dimensionless drag coefficient (typically of order 1 for cylindrical geometries).

The time required to reach terminal velocity can be estimated by

$$t \simeq \frac{V}{g}, \tag{1.62}$$

which, for an initial speed of 1 m/s, gives approximately 0.1 s. This implies that the force balance is established almost immediately, allowing the inertial term to be neglected. Newton's equation then simplifies to

$$0 = \rho\Omega g - F_\nu, \tag{1.63}$$

leading to an expression for the terminal velocity $\dot{z} = v$

$$\dot{z} = \frac{1}{\xi}\frac{\rho g}{\eta}\frac{\Omega}{2r_f}. \tag{1.64}$$

Since the droplet leaves a film as it descends, its volume decreases over time. The rate of this volume loss is given by

$$\dot{\Omega} = -2\pi r_f \, e\dot{z}, \tag{1.65}$$

where e is the film thickness, determined by LLD theory. By combining this equation with the expression for $\dot{z}$ and solving the resulting differential equation, Gilet obtained an analytical expression for the droplet position $z(t)$ as a function of time

$$z = \frac{\dot{z}_0^{1/3} - \left(\dot{z}_0^{-2/3} + \frac{2}{3}wt\right)^{-1/2}}{w/3}, \tag{1.66}$$

where $\dot{z}_0$ is the initial speed of the droplet and w is a parameter depending on the physical and geometric properties of the system

$$w = \frac{c_{\text{dry}}}{C_v}\frac{l}{L}\left(\frac{\eta}{\sigma}\right)^{2/3}\frac{2\rho g r_f}{\eta}. \tag{1.67}$$

The model, when compared to experimental data, successfully reproduces the evolution of droplet position and velocity over time when c_{dry} is adjusted, confirming the critical role of viscous dissipation, volume loss, and shape transition in governing the dynamics of sliding droplets on vertical fibers.

1.6.1 Flow on a fiber

When a droplet flows down a vertical fiber, the smooth coating deposited at the top often evolves into complex interfacial patterns (Figure 1.17(right). At rest, a cylindrical film is intrinsically unstable and eventually break into droplets [25, 24]. Yet, once the film is in motion, this instability can be delayed or even suppressed.

At moderate flow rates, fluid convection along the fiber competes with capillary breakup. When the convective timescale becomes shorter than the instability growth time, the film remains continuous, displaying only weak, bounded oscillations [72, 73, 74]. Increasing the flow rate further, the system transitions through a series

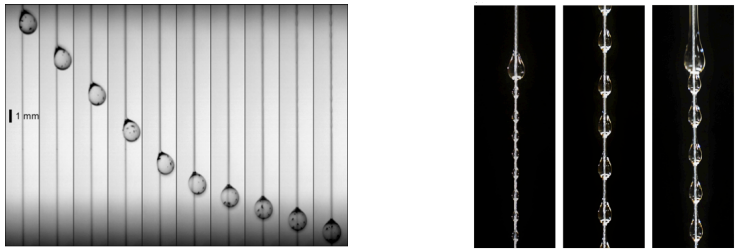

Figure 1.17: (Left) Experimental image of an initially clamshell-shaped droplet descending along a vertical fiber, transitioning to the barrel shape (the stable configuration). The change in shape induces a sudden decrease in vertical speed [18]. (Right) Different flow pattern on a vertical fiber as function of the flow rate [71].

of regimes: from isolated, slow-moving drops separated by thin films, to regular trains of droplets, and eventually to a continuous, wavy film with unpredictable coalescence in between droplets [75, 76].

Beyond flow rate, other parameters also shape the morphology. The fiber radius, liquid surface tension, and even small asymmetries, such as wind cross flow or nozzle geometry, can trigger transitions between axisymmetric (barrel-like) and asymmetric (clamshell) configurations [71, 77, 78, 79]. These studies reveal that even a simple geometry, a liquid film on a vertical fiber, can host a remarkable diversity of flow patterns, governed by subtle balances between capillarity, gravity, and viscous flow.

1.7 Multiple fibers

When multiple fibers interact with a liquid, their geometry defines how capillary forces shape, retain, or transport water. A single droplet on one fiber can only adopt a limited range of morphologies, but when fibers are brought together, confinement, orientation, and flexibility unlock new modes of liquid organization. Across a range of configurations, from parallel to twisted, crossed, and flexible fibers, research has shown how geometry acts as a lever to tune liquid behavior, offering control over shape, motion, and structure.

In the simplest configuration of parallel fibers (Figure 1.18(a)), spacing alone determines whether a droplet remains compact or stretches into a column bridging the gap between them [80]. As spacing decreases, curvature differences drive a transition from a discrete droplet to a continuous filament. When such fibers are oriented vertically (Figure 1.18(b)), gravity transforms these static bridges into steady flows [85]. At higher flow rates (Figure 1.18(c)), distant fibers introduce a new regime where the liquid forms stable sheets in between [81].

Introducing fiber twisting creates a helical groove (Figure 1.18(d)). Droplets placed on such twisted pairs follow the helical path while rotating and descending [86]. The motion transitions from pure helicoidal to mixed helicoidal-skipping regimes when the droplet length exceeds the pitch length. At larger scales, twisting enhances drainage and stabilizes asymmetric droplet shapes [82]. Depending on droplet volume and twist wavelength, three regimes may emerge: helicoidal, skipping, and barrel flow.

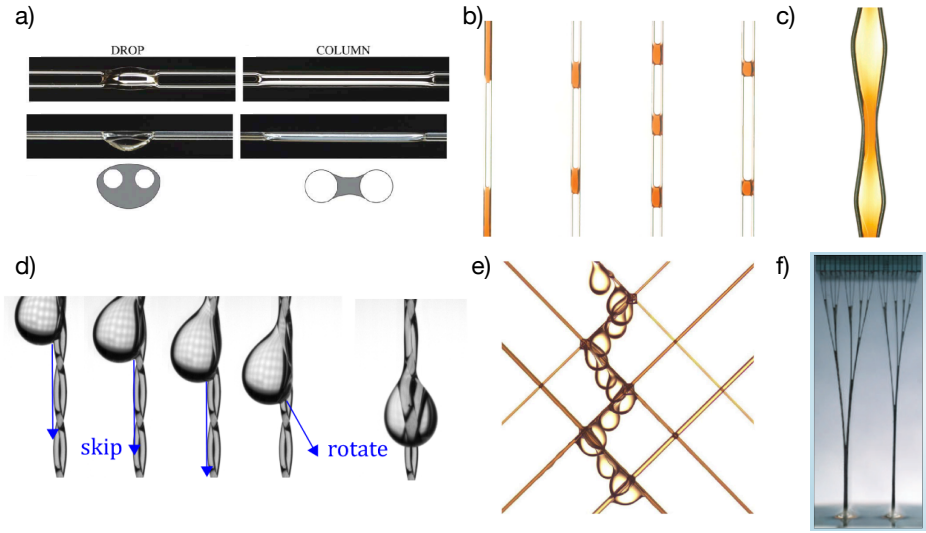

Figure 1.18: (a) Drop–to–column transition between parallel horizontal fibers [80]. (b) Effect of inter-fiber spacing on liquid morphology between vertical fibers, from elongated bridges to small drops [81]. (c) Formation of a self-sustained liquid sheet with thickness variations between closely spaced fibers [81]. (d) Helical droplet trajectories on twisted fibers created by a capillary groove [82]. (e) Droplet routing and switching at crossed fibers of different radii [83]. (f) Elastocapillary collapse of flexible fibers into hierarchical bundles under capillary forces [84].

At fiber crossings, geometry defines not only motion but also retention. On a single bent fiber as on fibers crossing, the angle controls the maximum droplet volume supported before detachment [87]. At multi-fiber junctions, cooperative anchoring between fibers allows large droplets to remain suspended below the hub [88]. Beyond static retention, capillarity at crossings can be exploited for routing and redistribution. By adjusting fiber orientation and size, droplets can be guided, merged, or split across intersections [89, 83] (Figure 1.18(e)). Asymmetries in spacing further enable directed motion, where droplets migrate toward narrower gaps or apexes under capillary pressure gradients [90].

Finally, when the fibers themselves are elastic, the liquid not only responds to the structure but also reshapes it (Figure 1.18(f)). Capillary forces can pull parallel flexible fibers together, leading to self-assembly through elastocapillary coupling [91, 92]. Depending on droplet volume and spacing, the system transitions from no spreading to partial or full collapse into a column. The same principle governs bundling in wet hair, where surface tension overcomes bending stiffness once the elastocapillary length

$$L_{\mathrm{EC}} = \sqrt{\frac{B}{\sigma}} \tag{1.68}$$

with B the bending modulus is exceeded [93]. Extending this interaction to large arrays, solvent evaporation can drive controlled bending and clustering of vertical pillars into complex three-dimensional architectures [94].

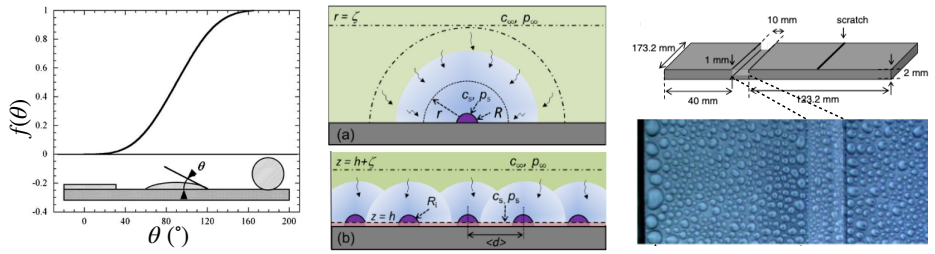

Figure 1.19: (a)Function $f(\theta)$ impacting nucleation energy barrier during heterogeneous nucleation. Even moderately hydrophilic substrates ($\theta < 90°$) substantially reduce the barrier compared to homogeneous nucleation. (b) Early growth of isolated droplets and subsequent overlap of their diffusion fields as surface coverage increases. (c) Edge effects: droplets located along outer edges or corners grow faster due to enhanced vapor supply, while those in inner corners or grooves grow more slowly.

1.8 Condensation

1.8.1 Nucleation

Homogeneous and heterogeneous

From a thermodynamic viewpoint, nucleation corresponds to the spontaneous formation of a liquid embryo within a supersaturated vapor. The driving force of the process is the excess chemical potential between vapor and liquid phases, which increases with the degree of supersaturation $S = p/p_{\text{sat}} > 1$. The creation of a liquid nucleus of radius r involves a competition between two terms: the gain of volumetric free energy due to condensation and the energetic cost of creating a liquid–vapor interface. In the homogeneous case, the total free-energy change ΔG_{hom} is expressed as

$$\Delta G_{hom}(r) = 4\pi r^2 \sigma - \frac{4}{3}\pi r^3 \frac{k_{\text{B}} T \ln S}{v_{\text{m}}}, \tag{1.69}$$

where k_{B} is the Boltzmann constant and v_{m} the specific volume of molecules in the liquid phase. The first term penalizes small droplets by the creation of new interface, while the second favors growth by the phase change. The extremum of the Gibbs free energy curve defines the critical radius,

$$r_c = \frac{2\sigma v_{\text{m}}}{k_{\text{B}} T \ln S}. \tag{1.70}$$

Below this critical radius, nuclei are thermodynamically unstable and re-evaporate, and above which they grow spontaneously. Because r_c decreases only logarithmically with supersaturation, extremely high S values are required for homogeneous nucleation in pure vapor [95].

In practice, condensation occurs almost exclusively by heterogeneous nucleation, where preexisting surfaces or particles lower the energy barrier for phase transition. When a nucleus forms on a solid substrate, the system no longer needs to create a complete spherical interface; the liquid–solid contact reduces the required surface energy by a factor depending on the contact angle θ. The associated energy barrier

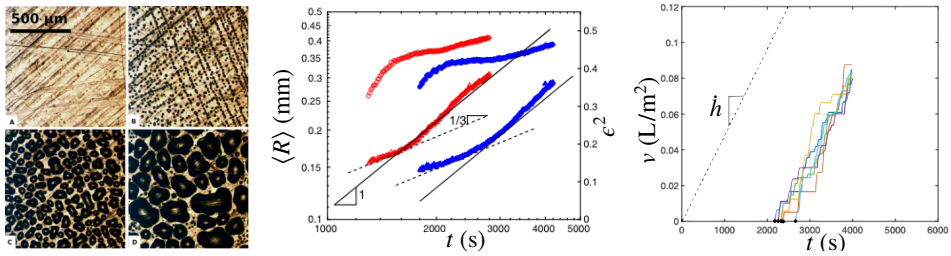

Figure 1.20: Evolution of condensation on a cooled surface. (Left) Nucleation begins at surface defects, after which droplets grow by vapor adsorption and coalescence, progressively forming larger clusters. (Center) Mean droplet radius $\langle R \rangle$ exhibits two growth regimes: a collective-diffusion regime with $\langle R \rangle \sim t^{1/3}$, followed by a coalescence-dominated regime with $\langle R \rangle \sim t$. During coalescence, the surface coverage ε^2 rises and saturates at $\varepsilon^2 \approx 0.5$. Rough surfaces (red) fastens the process compared to smooth one (blue). (Right) Water collected at the lower edge as a function of time shows a constant condensation rate $\dot{h}$, set by the cooling power of the plate rather than by surface chemistry or micro texture.

in the heterogeneous case ΔG_{het} becomes

$$\Delta G_{\text{het}} = f(\theta)\, \Delta G_{\text{hom}}, \tag{1.71}$$

with

$$f(\theta) = \frac{1}{4}(2 + \cos\theta)(1 - \cos\theta)^2. \tag{1.72}$$

This function is represented in Figure 1.19(a). Even modestly hydrophilic defects or impurities ($\theta < 90°$) thus dramatically favor droplet appearance. This explains why condensation preferentially starts on microscopic scratches, dust, or chemical heterogeneities [96, 97], as visible on Figure 1.20(a)

Growth

Once droplets have nucleated, their size increases through condensation of surrounding vapor. The rate of growth depends on how vapor diffuses toward each droplet and how neighboring droplets interact. Four main regimes can be identified, each characterized by a power-law relation between droplet radius and time, $R \sim t^{\alpha}$, where the exponent α reflects the dominant growth mechanism.

At the beginning, droplets are sparse and act as isolated sinks of vapor, as represented in Figure 1.19(center). Each droplet captures molecules independently within its own spherical diffusion field, leading to a growth law $R \sim t^{1/2}$. This corresponds to diffusion-limited growth without interference from neighbors.

As condensation progresses, droplets dispersion become denser and their vapor diffusion fields begin to overlap, illustrated in Figure 1.19(center). The local vapor supply to each droplet is then reduced, and growth slows down to $R \sim t^{1/3}$, experimental measures of this regime [96] are plotted in Figure 1.20(center). This regime represents collective diffusion, where droplets compete for vapor arriving through a boundary layer of finite thickness $\zeta \approx 2\,\text{mm}$.

Once droplets start to coalesce, the number of droplets decreases while their average size increases, as visible in Figure 1.20(a). The overall surface coverage remains roughly constant, and the pattern evolves in a self-similar manner. In this regime, the mean droplet radius grows linearly in time, $\langle R \rangle \sim t$, reflecting

the dominance of coalescence over individual diffusion [98, 99, 96]. This regime is also represented in Figure 1.20(b). In the same graph, the author represented the surface coverage that appear constant and approximately equal to $\epsilon \approx 0.5$ once in this regime.

As coalescence progresses, larger droplets tend to appear first near the substrate boundaries, as clearly visible in Figure 1.19(c). Edges and corners access a bigger vapor field, allowing vapor to diffuse from several directions and thereby enhancing the local concentration gradient. This leads to faster growth at outer edges and corners, while droplets confined in inner edges or grooves grow more slowly due to reduced vapor access. The effect diminishes when condensation becomes limited by heat transfer, as on low-conductivity materials [99]. Because edge droplets reach the detachment size earlier [96], they often initiate shedding event, bridging the coalescence regime with the emergence of drainage.

Latent heat

Condensation releases latent heat at the droplet–air interface. For water at ambient conditions ($T \approx 25°\mathrm{C}$, $p = 1\,\mathrm{atm}$), the latent heat of vaporization is

$$L = 2.4\ 10^6\,\mathrm{J\,kg^{-1}} \tag{1.73}$$

For condensation to continue, this heat must be removed efficiently through the droplet and the underlying substrate. If it is not evacuated fast enough, the local surface temperature increases, the vapor supersaturation decreases, and growth slows down. In many practical situations, thermal transport therefore becomes the primary limiting factor. This manifests as a constant condensation rate $\dot{h}$, as shown in Figure 1.20(c), which is set by the cooling power of the plate rather than by surface chemistry or micro texture. While the substrate's composition and patterning influence how much liquid is retained on the surface in steady state (horizontal offset from the dotted line), there is no evidence that they significantly modify the condensation rate itself (the slope)[100, 101].

1.9 Atmospheric water harvesting (AWH)

1.9.1 Fog harvesting

Formation and characteristics

Fog forms when atmospheric and surface conditions bring moist air to saturation. Two mechanisms dominate. Advection fog develops when warm, humid air travels over a cooler surface and cools below its dew point, a common event when marine air moves inland [102]. Radiative fog arises through nocturnal ground cooling: under clear skies and calm winds, the surface loses heat, cooling the adjacent air until condensation occurs [103].

Fog is most likely to form when relative humidity is high, dew-point temperature is elevated, and ambient air temperatures are low. Such conditions frequently occur in coastal and mountainous regions, where moist air masses and topographical uplift promote persistent fog [104]. These areas therefore offer particularly favorable environments for passive fog-collection technologies.

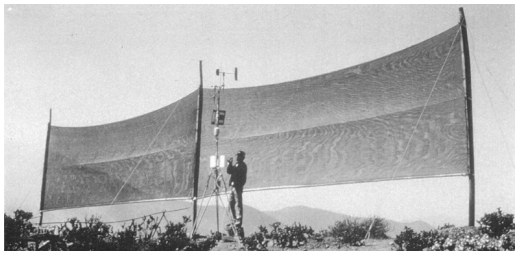

Figure 1.21: Fog harvesting installation in El Tofo, Chile, where 75 large vertical mesh collectors supply potable water to a remote village [112].

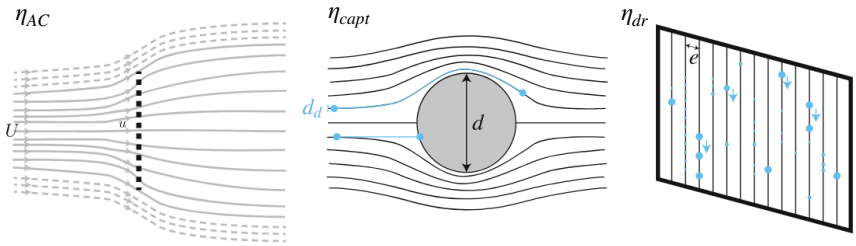

Figure 1.22: Schematic illustration of the physical mechanisms governing fog collection efficiency $\eta_{\text{coll}} = \eta_{\text{AC}} \cdot \eta_{\text{capt}} \cdot \eta_{\text{dr}}$. (Left) The aerodynamic coefficient η_{AC} reflects airflow interaction with a vertical fog net, illustrating the trade-off between aerodynamic passage and droplet interception. (Center) The capture coefficient η_{capt} describes the behavior of a droplet depending on its Stokes number : one follows streamlines and bypasses the mesh, while the other impacts a fiber due to its inertia. (Right) The drainage coefficient η_{dr} quantifies how efficiently collected water drains into storage, accounting for pinning, evaporation, and re-entrainment. Schematics from [7].

Fog is composed of water droplets with diameters typically ranging between 1 and 50 μm [105]. The most common metric to quantify fog's water-bearing capacity is the Liquid Water Content (LWC), which is generally of the order of 1 g/m^3 [106].

Ecologically, fog can serve as a crucial water source. In California's redwood forests, it provides up to 40 % of the water used by trees during dry periods [107]. In the coastal rain forests of Chile, fog water input may even exceed rainfall [108]. Similarly, in arid regions like the Namib Desert, organisms such as the fog-basking beetle rely on fog capture to survive [109].

Yet this resource is fragile. Deforestation can reduce fog frequency by disrupting microclimates [110], and climate change may alter wind patterns and temperature profiles in ways that reduce fog reliability [111].

Harvesting

Fog collection has been implemented in several arid and semi-arid regions as a low-tech, decentralized water source, particularly where conventional options are logistically or economically prohibitive. A notable example is found in El Tofo, Chile, where a network of 75 large fog nets (each 48 m^2) provided clean water to a village of 330 people. With yields averaging 3 L m^{-2} day^{-1}, the system delivered about 11 000 L/day, covering more than double the community's previous supply from trucked water [112]. Similar systems have supported reforestation efforts by maintaining soil moisture in degraded mountain regions [113].

The collection device is a vertical mesh, the fog net, that intercepts droplet-laden air and channels collected water into storage. The effectiveness of a fog net η_{coll} depends on how well it let air pass through η_{AC}, while capturing η_{dr}, and draining fluid η_{dr}. These physical mechanism are quantified through three key coefficients:

$$\eta_{\text{coll}} = \eta_{\text{AC}}\,\eta_{\text{capt}}\,\eta_{\text{dr}} \tag{1.74}$$

The aerodynamic coefficient η_{AC} (Figure 1.22(left)) can be approximated as [114]

$$\eta_{\text{AC}} = \frac{s}{1+\sqrt{C_o/C_d}}, \tag{1.75}$$

with the shading coefficient (the part of the collector's area capable of capturing droplets), C_o the pressure drop coefficient for the mesh and C_d the drag coefficient. This coefficient represent the fraction of droplets diverted toward the mesh in airflow. It depends on mesh porosity (shade coefficient). If the mesh is too dense, airflow is deflected; if too sparse, droplets pass through. Optimal shade coefficients are around 55 %.

The capture coefficient η_{capt} is the mesh's ability to retain impinging droplets [115] (Figure 1.22(center))

$$\eta_{\text{capt}} = \frac{\text{St}}{\text{St}+\pi/2} \quad \text{with} \quad \text{St} = \frac{2\rho \mathrm{r}_{\text{fog}}^2 \mathrm{v}}{9\eta \mathrm{r}_{\text{f}}}, \tag{1.76}$$

where St is the Stokes number, r_{fog} is the typical radius of a fog droplet, v is the flow speed, r_f is the fiber radius. The Stokes number St compares droplet inertia to viscous drag. For small St, viscous forces dominate and droplets closely follow the airflow, allowing them to pass around the fibers. For large St, inertia dominates and droplets deviate from streamlines, increasing the likelihood of collision with the mesh. Superhydrophilic coatings further improve capture by promoting adhesion and spreading upon impact, thereby reducing droplet re-entrainment into the airflow [115].

And finally, the drainage coefficient η_{dr} measures the fraction of collected water that successfully drains to storage (Figure 1.22(right)). Losses arise from evaporation, droplets trapped within the mesh (clogging), or re-entrainment by the airflow. Hydrophobic and superhydrophobic coatings enhance drainage efficiency by reducing pinning and shortening droplet residence time on the mesh [115].

Recent innovations include multi-layer meshes [114], kirigami-inspired geometries [116, 117, 118], hanging spine-based [119] or concave designs [114]. Because wind direction can significantly affect performance, circular [120] and Eiffel-like designs [110] have been developed to enable omnidirectional collection. At the microscale, surface microtexturing can reduce drag, enhancing the net's aerodynamic performance [121].

Mesh geometries that prevent clogging, such as harp-like designs, also reduce shade coefficient increases, though they require adequate structural support to avoid tangling [4, 122]. A well-designed mesh that prevents tangling and ensures good drainage is less prone to accumulate water that would otherwise evaporate or degrade collection efficiency [123].

Fog harvesting performance varies widely with local climate and seasonality. Typical yields are $5\,\mathrm{L\,m^{-2}\,day^{-1}}$ [104], though under optimal coastal conditions

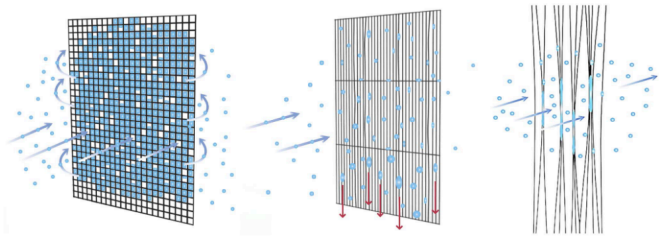

Figure 1.23: (Left) Square-mesh collectors are prone to clogging, which reduces both aerodynamic transmission (η_{AC}) and drainage efficiency (η_{dr}) by retaining water. (Center) Fibrous or long-strand collectors can suffer from tangling, disrupting airflow and reducing the effective shade coefficient. (Right) Hybrid geometries that combine long vertical fibers with support vertical ones mitigate both issues by preserving airflow while promoting drainage, leading to more stable and efficient fog harvesting.

(e.g., in Oman), collection rates as high as $45\,\mathrm{L\,m^{-2}\,day^{-1}}$ have been reported [124]. Material costs are relatively low: a $40\,\mathrm{m^2}$ mesh system costs about 3000 euro, yielding 200 L/day on average, competitive in isolated regions where water must be trucked in [125, 112].

Nevertheless, fog collection faces several challenges. Geographically, its applicability is limited to areas with frequent and dense fog, often near coastlines or mountainous regions. Weather conditions can also compromise system durability: strong winds may tear the mesh structure, and prolonged exposure to UV radiation accelerates material degradation [126]. On the human side, a lack of regular maintenance can impair system performance over time [126]. Furthermore, water quality can suffer due to turbidity when the system remains inactive for long periods [6], and in industrial zones, captured water may be contaminated by airborne pollutants [103, 127, 128].

These limitations highlight the need for robust design, careful site selection, and continued monitoring to ensure the long-term viability of fog harvesting systems. At the same time, they open the door for improving performance through better understanding of how droplets interact with the mesh structure at small scales, particularly along the fibers that form the backbone of most collector designs.

1.9.2 Dew harvesting

A window to the sky

The Earth's atmosphere, through the greenhouse effect, is largely opaque to infrared radiation. However, it has a spectral window between 8 and 20 μm where its emissivity is exceptionally low. Coincidentally, this range overlaps with the peak thermal radiation of a blackbody at ambient temperature ($T \sim 300\,\mathrm{K}$), making it possible for terrestrial surfaces to radiate heat directly into outer space. As outer space acts as a deep cold sink ($\sim 3\,\mathrm{K}$), this atmospheric window enables passive heat transfer, a mechanism known as radiative cooling[129].

This process becomes especially relevant in dew collection. At night, radiative emission can lower a surface's temperature below the ambient dew point, enabling condensation. During the day, however, maintaining sub-dew point temperatures becomes much more challenging due to strong solar irradiation.

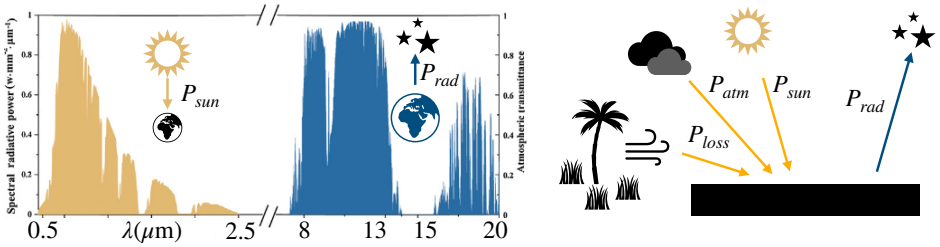

Figure 1.24: (left) Spectral plot of incoming solar irradiance P_{sun} (dominant in the 0.3–2.5 μm range) and thermal emission P_{rad} from a 300 K black body (peaking around 10 μm). Both are partially shielded by the atmosphere. The atmospheric window between 8 and 13 μm allows radiative heat to escape into space. Adapted from [130]. (right) Schematic energy balance at the surface of a radiative cooler, showing all major heat fluxes: emitted thermal radiation (P_{rad}), absorbed solar radiation (P_{sun}), atmospheric back-radiation (P_{atm}), and non-radiative losses (P_{loss}).

Net cooling power

Radiative cooling is governed by an energy balance between incoming and outgoing heat fluxes. The net cooling power is expressed as [130]

$$P_{\text{net}} = P_{\text{rad}} - P_{\text{sun}} - P_{\text{atm}} - P_{\text{loss}}, \tag{1.77}$$

where P_{rad} is the thermal radiation emitted by the surface, P_{sun} is absorbed solar radiation, P_{atm} is absorbed atmospheric and environment infrared radiation, P_{loss} includes conductive and convective heat transfer from the environment. Efficient cooling surfaces aim to maximize P_{rad} while minimizing the other three terms.

All black bodies at non-zero temperature emit thermal radiation according to Planck's law:

$$I(T,\lambda) = \frac{2hc^2}{\lambda^5} \frac{1}{\exp\left(\frac{hc}{\lambda k_{\text{B}} T}\right) - 1}. \tag{1.78}$$

Here, T is the absolute temperature, λ the wavelength, and h, c, and k_{B} are Plank, light speed and Boltzmann constants. The peak emission at $T = 300\,\text{K}$ occurs near $\lambda \approx 10\,\mu\text{m}$, precisely within the atmospheric window. The total radiated power per unit area is given by:

$$P_{\text{rad}} = \varepsilon k_{\text{B}} T^4, \tag{1.79}$$

where ε is the surface emissivity ($\varepsilon = 1$ for a black body). Materials engineered for radiative cooling are designed to have high emissivity in the 8–20 μm range, maximizing heat emission into the transparent part of the sky.

Under clear sky conditions, solar irradiance reaches up to 1000 W/m^2, nearly ten times larger than measured radiative cooling flux. If a surface absorbs even a small fraction of this incoming energy, it can easily overwhelm any cooling gains and lead to dew evaporation. To prevent this, radiative coolers must exhibit low absorptivity (or high reflectivity) in the solar spectrum, especially from 0.3 to 2.5 μm where most solar energy is concentrated.

The atmosphere itself emits infrared radiation due to water vapor, CO_2, and other greenhouse gases. This back-radiation contributes to surface heating. Radiative cooling is most effective under dry, clear-sky conditions, and its efficiency is significantly reduced in humid or cloudy environments, which further reduce the atmospheric transparency window.

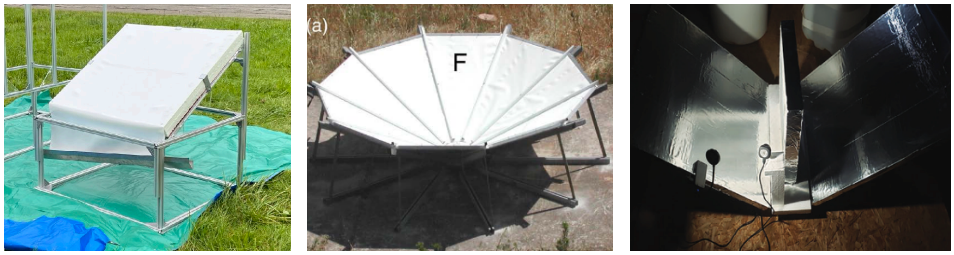

Figure 1.25: Examples of condenser geometries used to enhance dew collection. (left) A traditional flat condenser tilted at 30°, balancing radiative exposure with gravitational drainage. (center) A conical condenser that reduces wind influence and shields the surface from surrounding thermal radiation [131]. (right) A V-shaped radiator in which 45° side mirrors reflect the cold sky onto both faces of a central vertical surface, effectively increasing its radiative exposure and cooling power [132].

Real surfaces are not isolated. They exchange heat with their surroundings via conduction and convection, leading to parasitic heat gains:

$$P_{\text{loss}} \approx h(T_r - T_a), \tag{1.80}$$

where h is the convective heat transfer coefficient, T_r the surface temperature, and T_a the ambient air temperature. Non-radiative losses can be minimized by using thermal insulation or by reducing air flow near the surface.

To achieve sustained dew condensation, radiative coolers must meet the following design criteria: high emissivity in the 8–20 μm atmospheric window, high reflectivity across the solar spectrum to avoid heating, minimal non-radiative coupling with the environment.

Harvesting

Compared to fog harvesting, dew collection is less restrictive in terms of meteorological requirements. It can occur under relatively mild conditions, including moderate humidity and light winds, and is not limited to coastal or high-elevation environments [133, 134]. This broader applicability makes it a potentially versatile water harvesting strategy. However, as with fog collection, dew is sensitive to air quality: the condensed water may contain airborne pollutants or aerosols, especially in urban or industrial settings.

Dew harvesting systems may provide a passive and decentralized method for collecting potable water in regions where conventional sources are scarce or unreliable. The typical configuration consists of a flat and inclined surface, often tilted around 30° to balance gravitational drainage with radiative exposure [135] (Figure 1.25(left)). This geometry allows condensed droplets to flow into a collection tank while maintaining a broad view of the sky to maximize cooling efficiency.

Under favorable conditions, dew collection yields generally range between 0.2 and 0.5 $\mathrm{L\,m^{-2}\,night^{-1}}$, with variations depending on meteorological parameters, site location, and surface treatment (e.g., whether the surface is scraped during collection) [136, 137, 134]. Despite the simplicity of the concept, dew collection is fundamentally constrained by thermodynamic limits. A basic energy balance indicates that a surface radiating at 100 $\mathrm{W/m^2}$ over a 12-hour period can, at most, condense approximately 2 $\mathrm{L\,m^{-2}}$ of water. This ceiling arises from the high

latent heat of condensation (2200 J/g), which defines the energy cost of water phase change. In practice, additional losses, such as re-evaporation, imperfect water transport, and maintenance demands, further reduce achievable yields. As a result, dew harvesting remains a relatively low-output solution compared to other atmospheric water collection techniques.

To improve performance, various condenser geometries have been proposed with the goal of enhancing radiative loss and reducing convective heat gain. Among these, circular cone designs [131, 138] (Figure 1.25(center)) and V-shaped surfaces [132](Figure 1.25(right)) have demonstrated improved cooling efficiency by increasing the surface's effective sky view. In particular, the V-shaped geometry consists of a central cooling surface oriented vertically, flanked on both sides by mirrors inclined at 45°. These mirrors reflect the cold sky onto both faces of the surface, effectively doubling its radiative exposure. As a result, the surface loses heat more efficiently without requiring thermal insulation on the rear side.

Alternative approaches have also emerged that aim to bypass the energetic limitations of direct condensation. Sorption-based systems use hygroscopic materials to absorb water vapor from the air during the night, followed by desorption and condensation during the day when solar energy is available. This technique benefits from the higher energy flux of sunlight but introduces greater operational complexity. Such systems must be cyclically managed: opened to ambient air at night to absorb moisture, then sealed and heated during the day to recover the condensed water[6].

In parallel, active dew harvesting systems based on conventional refrigeration cycles have been adapted to maximize water recovery. Air conditioners inherently produce condensate as a byproduct, and industrial-scale atmospheric water generators have extended this principle to deliver yields ranging from 100 to over 10 000 L/day, depending on environmental conditions. However, these systems are highly energy-intensive, and the underlying energy requirement for phase change remains unchanged [6].

The scalability of passive dew collection remains limited by its low energy throughput. One of the largest field-scale implementations, deployed in India over an area of 850 m^2, yielded only 6500 liters of water across seven months [136]. This result highlights the ongoing technical and energetic barriers to large-scale adoption. While dew harvesting remains attractive for its simplicity, and independence from external infrastructure, its practical role is still challenging.

1.10 Conclusion

As we have exposed in this section, fluids display a wide diversity of morphologies and behaviors even on perfectly smooth surfaces. Depending on the conditions, they may appear as static isolated droplets formed by condensation or as rivulets meandering down a window. Geometry adds an additional layer of complexity and plays a decisive role at multiple scales. At the macroscopic level, a liquid on a fiber does not behave like a liquid on a plate: curvature restricts spreading, modifies Laplace pressure, and generates morphologies, such as a barrel that simply cannot occur on flat substrates. At the microscopic level, surface features introduce further mechanisms. They enable extreme wetting states such as superhydrophilic or superhydrophobic regimes and may impose directional wetting through asymmetric textures.

With these concepts in hand, we can now revisit classical fluid systems that are usually studied on smooth substrates and examine how their behavior changes when substructures are introduced. In this thesis, we focus on one particular type of microstructure, grooves. Although simple, grooves can radically alter the usual morphologies and dynamics, reorganizing droplet growth and drainage in ways that cannot be predicted from smooth-surface theory alone. The following chapters investigate how these minimal structures reshape fluid behavior across a variety of situations

Chapter 1 examines how the grooves naturally formed within fiber bundles modify droplet motion, showing that they can accelerate sliding droplets by altering dissipation while simultaneously increasing coating losses along the descent.

Chapter 2 investigates condensation on a vertical grooved plate and demonstrates how groove spacing governs water retention through droplet growth, storage, and the emergence of large-scale drainage patterns.

Chapter 3 turns to the lower edge of the same plate, where groove-fed drainage transitions into dripping and where the geometry controls both the position and the frequency of suspended-droplet release.

Chapter 4 shows that a pair of grooves can hold a thin water film even under extremely low flow rates that would normally cause dripping on a smooth surface, and that this stabilized film eventually ruptures at the groove ends, releasing droplets in a regular and periodic manner.

2 Droplet on fibers

2.1 Motivation

In both natural and engineered systems, the ability to transport small volumes of water along thin fibers is crucial. Plants and animals in arid regions often rely on spines, hairs, or silks to capture and direct water from dew or fog [139, 140, 141, 12, 11]. Inspired by such strategies, synthetic devices have adopted vertical fibers as passive conduits for water drainage, from microfluidic threads [70, 89, 142, 91] to large-scale fog-harvesting harps [4, 122, 7]. In these systems, gravity drives droplets along the fibers, but the efficiency of transport depends strongly on the delicate interplay between geometry, surface wetting, and viscous dissipation [18].

Much of our current understanding comes from studies on smooth fibers. However, real-world surfaces, which are frequently textured, introduce additional complexity that has been previously neglected. When two or more fibers are slightly twisted together, narrow grooves naturally form along their junctions, which can trap or guide liquid differently than a smooth surface. How these substructures affect droplet speed, shape, and fiber coating remains an open question that we explore in this chapter.

2.2 Experimental setup

Tracking the motion of droplets sliding along vertical fibers presents a significant experimental challenge. On the one hand, the droplet decelerates as it loses liquid, making it challenging to keep it within the camera's field of view. On the other hand, if the camera is placed far enough to capture the whole trajectory, it loses resolution on the droplet itself, which may travel several meters.

To overcome these difficulties, we inverted the classical approach: rather than following a falling droplet, we move the fiber upwards at the same speed as the droplet descends. This creates the illusion of a stationary droplet while in reality

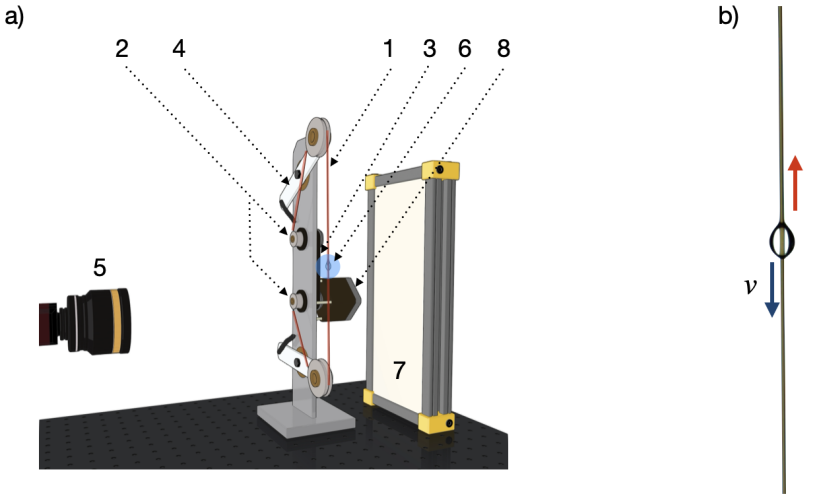

Figure 2.1: (a) Sketch of the experimental setup from two angles: (1) Motorized fiber highlighted in red, (2) Central pulleys, (3) Belt, (4) Pivoting spring-loaded arms, (5) Camera and lens, (6) Drop highlighted in blue, (7) Light panel , (8) Motor. (b) Typical frame taken by the setup.

the fiber slides through it. This method allows us to use a static camera while extending the effective tracking range to several meters.

To build a speed adaptive vertical fiber, we designed a motorized system based on a dual-pulley architecture, represented in Figure 2.1. Each end of the fiber (1) is attached to a pulley (2): one motorized and one passive. A belt (3) links both pulleys, ensuring synchronized rotation. At both extremities of the setup, the fiber passes through guide rollers mounted on pivoting arms. These arms are loaded with springs, allowing them to adjust position and maintain constant tension throughout the experiment (4). The fiber passes through these rollers, forming a tensioned vertical segment where droplets are deposited and analyzed. The total fiber length available on the lower pulley is approximately 3m. The CCD camera (5) records a fixed field of view ($\approx$ 2cm height), centered on the droplet (6). Back lighting from a uniform LED panel (7) provides high-contrast images. A Python program using a PID-inspired algorithm analyses live video to determine the droplet vertical position. This data feeds a control loop that adjusts the motor (8) speed, and thus the upward fiber speed, to maintain the droplet at the center of the image. As a result, the droplet appears stationary in the frame, even as it loses mass through film deposition. The same program also allows for synchronized image acquisition and metadata recording (time and fiber upward speed).

2.2.1 Material

We used nylon fiber with diameters ranging from $d = 80\mu$m to $d = 280\mu$m (brand Platil, type Strong). Then, we fabricated bundles from $n = 1$ to $n = 4$ fibers and tied them together by crimping a metallic ring at both ends. Larger n values have been tested, but the entire thread becomes so large that droplets lose their

sketch	n	d_e	n_g
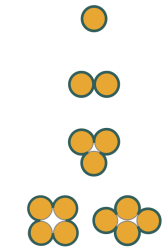	1	d	0
	2	$2d$	2
	3	$5d/2$	3
	4	$3d$	4

Table 2.1: Main characteristics of fiber bundles considered herein: effective diameter d_e (surligned in green in sketches) and groove number n_g as a function of the number of fibers n.

μ (mPa s)	ρ (kg m^{-3})	γ (mN m^{-1})
10	935	20.1
20	949	20.6
50	960	20.8

Table 2.2: Physical properties of the silicone oils used: kinematic viscosity (μ), density (ρ) and surface tension (γ) as described by the manufacturer (Dow).

axisymmetric shape [71, 81]. To guarantee fiber-to-fiber contact within the bundles, a slight torsion is applied, with a pitch length significantly larger than the setup size. This ensures that the torsion does not interfere with the behavior of the droplets. By varying the number n of fibers, we modify the substructure of the vertical threads, forming n_g grooves. Different configurations may form when n increases. In particular, for $n = 4$, two configurations can be formed, but they possess similar characteristics, as indicated in Table 2.1. The effective diameter d_e of the structure is considered by comparing the external perimeter of the grooved structure with an equivalent cylinder. The table 2.1 summaries the equivalent diameter d_e and groove number n_g for the structures studied herein.

We perform experiments with silicone oil (Dow Corning) to avoid partial wetting and evaporation that would occur with water. The oils had kinematic viscosities of 10, 20 and 50cSt. A table summarizing their physical properties is provided in Table 2.2.

2.2.2 Experimental protocol

Each experiment begins by depositing $3\mu L$ of silicone oil onto the fiber using a precision syringe. We carefully ensure the droplet forms a barrel-shaped morphology, fully wrapping around the fiber. Once the droplet is detected and stabilized at the center of the camera field, data acquisition is launched. We stop recording when the droplet either becomes too small to measure or exits the barrel regime. After each trial, the fiber is rewound in the opposite direction while being cleaned using a Kimtech technical wipe soaked in isopropanol. The system is then ready for the next experiment.

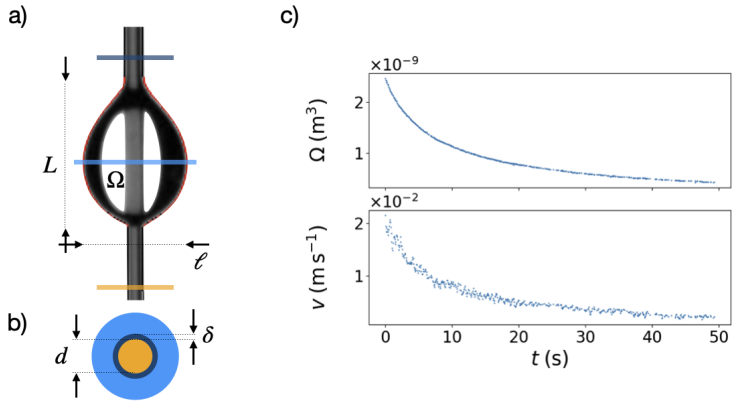

Figure 2.2: Image analysis and volume tracking of a droplet sliding along a vertical fiber of diameter d. (a) Binary image obtained after thresholding and contour detection, used to extract the droplet geometry (height L, width ℓ) and to estimate its volume Ω from Guldin's theorem. (b) Sketch of three horizontal cuts of the system: dry fibers in front of the droplet (yellow), the droplet cross section (light blue), and the liquid film of thickness δ after the passage of the droplet (dark blue). (c) Temporal evolution of droplet speed v and volume Ω. Both quantities decrease as the droplet descends, consistent with liquid loss into the deposited film.

2.2.3 Image analysis and volume estimation

Each recorded frame undergoes processing through a Python pipeline based on OpenCV. The steps include: Cropping to the region of interest (see Figure 2.2(a)), thresholding to produce a binary image, and contour detection to isolate the droplet from the fiber (red contour in Figure 2.2(a)). Assuming axisymmetry around the fiber, we estimate the droplet volume Ω using Guldin's theorem, also known as Pappus's centroid theorem [143]. The latter states

$$\Omega = 2\pi l_{cm} A, \tag{2.1}$$

where l_{cm} is the distance to the center of mass of half the droplet section and A its surface. We get these values from image processing. We correct the fluid volume by subtracting fiber volume in-closed by the droplet. In addition to the volume Ω, we extract the droplet geometry height L and width ℓ, represented in Figure 2.2(a).

As the droplet travels along the fiber, it leaves a thin film of thickness δ at droplet rear, sketched in Figure 2.2(b). This provokes a simultaneous decrease of both speed v and volume Ω over time, as represented in Figure 2.2(c).

2.3 Results

2.3.1 Droplet shape

When droplets of equal volume wrap around an increasing number of fibers, their morphology changes markedly, as illustrated in Figure 2.3. The droplet becomes more elongated as fibers are added to the bundle. To quantify this observation, Figure 2.4(a) reports the droplet width ℓ and height L for all experiments. Each

Figure 2.3: Experimental pictures of droplets of 3μl sliding down 1, 2 and 3 fibers of $d = 140\mu$m from left to right. A liquid film is seen behind the droplet.

color corresponds to a different number of fibers $n = \{1, 2, 3, 4\}$ and viscosity $\eta = \{10^{-2}, 2\ 10^{-2}, 5\ 10^{-2}\}$ Pa s. Because the droplet volume decreases during motion, both ℓ and L evolve accordingly. The data reveal a linear relation between the two lengths, with a slope close to unity, indicating that height and width change proportionally. The main difference lies in the offset: it increases with the number of fibers, reflecting the progressive elongation observed in Figure 2.3.

However, this comparison is not entirely fair. Increasing the number of fibers also increases the bundle's cross-sectional area, which alters the apparent droplet size [17]. To correct for this, we normalize both ℓ and L by the effective diameter d_e of the bundle. We compute it by matching the external perimeter of the grooved fiber bundle to that of an equivalent smooth cylinder. Once rescaled, all data collapse onto a single linear trend, Figure 2.4(b). This collapse shows that d_e is the relevant characteristic length governing droplet geometry, regardless of viscosity of fiber count. Interestingly, the number of grooves does not alter the overall shape once normalized. Finally, while droplets on fibers are often treated as nearly spherical objects [60, 17, 18], our results reveal larger aspect ratios, typically $L/\ell \approx 1.4$–1.8 in dynamical cases.

The red colored region in Figure 2.4(b) at small ℓ/d_e values is where droplets should leave their barrel shape to a clamshell shape. Indeed, we define the reduced volume Ω_c as the ratio between the droplet volume Ω and the volume of the fiber segment $\pi d_e^2 L/4$ enclosed by the droplet. Here, we approximate Ω as the volume of an ellipsoid with semi-axes $L/2$, $\ell/2$, and $\ell/2$, from which we subtract the volume of the embedded fiber. The criterion for keeping a barrel shape droplet is given by $\Omega_c > 1$ [60, 144]. Such as the barrel shape criterion becomes

$$\frac{\ell}{d_e} > \sqrt{3} \tag{2.2}$$

where all our data is seen. The lower limit $\ell = \sqrt{3} d_e$ is denoted by a red vertical line in Figure 2.4(b).

2.3.2 Film thickness

As droplets descend, their shape evolve: both L and ℓ shrink in time. This evolution is the consequence of a continual loss of liquid into the fiber coating. To understand this evolution, we now examine how much liquid the droplet deposits and how the thickness of this film depends on viscosity and fiber substructure.

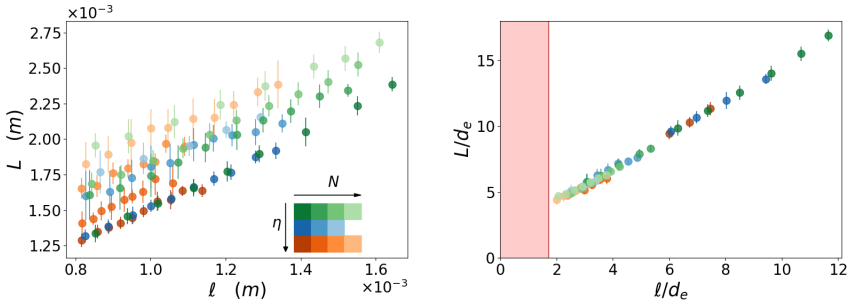

Figure 2.4: (a) Height of the droplet L as a function of the width ℓ of the droplet. All data points are colored as a function of viscosity η and fiber number n. See the color legend given as an inset. (b) Lengths are rescaled by the effective diameter d_e. The region colored in red corresponds to the $\Omega_c < 1$ criterion, such that a droplet there is no longer in a barrel configuration.

The volume Ω is decreasing as the droplet slides along the fiber, leaving a thin film behind. Liquid volume conservation states that

$$\dot{\Omega} = -\pi d_e \delta v. \tag{2.3}$$

where $\delta \ll d_e$ is the thickness of the liquid film left behind the droplet, as observed and sketched in dark blue in Figure 2.2(b). Whatever the η and n values, a nearly linear behavior is obtained in Figure 2.5(a) when $\dot{\Omega}$ is plotted as a function of speed v. All results are shown following the same color code as the inset of Figure 2.4. Different slopes are observed, depending on viscosity η and number n of fibers.

From the slopes measured in Figure 2.5(a), the relationship Equation(2.3) allows us to estimate the average film thickness $\bar{\delta}$ left behind droplets. Results are plotted in Figure 2.5(b) as a function of n. Typical values for $\bar{\delta}$ ranges from 10 to 50 μm. The film thickness is seen to be highly dependent on liquid viscosity η. It should also be remarked that the presence of grooves ($n > 1$) also has an important effect on the film thickness. Indeed, a clear increase of $\bar{\delta}$ is observed for all viscosities in Figure 2.5(b). In fact, liquid accumulate into the grooves. The above behaviors are emphasized in Figure 2.5(b) by colored lines which are guides for the eye.

Moreover, the Landau-Levich model (Section 1.5.2) of liquid coating is predicting a film thickness $\delta \propto \mathrm{Ca}^{2/3}$, and more precisely

$$\delta = 0.67 d_e \left(\frac{\eta v}{\gamma} \right)^{2/3} \tag{2.4}$$

as proposed in [62]. The volume loss vs speed should therefore scale as $\dot{\Omega} \propto -v^{5/3}$. However, the range of speed values (or Ca values) is less than a decade, such that a nearly linear behavior is observed in Figure 2.5(a) instead. Higher speeds cannot be reached with this experimental setup. Nevertheless, the liquid coating is highly sensitive to viscosity, and one expects that the film thickness increases as $\bar{\delta} \propto \eta^{2/3}$. For a single fiber ($n = 1$), the three measured thicknesses are in agreement with the Landau-Levich model since $\bar{\delta}/\eta^{2/3}$ gives a unique value of 2.5 10^{-4} m/(Pa s)$^{2/3}$ within error bars, see Figure 2.5(c). The cases with grooves ($n > 1$) are different since the penetration of the liquid into grooves relies heavily on viscosity, and here the Landau-Levich model ceases to provide accurate predictions.

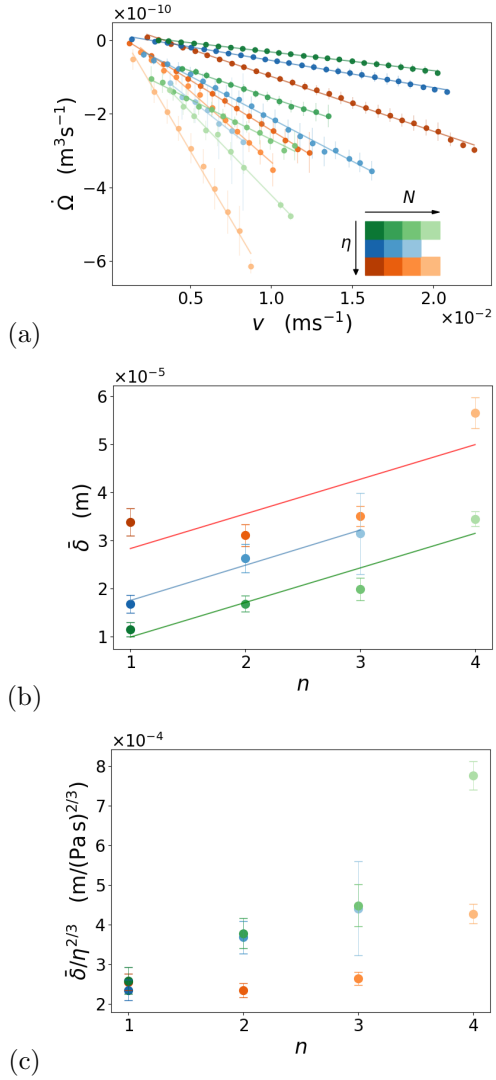

Figure 2.5: (a) Volume loss rate $\dot{\Omega}$ as a function of droplet speed v. Lines are linear fits used to extract the slopes for determining $\bar{\delta}$ from Equation(2.3). (b) Average Liquid film thickness $\bar{\delta}$ as a function of n. Lines are fitted on the data to emphasize η and n dependencies, but should be considered as guides for the eye. (c) Average film thickness normalized by $\eta^{2/3}$ emphasizing that the effect of viscosity is captured by the Landau-Levich model only for $n = 1$.

2.3.3 Droplet speed

The coating process discussed above continuously removes liquid from the droplet, reducing its volume and therefore the gravitational force available to pull it downward. To understand how this evolving balance of forces shapes the motion, we now examine the relationship between droplet speed and instantaneous volume.

In Figure 2.6(a), the speed v of the droplet is plotted as a function of the measured volume Ω. One may notice that the speed increases with the volume, a result which is consistent since the weight of the droplet is the driving force of the problem. A linear behavior is observed between the two physical quantities. Increasing the effective fiber diameter d_e reduces the speed, and more precisely the slope of the linear behavior. Also, different oil viscosities have been used in order to evidence the role of dissipation mechanisms. Increasing the viscosity has an effect on the speed, which is reduced accordingly. On top of that observation, one remarks that all linear trends are converging towards a particular volume at zero speed. It means that below that particular volume Ω_0, tiny droplets are static on the vertical fiber. This particular volume seems more dependent on fiber diameter than on viscosity, as we will see below.

2.4 Discussion

2.4.1 Droplet dynamics

The previous sections showed that droplet shape, coating thickness, and speed are tightly linked. Together, they describe what the droplet does as it moves. To understand why it behaves this way, we now examine the underlying force balance.

The motion of the droplet along a single fiber or the bundle of fibers is driven by gravity and surface tension as revealed by the following non-dimensional numbers. We can estimate the Bond number $\mathrm{Bo} = \rho g \Omega / 2\pi\gamma d_e$, which compares gravitational and capillary effects by taking the typical values of Ω in our experiments. We obtain Bo values around 0.75 for moving droplets, meaning that gravity drive the system, as well as capillary effects. The capillary number $\mathrm{Ca} = v\eta/\gamma$ compares surface tension effects to viscous ones. We have Ca values between 0.05 and 0.25, revealing that surface tension may overcome viscosity. The Weber number $\mathrm{We} = \rho v^2 d_e / 8\gamma$ is typically around 10^{-6} such that inertia can be neglected in the present study. This assumption has been considered in [18] where similar fiber sizes and drop volumes were considered.

In order to capture the linear behaviors of Figure 2.6(a), i.e. the droplet dynamics, we propose a model based on the sum of three forces acting on the droplet: gravity, dissipation and surface tension. The driving force is the weight of the droplet and is given by $F_g = \rho g \Omega$, where g is the gravitational acceleration.

Dissipation should play an important role, and following [18], we consider a classical drag force $F_d = -\xi \eta d_e v$, where ξ is a dissipation factor. Assuming that the friction force F_d is mainly due to velocity gradients within the droplet, and following [145, 18], one has

$$F_d = -\pi d_e \int_{a_f}^{L/2} c\,\frac{\eta v}{z}\,\frac{L}{\ell}\,dz + \pi d_e \int_{L/2}^{a_r} c\,\frac{\eta v}{z}\,\frac{L}{\ell}\,dz \tag{2.5}$$

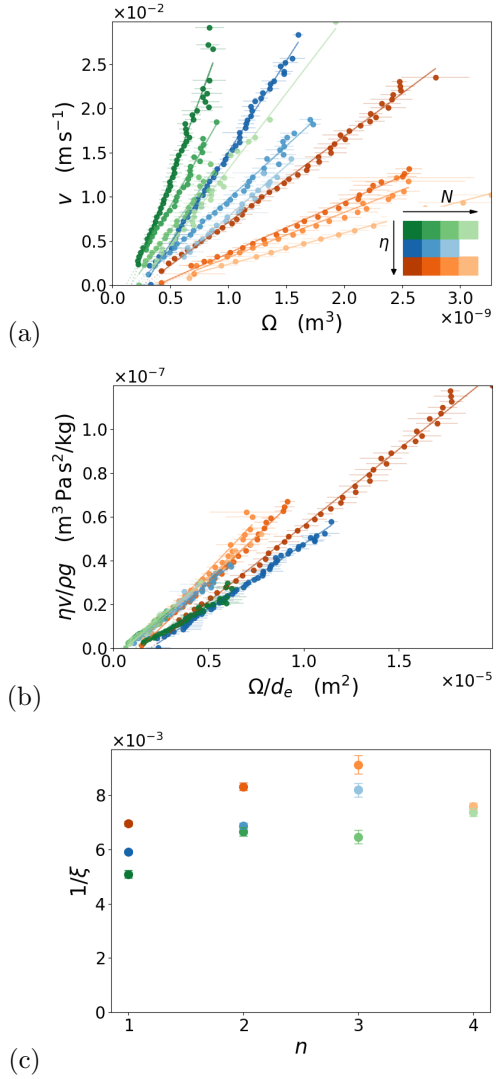

Figure 2.6: (a) Droplet speed as a function of Ω emphasizing the gravity driven mechanism. Each color is associated with viscosity η and fiber number n. Error bars are given. Data are fitted by a linear model of Equation(2.8). (b) Rescaled speed v and volume Ω according to Equation(2.8). (c) From the slopes extracted in the top graph, the inverse dissipation factor $1/\xi$ is estimated. It is plotted as a function of n with the same color code. One observes that the presence of grooves favors the droplet motion, i.e. $1/\xi$ increases with n.

where velocity gradients v/z are integrated from the shortest distance from the contact line at either the front a_f or the rear a_r of the droplet. We cut the droplet into equal parts $L/2$, although the lack of front/rear symmetry, because the sources of dissipation are mainly located at the front and at the rear of the droplet. The dimensionless constant c is a geometrical factor close to unity studied in [18]. After integration over the front of the droplet and the rear of the droplet, the main contributions to ξ are due to the front and rear characteristics, and more precisely

$$\xi = c\pi \frac{L}{\ell} \ln\left(\frac{L^2}{4a_f a_r}\right) \tag{2.6}$$

In front of the droplet, the fiber is dry such that a_f is estimated to $a_f \approx 10^{-9}$ m from de Gennes [146] while at the rear of the droplet, this distance is limited by the film thickness $a_r = \delta$. Injecting geometrical characteristics L/ℓ as measured herein and $\bar{\delta}$ around 10 μm, one obtains $\xi \approx 115$.

The capillary force is acting on both sides of the droplet. In the front, i.e. at the bottom of the droplet, the contact line separates a dry fiber and the droplet, such that the contribution to the capillary force is given by $\pi\gamma d_e$. Indeed, silicone oil is totally spreading on the fiber such that the contact angle can be considered as zero. Behind the droplet, capillary force comes from the liquid film. One has a contribution $-\pi(d_e + \delta)\gamma$. Summing both contributions gives a capillary force $F_c = -\pi\delta\gamma$.

Therefore, taking into account the sum of the forces acting on the droplet, the equation of motion becomes

$$\rho\Omega\dot{v} = \rho g\Omega - \pi\delta\gamma - \xi\eta d_e v. \tag{2.7}$$

Neglecting inertia, the speed of the droplet v is given by

$$v = \frac{\rho g\Omega}{\xi\eta d_e} - \frac{\pi\gamma\delta}{\xi\eta d_e}. \tag{2.8}$$

One finds the linear dependency of the speed on the droplet's volume with a single slope. Figure 2.6(b) plots $\eta v/\rho g$ as a function of Ω/d_e to evidence such linear behavior. Different slopes are, however, observed, indicating that the dissipation factor depends on η and n. This will be discussed in the next subsection.

Setting the speed to zero in Equation(2.8), one can find the volume offset Ω_0 being

$$\Omega_0 = \frac{\pi\delta\gamma}{\rho g}. \tag{2.9}$$

Injecting the values of surface tension and density in the last relationship, one finds a typical volume offset around 0.1 $\mu\ell$, in agreement with our measurements. The above condition can be interpreted in terms of Bond numbers. Indeed, Equation(2.9) can be rewritten into $\mathrm{Bo_c} = \bar{\delta}/2d_e \approx 0.05$, meaning that all droplets characterized by a larger Bond number are moving until they lose volume and reach this critical low $\mathrm{Bo_c}$ value.

2.4.2 Dissipation factor

By fitting the slopes of Figure 2.6(b) with Equation(2.8), the inverse dissipation factor $1/\xi$ can be extracted from all experiments. The results are shown in Figure

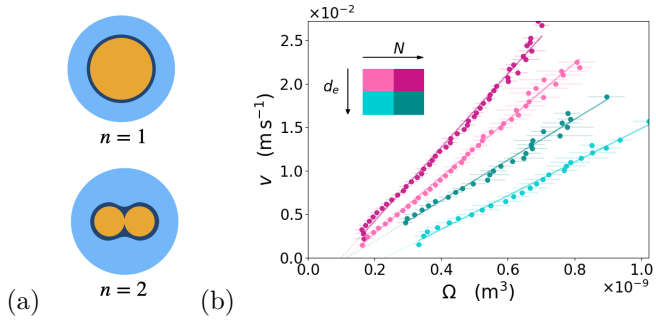

Figure 2.7: (a) Sketch of the additional experiment where a single fiber of diameter d is compared with $n = 2$ fibers of diameter $d/2$. The equivalent diameter d_e is therefore conserved, but grooves are present in the second case. (b) Droplet speed as a function of droplet volume for two situations is illustrated in (a). Extra speed is clearly obtained for $n = 2$.

2.6(c). One observes that the dissipation factor (and therefore droplet speed) is dependent on viscosity η and fiber number n. The values of $1/\xi$ are close to the one estimated in the previous subsection, i.e. $1/\xi \approx 1/115 = 8.7\ 10^{-3}$. Surprisingly, the inverse dissipation factor seems more important for intermediate n values, such that higher speeds are observed for fiber bundles. The effect is already present for $n = 2$ and $n = 3$. There, a significant speed increase of about 20% is obtained from the single fiber case.

In Figure 2.6(c), one observes that ξ decreases with η and is quite sensitive to the substructure, i.e. depends on n. Indeed, Equation(2.6) links ξ to δ. Since high viscosities imply thicker films behind the droplet, one expects less dissipation. A second observation is that substructure has a significant effect on dissipation since ξ is lower for $n = 2$ and $n = 3$ than for $n = 1$. Of course, the previous argument on film thickness could also be used. Grooves allow for faster droplet motion due to the thicker films behind. It is hard to separate effects, but it should be noted that the groove effect is significant with 20% extra speeds for some configurations.

To assess the effect of grooves, we performed additional experiments. In Figure 2.7, droplet dynamics are shown for comparing the case of a single fiber of diameter d with two adjacent fibers of diameter $d/2$, thus fixing the equivalent diameter $d_e = d$. Two different diameters d are tested. In both cases, the droplet speed v is much higher when $n = 2$ than for $n = 1$. These additional experiments confirm extra speed for two joined fibers equivalent to a single one, as represented in Figure 2.8. This image shows that two drops of equal volume travel at different speeds depending on the geometry of the substrate: the grooved substrate allows faster movement over the same time interval.

A last remark is that the dynamics emphasized above lead to a more complex phenomenon over longer times. Indeed, any droplet is losing volume and finally stops when reaching Ω_0. After a while, the coating left above the immobile mother droplet forms smaller daughter droplets due to the classical Rayleigh-Plateau instability. Those daughter droplets are on a prewetted fiber such that they start moving as soon as they grow. Finally, they reach the mother droplet. Fed by daughter droplets, the mother droplet starts again its motion till reaching again Ω_0. A start and stop motion of the primary droplet develops, as studied by Van

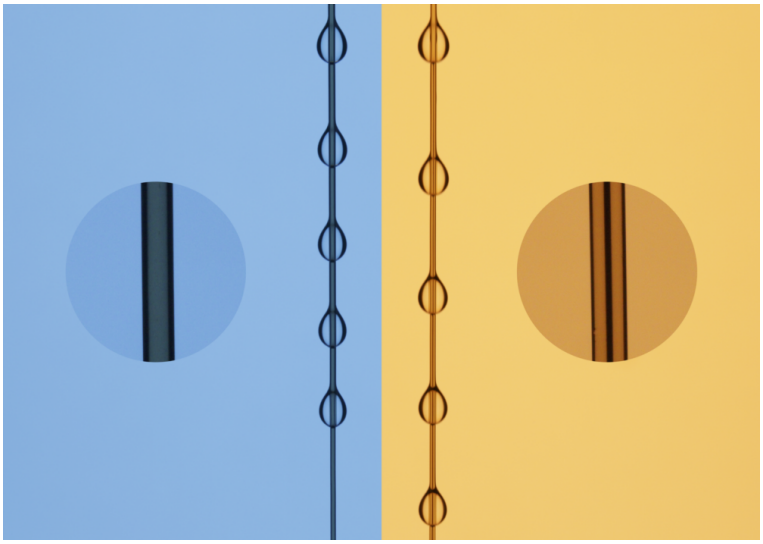

Figure 2.8: Superposition of droplet position over equal time intervals on two substrates with identical equivalent diameter d_e but different fiber configurations. (Left) A silicone oil droplet slides along a single fiber of diameter d. (Right) A second droplet of same initial volume descends a double-fiber bundle ($n = 2$) composed of fibers of diameter $d/2$. Although both configurations have the same outer perimeter, the grooved geometry formed by the fiber pair leads to a visibly faster descent. This highlights the influence of substructure on droplet mobility.

Hulle [147] and represented in Figure 2.9.

2.5 From barrel to clamshell

What changes if we consider not a barrel situation but rather a clamshell one? This matters because clamshell morphologies appear when the droplet is relatively small compared to the fiber diameter, or when using high surface tension liquids like water or glycerol, as explained in Section 1.5. Such asymmetrical shapes fundamentally alter the way a droplet interacts with the fiber, especially when substructures such as grooves or twists are introduced. J. Van Hulle explored this regime using vertical bundles of twisted fibers, and found several notable insights about droplet motion [86].

Twisting a pair of fibers creates a regular substructure: a helical groove whose pitch decreases as the number of twists increases. This groove acts as a guide path for the droplet, biasing its motion along the helical trajectory. The degree of twist is quantified by the dimensionless parameter $\alpha = L/\pi b$, which compares the droplet length L to the half-pitch πb of the helix. In this framework, $\alpha = 0$ corresponds to untwisted, parallel fibers, while increasing values of α represent more tightly twisted configurations, with $\alpha > 1$ indicating that the droplet spans multiple grooves.

At low twist numbers, as illustrated in Figure 2.10, the helical pitch remains large compared to the droplet length. In this regime ($\alpha < 1$), the droplet fits entirely within a single helical turn and closely follows the groove. The motion is predominantly rotational, with the number of turns made by the droplet scaling

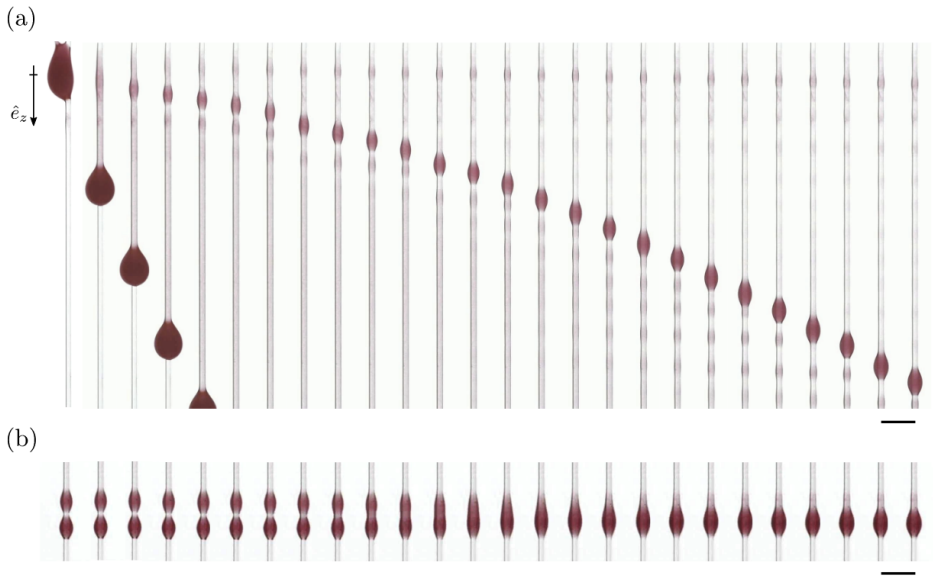

Figure 2.9: From J. Van Hulle's work [147]. (a) Red-dyed silicone oil droplet descending a vertical nylon fiber. The time interval between each frame is $0.68\,\mathrm{s}$. As the droplet slides downward, it leaves behind a liquid film. The film is thicker when the droplet speed is higher; thus, at the release point of the initial droplet, referred to as the mother or generation 0 droplet, the film is at its thickest. This triggers the Rayleigh–Plateau instability, leading to the formation of a small new droplet, termed the daughter or generation 1 droplet, which then slides along the film left by the mother. (b) Same experiment viewed further down the fiber. The mother droplet is located below, while the daughter droplet follows above. The time interval between each frame is $0.017\,\mathrm{s}$. One observes that the daughter droplet eventually catches up with the mother, resulting in coalescence. Experimental conditions for both sequences: droplet volume $\Omega = 5\,\mu\mathrm{L}$, kinematic viscosity $\nu = 100\,\mathrm{cSt}$, and fiber diameter $d = 0.3\,\mathrm{mm}$. Scale bars represent $2\,\mathrm{mm}$.

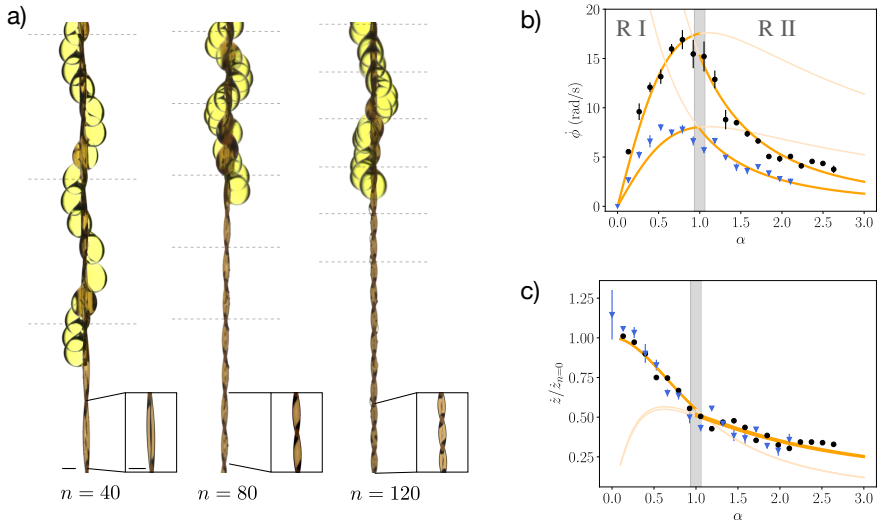

Figure 2.10: From J. Van Hulle's work [86] (a) Superposition of successive pictures ($\Delta t = 0.2$ s, scale bars correspond to 1 mm) of an asymmetrically shaped droplet travelling down twisted fibers with a helical motion. From left to right, the number of fiber twists increases, $n = 40,\ 80,\ 120$. The dashed horizontal lines represent the fiber pitch. For small n, the droplet follows exactly the substructure, displaying a helical motion, see ($n = 40$). However, at a larger number of twist values, the droplet exhibits reduced adherence to the tight substructure, resulting in an additional vertical motion, see ($n = 80$) and ($n = 120$). The motion is a mix of translations and rotations, but the helical motion is no longer correlated with the helical groove of the twisted fibers. (b) Angular speed $\dot{\phi}$ as a function of α. In regime I, $\alpha < 1$, the angular speed increases with α. In regime II, $\alpha > 1$, it is slightly decreasing. The colored curves are fits of the respective regimes. (c) Non-dimensionalized linear speed $\dot{z}/\dot{z}_{n=0}$ as a function of α. In regime I, $\alpha < 1$, the non-dimensional linear speed decreases with α. In regime II, $\alpha > 1$, it decreases more gently. The colored curves are fits of the respective regimes. Data with black circles (●) are for a low viscosity, and data with blue triangles (▼) are for a higher viscosity. The gray region in both (b) and (c) depicts the transition between the two regimes.

linearly with the imposed twist. As shown in Figure 2.10, the angular speed $\dot{\phi}$ increases with increasing twist, while the vertical speed $\dot{z}$ decreases, indicating that tighter grooves favor rotation but hinder downward motion.

As the twist increases further, the pitch shortens until the droplet spans multiple grooves simultaneously ($\alpha > 1$). In this high-twist regime, the groove no longer fully constrains the droplet. The trajectory becomes intermittent: the droplet alternates between following the helical path and slipping vertically, resulting in a mixed "skipping" motion. As a result of this change in dynamics, the angular speed $\dot{\phi}$ begins to decrease with increasing twist, while the vertical speed $\dot{z}$ continues to decrease, but more slowly, the skipping introduces brief episodes of enhanced vertical motion.

This geometric transition defines a clear boundary between two qualitatively distinct regimes of motion. It once again underscores the role of grooves as key elements in directing droplet transport.

2.6 Future works

These findings have useful implications for water harvesting technologies, where the speed of droplets traveling along fibers directly influences collection efficiency. Vertical fiber-based structures, often referred to as harps, can drain water rapidly after an initial onset period, the time required for the first captured droplets to reach the reservoir [148, 149]. Shortening this onset time is particularly important under fluctuating weather conditions. Our results suggest that fiber bundles, through the grooves formed at their junctions, could accelerate this initial drainage by promoting liquid transport inside the substructure (see Section 1.3.2).

Beyond harvesting applications, the experimental approach developed here provides access to detailed measurements of dissipation within moving droplets. This capability effectively turns the setup into a simple rheometric tool, which could be used to probe non-Newtonian or complex fluids in future work.

Finally, the presence of substructures invites a re-examination of classical problems. We have already shown that grooves increase the amount of liquid deposited behind a droplet compared with a single smooth fiber, modifying the Landau–Levich–Derjaguin coating (see Section 1.5.2). The same mechanisms may affect the Plateau-Rayleigh instability, since grooved fibers can redistribute fluid along their length and potentially alter the selected instability wavelength (also in Section 1.5.2).

2.7 Summary

In this chapter, we built an experimental setup able to measure simultaneously droplet speed v and volume Ω during their motion on various threads. We capture the dynamics of the droplet motion, and we proposed models based on the three main forces at work : weight, dissipation and surface tension. Such measurements allow for estimating the dissipation factor ξ, which is dependent on viscosity because of the film thickness left behind.

On top of that, we evidenced that the droplet motion is deeply affected by the substructure of the vertical thread. Indeed, grooves are collecting more liquid such

that the film thickness left behind the droplet depends on the groove number. As a result, dissipation is reduced, and droplets on grooved threads travel up to 20% faster than on smooth fibers.

This chapter demonstrates in a minimal system that geometric features can influence fluid transport and coating on a fiber. The next chapter extends this idea to planar substrates under condensation, where similar geometric constraints reshape droplet growth, retention, and drainage across an entire surface.

3 Condensation

3.1 Motivation

Condensation is a ubiquitous phenomenon that plays a crucial role in both natural and engineered systems, from cloud formation [125] to the operation of heat exchangers [5] and atmospheric water harvesters [137]. In particular, passive dew harvesting, where water condenses from ambient air onto a radiatively cooled surface, promise a low-tech, energy-free solution to water scarcity. Yet a major limitation persists: a significant fraction of the condensed water remains trapped on the collecting surface [136]. This retained water not only limits the amount of liquid that can be harvested overnight but may also evaporate during the day, further reducing the net yield. Efficient drainage of condensed water is therefore essential to maximize collection performance.

The previous chapter showed that even the simplest geometric substructures, such as grooves inside fiber bundles, can influence droplet motion. Moreover, we looked at a single droplet at the time. Condensation, in contrast, produces a dense and continuously renewing population of droplets across a two-dimensional surface. This raises a broader question central to the thesis: how does surface geometry influence water retention and drainage when droplets form collectively and interact across the whole substrate?

To enhance drainage, many designs draw inspiration from nature and introduce micro- or millimetric surface textures, such as grooves [10] or ridges [150], which can guide and evacuate liquid effectively. Among these, vertical grooves are widely adopted [22, 9] for their simplicity and compatibility with large-scale fabrication. Yet their actual role during steady-state condensation remains poorly understood. How much water is retained on the surface? Where exactly is it trapped? How do these effects depend on groove spacing or geometry? Whether grooves facilitate drainage or promote retention likely depends on subtle interactions between geometry, wetting, and condensation dynamics, but a clear framework to disentangle

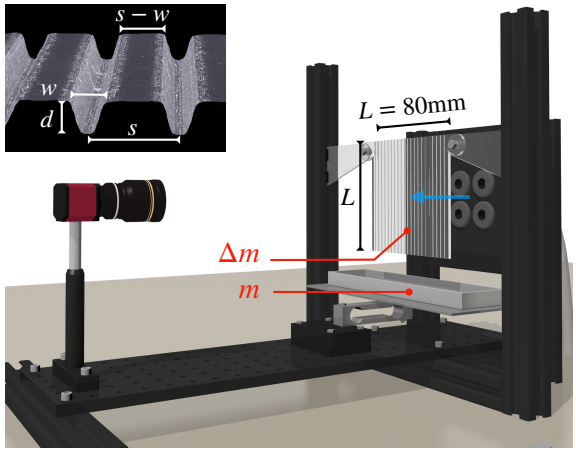

Figure 3.1: Experimental setup. Warm, humid air is generated by bubbling compressed air through a heated water reservoir and directed toward the vertically mounted substrate via four nozzles (right). Condensation forms on a square acrylic plate of side length $L = 80\,\mathrm{mm}$, either smooth ($s = 80.00\,\mathrm{mm}$) or patterned with parallel vertical grooves. The grooves have depth d and width w both equal to $0.20 \pm 0.01\,\mathrm{mm}$, while the spacing s between grooves ranges from 0.30 to $10.00\,\mathrm{mm}$. The flat region between two adjacent grooves is referred to as a plateau, with a width equal to $s - w$. Water detaching from the substrate is collected in a vessel connected to a strain gauge, providing the time-dependent collected mass $m(t)$. The retained mass $\Delta m(t)$, representing the water still present on the substrate, is obtained from $m(t)$ as described later in the text. The inset shows the groove cross-section, where the groove geometry parameters d, w, and s are indicated.

these factors is still missing.

This chapter addresses that ambiguity by focusing on a single geometric parameter: the spacing between grooves. Using an innovative and high-throughput condensation setup, we systematically vary groove spacing while keeping the groove geometry constant. This approach reveals that not only the behavior inside the grooves matters, but also the dynamics occurring on the plateaus, in between two grooves. Below a critical spacing, a new condensation regime emerges, where droplet growth becomes strictly confined by groove spacing. This geometrically constrained regime alters drainage mechanisms and reshapes water retention behavior, offering fresh insight into how a simple geometric feature governs the efficiency of condensation systems.

3.2 Experimental setup

3.2.1 New approach of condensation

The classical approach to forced condensation involves cooling a surface below the dew point, typically by placing it in contact with a thermal exchanger. Much like the condensation that forms on a cold water bottle taken out of the fridge, droplets nucleate and grow on the chilled substrate. This method is widely used due to its reliability and steady-state precision, and remains the standard in many laboratory setups. However, its main drawback lies in its slowness: condensation rates typically stay below $10\,\mathrm{g/m^2h}$ [96, 22, 100], making experiments lengthy. As

a result, exploring multiple surface geometries or observing rare events becomes a time-intensive process.

Just as breathing on a cold window instantly covers its surface with tiny droplets, condensation rapidly form when directing a warm, humid airflow onto a cooler substrate. This method, that we call *moist breath*, offers a faster alternative to classical cold-contact cooling. In our setup, shown in Figure 3.1, compressed air is bubbled through heated water, producing saturated vapor that flows onto a room-temperature acrylic plate. This moist breath generates condensation rates up to $900\,\mathrm{g/m^2\,h}$, over 150 times faster than traditional methods, making it ideal for exploring how surface microstructures, such as grooves, influence water retention and drainage dynamics.

3.2.2 Description

The generation of saturated vapor begins with compressed air, regulated in pressure and flow rate to ensure stability. This dry air is injected into a sealed water reservoir kept at a constant temperature of $T = 75 \pm 2°\mathrm{C}$. To enhance moisture uptake, the air is bubbled through the liquid using a custom-built diffuser: a coiled polyethylene tube perforated with evenly spaced holes and resting at the base of the water tank. Four outlet tubes pierce the reservoir lid and transport the humid air toward the experiment. No active pumping is needed as the incoming pressurized air pushes forward the moist air.

A key challenge with moist air transport is to prevent premature condensation inside the tubing. When hot vapor contacts cooler tube walls, droplets can form and, if dislodged, be projected onto the experimental sample, biasing the measure. To counter this, we place the water tank below the substrate being studied. This way, any condensate inside the tubing naturally drains back into the reservoir by gravity, thereby reducing the risk of contamination.

The vapor is delivered through four nozzles arranged in a square, positioned directly in front of the sample. This configuration produces a gentle and spatially homogeneous flow, with an air velocity around $1\,\mathrm{m/s}$, comparable to natural dew formation environments [137, 151]. As the flow cools upon mixing with ambient air, homogeneous nucleation produces a mist of fine droplets. The majority are carried away without depositing on the surface, and the few that do reach it are small, well below the groove dimensions, so they do not affect the measurements.

The system produces a significant vapor output, up to $0.5\,\mathrm{L/h}$, which could damage nearby electronics, particularly the sensitive strain gauge. To mitigate this, all experiments are conducted inside the climatic chamber ($3 \times 4 \times 2.5\,\mathrm{m}$), which maintains stable environmental conditions while absorbing excess humidity.

A comparative summary of both condensation techniques is presented in Table 3.1. While the cold-plate method offers precise thermal control and high-resolution imaging, its slow dynamics limit throughput and prevent the observation of rapid or collective phenomena. In contrast, the blown moist-air system enables fast condensation, rapid cycling, and high repeatability across a wide range of surface geometries. Its ability to reach steady state within minutes, combined with real-time imaging and mass tracking, makes it ideally suited for probing dynamic processes. As such, it serves as a versatile exploratory platform before potentially transferring select conditions to slower, high-resolution setups.

	Cold Plate	Moist Breath
Condensation rate	5–10 $g/m^2\,h$	900 $g/m^2\,h$
Time to steady state	30–60 min	1–2 min
Homogeneity	Excellent	Good
Sample properties	Heat conductor	Transparent
Visualization	Front view	Through sample
Environment	Glove box	Room with strong RH control

Table 3.1: Comparison between cold-plate and moist breath method. We use the latter technic in this study.

3.2.3 Material and methods

The substrate reaches a temperature of $T = 45.0 \pm 1.5°C$ within about 100 seconds. At this temperature, liquid water has a density $\rho = 992\,kg/m^3$ and surface tension $\sigma = 69\ 10^{-3}\,N/m$ [152], corresponding to a capillary length of $\lambda = \sqrt{\sigma/\rho g} = 2.67\,mm$.

The substrate is a square acrylic plate (TroGlass Clear) with thickness 3 mm and side length $L = 80\,mm$. Its wetting properties are characterized by a static advancing contact angle $\theta_A = 78.0 \pm 4.5°$ and a receding angle $\theta_R = 48.0 \pm 4.7°$, yielding an average contact angle of $\theta = 63 \pm 4.6°$. Surface structuring is done with a laser cutter (Speedy 100, Trotec), producing grooves with spacing s ranging from 0.30 to 10.00 mm, with depth d and width w such as $d = w = 0.2 \pm 0.01\,mm$. A smooth surface ($s = 80.00\,mm$) serves as the reference. Groove depth d and width w are both measured using optical microscopy (Keyence VHX), see inset of Figure 3.1. In the following, we refer to the flat region between adjacent grooves, of width equal to $s - w$, as plateau. Each experiment lasts 50 minutes and is repeated three times to ensure reproducibility.

Mass measurements are performed using a strain gauge placed directly beneath the substrate to monitor the amount of collected water. This setup provides real-time access to the mass $m(t)$ of drained water with a resolution of 0.05 g, roughly the weight of a single drop. Imaging is performed from behind the transparent substrate using a CCD camera at one frame per second. To enhance contrast and edge detection, a ring light is placed behind the four nozzles, producing circular highlights around each droplet facilitating droplet detection.

3.3 Transport description

3.3.1 Gravitational shedding

On a smooth vertical surface, condensation typically initiates at material imperfections, which act as preferential nucleation sites [97]. Because the process starts uniformly and nearly simultaneously across the entire substrate, droplet nucleation and early growth are highly synchronized [22], a behavior also observed during natural dew formation and in engineered systems such as heat exchangers. Droplets grow initially by vapor adsorption and subsequently through coalescence with neighboring droplets. Once a droplet reaches critical radius R_c, its weight overcomes surface retention forces and it begins to slide downward [44, 153]. As it

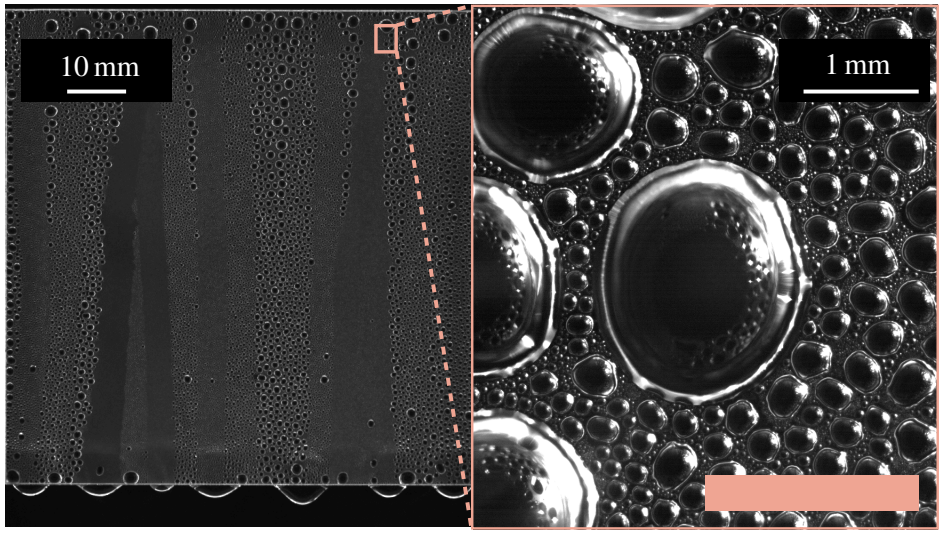

Figure 3.2: (Left) Overview of the smooth substrate, showing horizontal bands of similarly sized droplets. The droplet size varies from one band to another, reflecting the time elapsed since the last passage of a sweep droplet. These bands act as a short-term memory of the system: each is the trail left by a droplet sliding and sweeping smaller droplets from its path, with a characteristic trail width $2R_t$. The bands are not perfectly straight, as the sweep droplet's trajectory can be deflected by coalescence with droplets encountered along the way. Larger droplets are found in the upper part of the sample, where they have more time to grow before being intercepted by others, making the upper region the primary origin of sweep droplets. Once formed, these droplets traverse the entire surface, providing efficient drainage exclusively through gravitational shedding. (Right) Close-up view, showing droplets of various sizes. Growth is unconstrained by substrate geometry, leading to a broad size distribution prior to detachment.

descends, the droplet collects smaller droplets in its path [154], rapidly increasing its volume. Over time, its size stabilizes, through the emission of satellite droplets due to Plateau-Rayleigh instabilities [29, 30]. This process leaves behind a narrow, nearly dry trail of width $2R_t \approx 2\lambda$, where λ is the capillary length. The dry wake provides a clean region where new nucleation events can occur, effectively resetting the local condensation cycle. Occasionally, some of the satellite droplets released during descent are already close to the detachment radius and quickly begin to slide in turn. This creates a repeating cycle, adsorption, coalescence, sliding, and instability that governs condensation dynamics over time. Because droplets near the top of the surface experience less frequent sweeping, they have more time to grow and are more likely to initiate a shedding event. As a result, drainage is managed progressively, droplet by droplet, from the top part of the surface.

The fact that a sweep droplet collects all droplets in its path leads to an interesting property of the system. Once a region is scraped clean, it begins a new cycle of nucleation and growth, just like at the start of the experiment. Until it is scraped again, the droplets in that region grow at similar rates, resulting in a population of droplets with fairly uniform size. Moreover, in a steady state, the formation of sweep droplets at the top of the sample is independent from one drop to another. As a result, the system exhibits vertical bands of droplets whose sizes vary from one band to another, depending on the time elapsed since the last sweep droplet passage, as clearly visible on Figure 3.2 (Left). The striped pattern that forms across the sample thus represents the drainage memory of the system, a short-term memory, as each new band partially erases the previous one.

Finally, it is worth noting that droplets do not follow straight paths. Instead, their trajectories are influenced by interactions with the droplets they collect. During coalescence events, the fluid within the droplet reorganizes, which can alter its course. This effect is visible in Figure 3.2(Left), where two trails that start very close to each other gradually diverge as they descend. This behavior, combined with the striped surface pattern, allows sweep droplets to deviate from a vertical trajectory and collect bands they would have only partially swept otherwise.

3.3.2 Groove drainage

We now examine the grooved substrate with spacing $s = 0.5\,\text{mm}$ and geometry $d = w = 0.2\,\text{mm}$. Initially, nucleation resembles that on a smooth substrate. However, a novel behavior emerges: droplet growth becomes strictly confined by the plateau width, as visible in Figure 3.3(right). This geometric constraint prevents droplets from reaching the detachment radius, effectively suppressing classical gravitational shedding, an even extreme situation than that described by Bintein *et al* [22], where droplets over spanning multiple grooves are always visible. A central question follows: how is water evacuated in this regime? Three physical mechanisms govern drainage under such confinement: the wetting interaction between a droplet and a groove, the drying process, and long-range coalescence (LRC).

When a droplet interacts with a rectangular groove, its morphology depends on the contact angle θ and the aspect ratio d/w. According to Seemann *et al.* [40, 41], three regimes arise. For small aspect ratios and large θ, the droplet remains compact, spreading little into the groove (D regime). For moderate aspect ratios, the liquid fills the groove and forms a filament with positive Laplace pressure, the

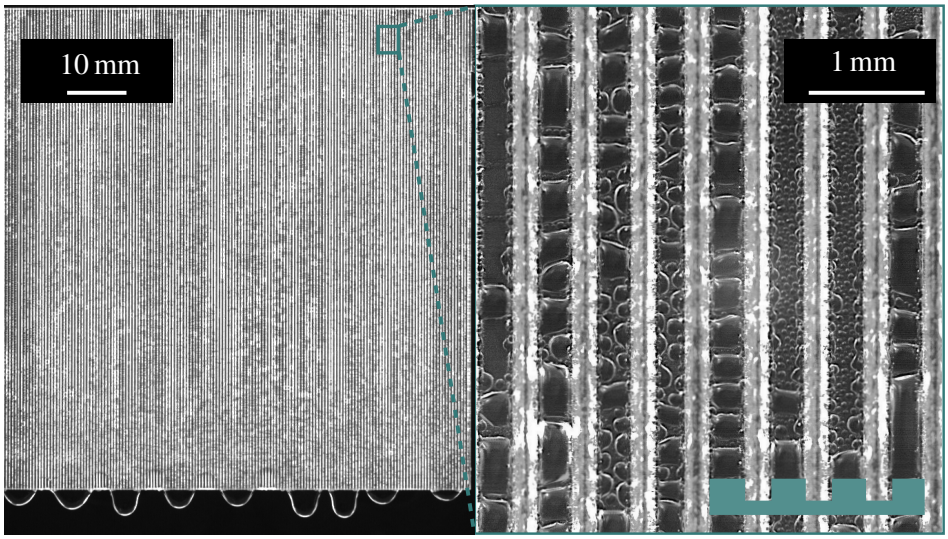

Figure 3.3: (Left) Global view of the grooved substrate ($s = 0.5\,\mathrm{mm}$, $d/w = 1$). In contrast to the smooth substrate, no large droplets are visible and no dry trails are present, indicating the suppression of gravitational shedding and the absence of drainage memory. Droplet size is limited by the plateau width, and transport occurs predominantly through groove-mediated drainage. (Right) Close-up view showing plateau and groove regions, as indicated by the schematic. Plateau droplets are laterally confined by the plateau width, causing larger droplets to elongate along the groove direction.

F^+ regime. This configuration is metastable for large volumes ($\Omega \gg w^3$), where it tends to revert to a droplet state. At high aspect ratios and low contact angles, the filament becomes fully confined with a concave meniscus and negative pressure, the F^- regime. The transition to this stable groove-filling state is predicted by the following equation, linking the aspect ratio d/w to the contact angle θ

$$d/w = \frac{1 - \cos\theta}{2\cos\theta}. \tag{3.1}$$

In the F^- regime, the groove acts as a one-dimensional capillary sink, drawing water from the adjacent plateaus.

This process is fundamental to the drying phenomenon. It was first described by Narhe and Beysens [155] during experiments on horizontal substrates with large-aspect-ratio rectangular grooves. As condensation continues, the water level within the groove rises until it contacts a droplet sitting on nearby plateaus. This initiates a rapid sequence of coalescence events: the initial merging between the plateau and the groove droplet raises the channel level, prompting further coalescence with neighboring droplets. In a short time (20ms for a 1cm long groove in the original experiment), all droplets on the top surface of one or both grooves merge into the channel, leaving it dry. This process is driven entirely by surface tension, as droplets stay smaller than the capillary length λ. Once dry, the surface is immediately ready for new nucleation.

A final mechanism, Long-Range Coalescence (LRC), enables fluid transfer between distant droplets connected by filled grooves. First reported by Bintein [22], LRC occurs over centimeter-scale distances through wet grooves. Liquid flows from one droplet to another, driven by differences in Laplace or hydrostatic pressure.

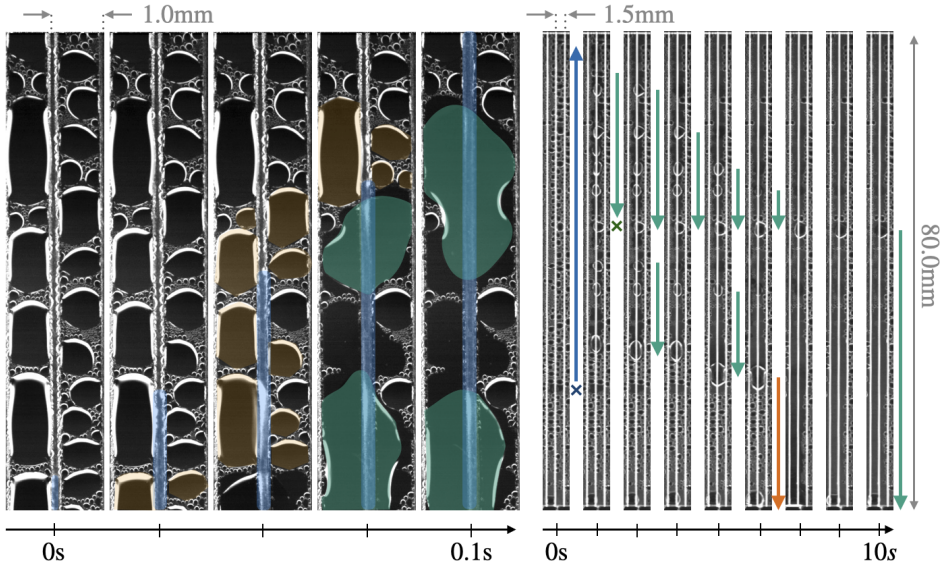

Figure 3.4: Drying dynamics and groove-mediated drainage. (Left) High-speed sequence on a substrate with $s = 1.0\,\mathrm{mm}$ ($d = w = 0.2\,\mathrm{mm}$) showing a capillary filament advancing upward inside a groove (blue), sequentially absorbing neighboring plateau droplets (yellow) and forming larger groove straddling droplet (green). The process, independent of gravity, spreads at $\sim 100\,\mathrm{mm/s}$ and can leave over spanning droplets behind when coalescence exceeds groove capacity. (Right) Large-scale view of a drying event on $s = 1.5\,\mathrm{mm}$ spacing. The event initiates at the blue cross and propagates upward, redistributing water into the groove before sequential drainage begins (green arrows). Droplets are pumped in order of hydrostatic pressure, sometimes growing before being absorbed, illustrating hierarchical long-range coalescence. Near the origin, excess influx creates a large droplet that eventually sheds (orange arrow), highlighting the balance between groove drainage and gravitational shedding. Together, these dynamics show how drying funnels plateau water into grooves, with outcomes ranging from full absorption to overflow-induced droplet release.

This mechanism allows the accelerated growth of droplets, thus enabling earlier shedding. Water transport by gravity in a vertically open groove, despite being the backbone of this mechanism, is not described theoretically yet.

To illustrate these concepts, we present in Figure 3.4 (left) a drying event observed during our experiments on a substrate with spacing $s = 1.0\,\mathrm{mm}$ and groove geometry $d = w = 0.2\,\mathrm{mm}$. This configuration corresponds to an F^- regime, as Equation (3.1) gives a critical aspect ratio $d/w = 0.6 < 1$ for a contact angle $\theta = 63°$. The sequence shows the time evolution ($\Delta t = 0.02\,\mathrm{s}$) of a defined region comprising a groove in the middle and two plateaus along. The advancing filament tip is highlighted in blue to aid visualization. Initially, we see droplets sitting on both sides of the grooves. Then, as the filament goes upward (confirming that gravity plays no role in this phenomenon), droplets, highlighted in yellow, merge sequentially with the filament. This results in fast expansion of the filament at a rate of 100mm/s, as fast as initial speed in capillary wetting (see Section 1.3.2), but sustained over the entire groove length. The drying process can be partial as not all droplets sitting on plateaus were absorbed. Interestingly, we observe the formation of large over spanning droplets resulting from the coalescence of plateau droplets, highlighted in green in Figure 3.4(left).

To dig further into the implications of these straddling droplets during the

drying process, we now look at what happens on the entire length of a groove on textured substrate ($s = 1.5$mm and $d = w = 0.2$mm). This is represented in Figure 3.4 (right), where we pictured a groove at fixed time intervals ($\Delta t = 1.1s$). On the first frame, highlighted with a blue cross is the location where the drying process begins. Then, in the following picture, the influx propagated until the upper part of the sample, creating multiple droplets that span over the central groove. As explained earlier, this process is the result of a quick reorganization of water distribution, from plateaus to the groove, and there is no drainage yet. In the following pictures, marked with green arrows, we see gravitational drainage of the water through the groove. This drainage is sequential; higher droplets are pumped first, illustrating a specific case of long-range coalescence. Interestingly, we observe that the droplet at the mid-height of the sample, marked by a green arrow, appears to grow during the first 7 seconds and then shrinks, being pumped by the groove. This phenomenon emphasizes the fact that there can be multiple hierarchies of pumping between the droplets, depending on Laplace and hydrostatic pressure, as mentioned earlier, as well as defect pinning or incomplete groove wetting, which likely alter the way fluid can circulate through the groove.

Another interesting phenomenon is observed near the origin of the drying event, marked by a blue cross, where a large droplet undergoes a distinct two-stage evolution. In the first four frames, the droplet grows steadily, fed through the groove by droplets located higher up. Then, in the fifth frame, it begins to slide down the surface, as visualized by an orange arrow. When the groove cannot drain the water fast enough, it leads to the formation of a droplet that may be large enough to shed. This highlights the interplay between groove-mediated drainage and gravitational shedding.

In summary, the interplay between coalescence, drying, and long-range coalescence gives rise to distinct water transport modes that depend strongly on substrate topography. On smooth substrates, drainage occurs exclusively via shedding: coalescence produces droplets large enough to overcome contact line pinning and slide under gravity, sweeping smaller neighbors along their path. In contrast, grooved substrates promote capillary confinement, shifting the dominant transport mechanism to groove drainage. Here, drying events funnel water from the plateaus into the grooves, where it flows downward under gravity. When this drainage is efficient, water remains fully confined, leaving no droplets visible on the surface. However, if the local influx exceeds the groove capacity, overflow occurs. This can lead to short-lived straddling droplets (static overflow) or to larger droplets that shed under gravity (shedding overflow). Intermediate cases also emerge, where droplets begin to slide but are eventually reabsorbed by the groove, reflecting a dynamic balance between groove and gravitational drainage.

3.4 Retention

Now that we have identified transport mechanisms, whether on a smooth or grooved surface, let us try to understand the link between them and fluid retention on the surface.

3.4.1 Smooth substrate

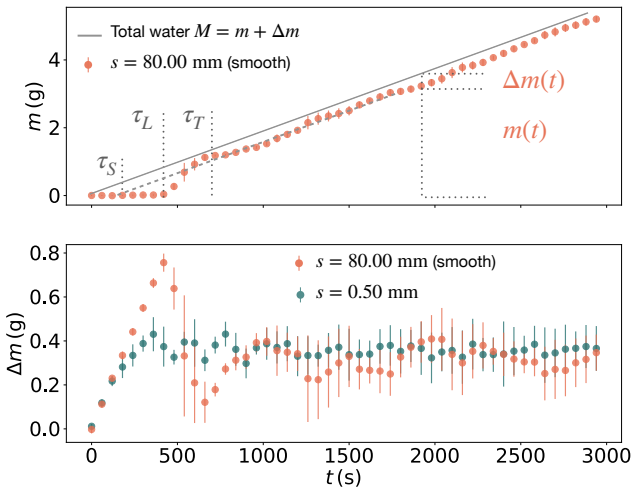

Figure 3.5: Condensation dynamics on smooth and grooved substrates. (Top) Collected water mass $m(t)$ on a smooth surface shows three regimes: a latency period with no collection ($0 \to \tau_L$), a transient burst when synchronized droplets reach the detachment radius R_d ($\tau_L \to \tau_T$), and a steady state where $m(t)$ grows linearly at a constant condensation rate c ($\tau_T \to \infty$). The gray line indicates the total condensed mass $M(t)$, with the vertical gap to $m(t)$ giving the retained mass $\Delta m(t)$. The extrapolated time τ_S marks when the first droplet would arrive if the system were operating directly in steady state. (Bottom) Retained mass $\Delta m(t)$ for different groove spacings s. Narrow grooves shorten the latency and suppress the transient burst, but the steady-state retention Δm remains comparable to the smooth case. This challenges the view that shorter latency always τ_L signals higher drainage efficiency, showing instead that Δm is the key metric for long-term performance.

Results

To establish a baseline, we first examine condensation and drainage on a smooth vertical substrate. Figure 3.5(top) shows the collected water mass $m(t)$ over time, while Figure 3.5(bottom) presents the mass retained on the substrate $\Delta m(t)$. Both curves reveal three distinct regimes. In the latency regime ($0 \to \tau_L$), $m(t)$ remains at zero, indicating that no droplet has yet reached the collection vessel, while $\Delta m(t)$ increases steadily as droplets grow on the surface. The transient regime ($\tau_L \to \tau_T$) begins once the first droplet arrives at the vessel, producing a sharp rise in $m(t)$ and a corresponding drop in $\Delta m(t)$ as retained water is evacuated. Finally, in the steady-state regime ($\tau_T \to \infty$), $m(t)$ increases linearly with a constant slope, and $\Delta m(t)$ fluctuates around a stable average. We now dive further into each of these regimes.

The latency regime corresponds to the period when condensation is already active, but all water remains on the surface. Droplets grow until they reach the detachment radius R_d, the smallest size at which they slide under gravity. Classical theory predicts motion at a critical radius

$$R_c = \lambda \sqrt{\frac{\cos\theta_R - \cos\theta_A}{A}} = 1.80\,\text{mm}, \tag{3.2}$$

with $A = 0.33$ related to the drop cap geometry [129]. However, in our experiments, droplet motion frequently occurs at radii smaller than the theoretical critical radius R_c. We define the observed onset of sliding as the detachment radius, denoted R_d

$$R_c > R_d > 1\,\text{mm}. \tag{3.3}$$

We attribute the discrepancy between R_c and R_d to the dynamic nature of coalescence during condensation. When two droplets merge, the resulting droplet undergoes a rapid reconfiguration, during which the triple contact line moves significantly. Gao *et al.* [153] showed that the friction opposing droplet motion is considerably lower when the droplet is already in motion than when it is static, an effect analogous to solid-on-solid friction. This reduction in resistance during contact line displacement likely facilitates the onset of sliding at smaller droplet sizes. It thereby explains the difference between the theoretical critical radius R_c and the experimentally observed detachment radius R_d. As they slide down the surface, these droplets sweep smaller droplets along their path, leaving behind a nearly dry trail. These descending droplets accumulate on the lower edge of the substrate, where they remain hanging until they detach (visible in Figures 3.2 & 3.3). These droplets will be further explored in Chapter 4. The moment the first droplet detaches and reaches the collection container defines the latency time τ_L.

Let us now turn to the burst of collection that marks the transient regime. Its origin lies in the initial synchronicity of droplet growth, which keeps the droplet size distribution narrow at early times. As a result, many droplets reach the detachment radius R_d almost simultaneously and slide down within a short interval, producing a sharp, temporary increase in the collected water mass $m(t)$ just after τ_L. This synchrony also allows us to estimate the theoretical maximum retention of the smooth substrate during latency. Assuming droplets of radius $R_d = 1\,\text{mm}$ arranged in a hexagonal lattice, the configuration that maximizes surface occupancy, the packing fraction is $\epsilon = 0.91$, representing the ratio of droplet-covered to total

surface area. The volume of a single droplet is given by [129]

$$\Omega_d = A\pi R_d^3, \tag{3.4}$$

The corresponding maximum retained mass is

$$\Delta m_L^{\max} = \frac{\epsilon L^2}{S_d}\rho\Omega_d = 1.92\,\mathrm{g}, \tag{3.5}$$

where S_d is the droplet contact surface. This value is more than twice the experimental peak of Δm observed in Figure 3.5(bottom), showing that in practice, imperfect synchrony and coalescence-induced shedding prevent the surface from reaching this upper bound. The estimate, therefore, represents a worst-case retention scenario, assuming perfect packing and no early drainage, and will vary with substrate wetting properties through A. After this initial burst, synchrony progressively decays, marking the transient regime ($\tau_L \to \tau_T$), until the system approaches steady state.

Finally, the steady-state regime commences when the collection rate stabilizes, defining a straight slope in the $m(t)$ graph of Figure 3.5(top). Thermodynamic constraints govern this rate: for condensation to occur, the latent heat of vaporization must be removed. In our setup, heat is dissipated by thermal exchange with ambient air maintained at 20°C in the climate chamber. Because this process does not depend on the surface texture [100, 96], the condensation rate remains constant across all substrates, with a measured value of $c = 1.9\ 10^{-3}\,\mathrm{g/s}$. It allows us to estimate the total amount of water condensed $M(t)$ at any time t. Indeed, it corresponds to a straight line of slope c passing through the origin of the graph. As we measure the collected water $m(t)$ and we know the total amount of water condensed $M(t)$, we deduce the amount of water retained on the surface $\Delta m(t)$ during the steady state phase, such as

$$\Delta m(t) = M(t) - m(t) \tag{3.6}$$

In Figure 3.5(top), these three quantities are represented. The gray line with slope c is the total amount of water condensed $M(t)$, dots represent the water collected in the vessel $m(t)$. The vertical gap between this reference and the experimental $m(t)$ curve provides a dynamic estimate of $\Delta m(t)$. Once the system reaches the steady state ($t > \tau_T$), the retained mass Δm fluctuates around a stable average value, as visible on Figure 3.5(bottom).

Model

Can we predict the retained mass on a smooth substrate, Δm_s, during the steady-state regime? We propose a semi-empirical model that considers only the water resting directly on the surface, explicitly excluding hanging droplets, which will also be neglected in the following models. These suspended droplets (visible on the bottom part of Figures 3.2 & 3.3) are modeled as half-ellipsoids, with the major axis corresponding to the droplet width, the minor axis to the substrate thickness (3 mm), and the height taken from image measurements. Their volume, measured through image analysis, accounts for about 5–10% of the total retained mass Δm.

We measured the time interval Δt between successive droplet sliding events, along with the average width of the trails they leave behind. From these measurements,

we estimate a trail width $2R_t = 5.34 \pm 0.88\,\text{mm}$. The mean time interval between events is $\Delta t = 22.13 \pm 21.85\,\text{s}$. The fact that the standard deviation is of the same order as the mean suggests that droplet shedding follows a Poisson process, in which events occur independently at a constant average rate. In such a regime, the waiting times between events are exponentially distributed, reflecting the absence of temporal correlation between successive sliding events. Based on this, we estimate a characteristic surface renewal time

$$t_r = \frac{\Delta t\, L}{2R_t} = 331.5\,\text{s}. \tag{3.7}$$

This time is also the characteristic time of drainage memory. It obviously depends on the condensation rate c. From this, we infer the average retained mass on a smooth substrate

$$\Delta m_s = \frac{c\, t_r}{2} = 0.31\,\text{g}, \tag{3.8}$$

where c is the measured condensation rate. This prediction agrees well with experimental measurements ($\Delta m_s = 0.35 \pm 0.08\,\text{g}$), although it remains a simplified model that neglects the complex dynamics of coalescence-driven growth.

In summary, for a smooth substrate, the retained water mass is mainly determined by the time it takes for droplets at the top to grow, detach, and slide down, sweeping up others along the way. This time, and thus the average retention, depends on the condensation rate and both detachment radius R_d and trail width $2R_t$. When scaled to a $1\,\text{m}^2$ surface, the retained mass reaches about 54 g of water, or roughly 5 cL. This volume corresponds to nearly 15% of the total dew that can be collected on a productive night [137, 151], and highlights the importance of minimizing retention to improve the efficiency of passive water collectors.

3.4.2 Spacing variation

We showed in Section 3.3.2 that grooves introduce very specific transport mechanisms. Therefore, we seek to understand their impact on surface retention.

Results

To ensure stable groove drainage conditions, we carefully set their aspect ratio in accordance with the condition outlined in Equation (3.1). Specifically, with an average contact angle of $\theta = 63°$, this leads to the requirement that $d/w > 0.6$. Therefore, we select $d/w = 1.00$ with $d = w = 0.20 \pm 0.01\text{mm}$ to accommodate potential imperfections in the substrate.

We start by examining the amount of water retained on a sample with a groove spacing of $s = 0.50\,\text{mm}$, as shown in Figure 3.5(bottom). Several observations emerge. First, the latency time τ_L is shorter. Second, the intermediate regime is nearly absent. Finally, despite these two aspects suggesting that this sample may be more efficient than the smooth reference, the actual amount of water retained on the surface during the steady state regime, Δm, is found to be quite similar. This observation challenges the previously proposed link between latency time and surface efficiency [22].

To capture this effect, we introduce a new characteristic time, τ_S. It estimates how long it would take for the first droplet to be collected if the system started

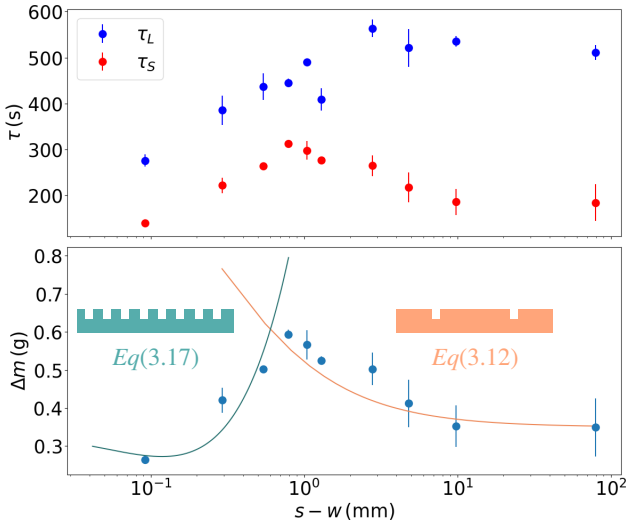

Figure 3.6: (Top) Comparison of latency time τ_L (blue) and extrapolated steady-state time τ_S (red) as functions of plateau width $s - w$, with $w = 0.2\,\text{mm}$ held constant. For small s, both times scale similarly, indicating negligible transient effects. For larger s, the increasing divergence between τ_L and τ_S reflects excess water retention from early-stage synchronized droplet growth. (Bottom) Total retained water mass Δm as a function of plateau width $s - w$. Experimental data (blue circles) reveal two opposing trends: retention increases with s for densely grooved substrates ($s < 1\,\text{mm}$), then decreases for larger spacings, approaching the smooth-surface limit. Orange and green curves correspond to asymptotic models valid for sparsely (Eq. 3.12) and densely grooved (Eq. 3.17) regimes, respectively.

directly in steady state. We obtain τ_S by extrapolating the steady-state $m(t)$ curve back to the time axis (Figure 3.5(top):

$$\tau_S(s) = \frac{\Delta m(s)}{c}, \tag{3.9}$$

where $\Delta m(s)$ is the steady-state retained mass for spacing s, and c is the condensation rate.

Figure 3.6(top) compares τ_S with the measured latency time τ_L. For small spacings ($s < R_d$), the two times scale proportionally, showing that densely grooved substrates exhibit little or no transient regime. Beyond R_d, however, the curves diverge: τ_L saturates near $s \approx 3\,\text{mm}$, while τ_S decreases. This divergence reflects a transient accumulation of water caused by synchronized droplet growth. The excess is progressively drained as the system relaxes into a steady state. In practice, substrates with a τ_L similar to the smooth surface all display the same burst of retained mass, revealing that τ_L predicts the onset of collective shedding but not the long-term efficiency of drainage, as clearly visible on Figure 3.5(bottom).

This observation leads us to compare samples based on the average retained mass Δm during the steady-state regime. These values are reported in Figure 3.6(bottom) for groove spacings ranging from $s = 0.30\,\text{mm}$ to $s = 80.00\,\text{mm}$, the latter serving as a smooth-surface reference. In this Figure, we express the horizontal axis not in terms of s, as done previously, but in terms of the plateau width $s - w$. Since the groove width w is held constant at $0.2\,\text{mm}$, the plateau width is directly

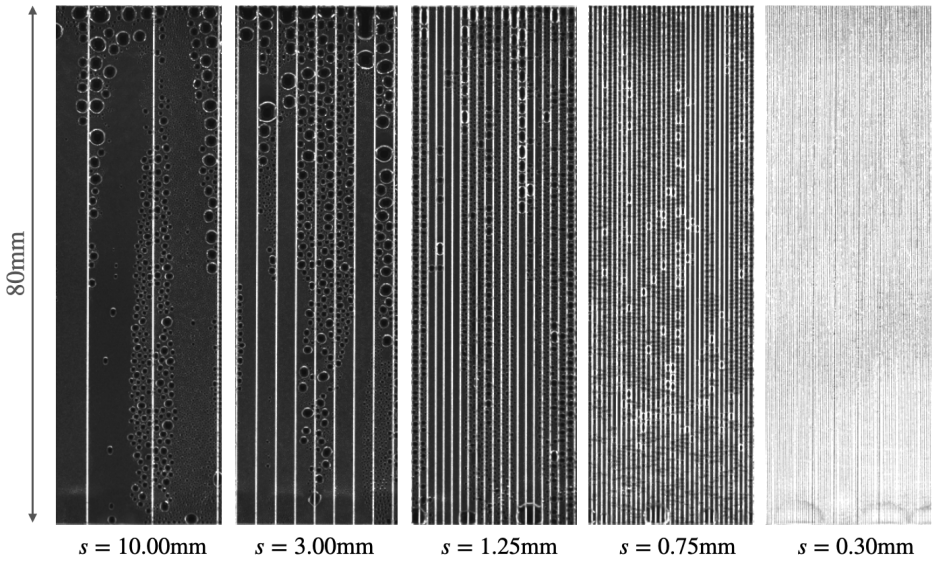

Figure 3.7: Snapshots of condensation patterns in the steady state ($t > 2000\,\mathrm{s}$) for substrates with groove spacing increasing from left to right: $s = 10.00$, 3.00, 1.25, 0.75, and $0.30\,\mathrm{mm}$. At large spacing ($s \approx 10\,\mathrm{mm}$), the surface resembles a smooth substrate, with wide striped bands formed by sweep droplets sliding under gravity and leaving trails of width $2R_t$, occasionally accompanied by satellite drops. At intermediate spacing ($s \approx 3\,\mathrm{mm}$), the bands narrow and droplet size becomes limited by s, constraining vertical coalescence. Drying events become more frequent, generating straddling droplets that can evolve into sweep droplets mid-height, although these often stop partway and are absorbed by grooves, suppressing efficient drainage. At very small spacing ($s \approx 0.75\,\mathrm{mm}$), sweep droplets vanish altogether. Straddling droplets formed during drying remain pinned and are reabsorbed, leaving only laterally confined droplets with no correlation in size across the surface. The progression highlights a transition from gravity-driven drainage with memory effects (left) to groove-constrained dynamics dominated by groove drainage (right).

proportional to s, and the underlying control parameter remains the groove spacing. As expected from Equation 3.9, Δm exhibits a similar trend to that of τ_S. Two opposing regimes can be identified. In the range $s - w < 1.00\,\mathrm{mm}$, the retained mass Δm increases with increasing plateau width. However, beyond $1.00\,\mathrm{mm}$ and up to the smooth-surface case, this trend reverses: further increasing the plateau width leads to a decrease in the amount of retained water.

To understand this antagonistic behavior, we analyze images taken in the steady state ($t > 2000\,\mathrm{s}$) for various spacings ($s = 0.30 - 0.75 - 1.25 - 3.00 - 10.00\,\mathrm{mm}$) represented in Figure 3.7. For large spacings ($s \approx 10\,\mathrm{mm}$), the surface resembles that of a smooth substrate. One observes the characteristic striped pattern made up of droplet clusters of similar sizes. Coalescence events produce sweep droplets, which then slide freely, clearing a trail of width $2R_t$. Occasionally, satellite droplets are emitted along the way. Since droplets are not geometrically confined by the grooves, successive coalescence events during growth tend to shift their center of mass away from the groove axis. As a result, apart from a few isolated drying events, primarily observed during the early stages of condensation, the grooves appear to contribute little to drainage compared to gravitational shedding.

When the spacing is reduced ($s \approx 3\,\mathrm{mm}$), the striped pattern becomes tighter, with band widths now limited by the spacing s. As a result, grooves limit the size

of static droplets within each band, constraining coalescence along the vertical direction and limiting the spontaneous formation of sweep droplets. On the contrary, drying events are more frequent, generating straddling droplets along the groove. The lowest droplet generated is typically the one that has the lowest hydrostatic pressure. It then drains fluid from upward droplets and evolves into a straddling sweep droplet. Thus, sweep droplets are no longer initiated exclusively from the top of the sample, but can also form mid-height, as illustrated in Figure 3.4. As s decreases, sweep droplets are less likely to reach the bottom of the sample. Instead, they stop mid-way and are absorbed by a groove, further reducing drainage efficiency. Finally, these sweep droplets no longer leave satellite droplets behind. Since they straddle a groove as they descend, any potential satellite droplet is rapidly absorbed by the groove.

In the limit of very narrow spacing ($s \approx 0.75\,\mathrm{mm}$), even sweep droplets generated by drying are absent. Occasionally, groove-spanning droplets appear during drying episodes, but they remain fixed and are eventually absorbed by the groove. This results in a droplet distribution strictly limited in width by s, highly dispersed on the sample and lacking any clear size correlation between neighboring droplets. There is nothing left similar to the smooth case.

Model

The control variable in our model is the plateau width, $s - w$, since it defines the space where droplets can grow and coalesce. In our experiments, however, the groove width w was held fixed. This means that, in practice, all variations in $s - w$ come from changing s alone. With this in mind, we develop two asymptotic models that capture the dominant transport modes in the limits of large and small spacing. These models are not intended to describe every detail of the fluid dynamics, as fundamental theory is lacking on several key concepts (drop morphology on a grooved vertical substrate, coalescence-driven shedding, open groove drainage, drying phenomenon), but rather to provide physical insight into how retention evolves as groove spacing is varied.

In the large-spacing limit ($s > R_d$), the plateaus between grooves are wide enough to permit unconstrained droplet growth and lateral coalescence. In this regime, gravitational shedding is the dominant drainage mechanism. The grooves, while occasionally activated, act mainly as passive reservoirs and play only a secondary role in transport.

We model retention in this regime by assuming it is equivalent to that of a smooth substrate, Δm_s, but scaled by the surface fraction occupied by plateaus:

$$\Delta m_{\mathrm{plateau}} = \frac{\Delta m_s}{L^2} n_g (s - w) L = \Delta m_s \frac{s - w}{s}, \tag{3.10}$$

where $n_g = L/s$ is the number of grooves on the substrate. The grooves themselves contribute an additional retained volume given by

$$\Delta m_{\mathrm{grooves}} = n_g \rho L d w = L^2 \rho \frac{dw}{s}, \tag{3.11}$$

where d is the groove depth and ρ is the fluid density. The total retained mass for a sparsely grooved substrate is thus

$$\Delta m = \Delta m_s \frac{s - w}{s} + L^2 \rho \frac{dw}{s}, \tag{3.12}$$

shown as the orange curve in Figure 3.6(bottom).

This formulation assumes that the grooves remain mostly filled on average, which is consistent with observations that gravitational shedding dominates drainage when spacing is large. While this approach simplifies groove dynamics, it is expected to hold in situations where wide plateaus allow for unconstrained droplet growth and only limited interaction with grooves. We acknowledge that grooves can still be intermittently activated, occasionally altering droplet trajectories or triggering overflow events, but these effects are not explicitly captured in the model. They are assumed to have a secondary influence on overall retention.

In the opposite limit of narrow groove spacing ($s < R_d$), the drainage mechanism changes fundamentally: grooves are frequently activated and handle most of the water removal. As before, we model the total retention as the sum of contributions from grooves and plateaus.

We begin with the groove contribution. Grooves act as narrow reservoirs that can trap a residual amount of water even after drainage events, thanks to continuous condensation, for example. To capture this effect, we assume that the volume stored in grooves scales with the reference retention Δm_s, but weighted by the fraction of the surface occupied by grooves:

$$\Delta m_{\text{grooves}} = \frac{\Delta m_s}{L^2} n_g w L = \Delta m_s \frac{w}{s}, \tag{3.13}$$

where $n_g = L/s$ is the number of grooves across the sample. This simple form reproduces the two natural limits. When $s \to w$, the plateaus shrink to nothing, and the surface is essentially all grooves. In that case, retention tends to the smooth reference value, $\Delta m_{\text{grooves}} \to \Delta m_s$. At the opposite extreme, when s becomes large, the number of grooves drops, and their contribution to storage vanishes, $\Delta m_{\text{grooves}} \to 0$.

We now turn to the plateaus. These regions host droplets that are laterally confined by the plateau width $s - w$. To approximate their contribution, we assume that the median droplet diameter scales with the plateau width. This gives a droplet volume

$$\Omega_d = \frac{A\pi}{8}(s - w)^3, \tag{3.14}$$

where A is a geometrical factor linked to droplet shape. Because droplets are confined by plateau edges and often appear elongated (as in Figure 3.3), we take the packing fraction to be unity. This assumption also accounts for the presence of smaller droplets that fit between larger ones. The average number of droplets per plateau is then

$$n_d = \frac{4L}{\pi(s - w)}. \tag{3.15}$$

Multiplying by the number of plateaus $n_p = L/s$, the total mass stored on plateaus becomes

$$\Delta m_{\text{plateau}} = n_p n_d \Omega_d \rho = \frac{3}{8} L^2 \rho A \frac{(s - w)^2}{s}. \tag{3.16}$$

Here too, the asymptotic behaviors are clear. When $s \ll w$, plateaus vanish, and their contribution goes to zero. As s increases, droplet size scales with the growing plateau width, so $\Delta m_{\text{plateau}}$ rises sharply. However, this growth cannot continue indefinitely. Once s exceeds the detachment radius R_d, droplets on plateaus begin

to shed under gravity, and retention will be capped by shedding dynamics rather than geometry. For this reason, the model should not be extrapolated beyond R_d without additional corrections.

Combining both contributions, the total retained mass for densely grooved substrates is

$$\Delta m = \Delta m_s \frac{w}{s} + \frac{3}{8} L^2 \rho A \frac{(s-w)^2}{s}. \tag{3.17}$$

Plotted as the green curve in Figure 3.6(bottom), this expression captures the observed scaling of retention with groove spacing and agrees well with the experimental data in the dense-groove regime. It highlights how retention increases with groove density and how plateau-confined droplets dominate storage when $s < R_d$.

The model, however, is deliberately simple. It neglects processes likely active in this regime. Stable filaments may channel long-range capillary transfer or act as temporary reservoirs. Overflow shedding, when drying-induced droplets grow large enough to sweep the surface, is also ignored. Furthermore, the formulation depends only on spacing s, without explicitly accounting for groove depth d; that role is explored separately in the next section. Despite these omissions, the model provides a useful framework: it clarifies why retention scales with s and explains the shift in control from grooves to plateau-confined droplets.

Interestingly, the lowest retention is found in this densely grooved regime, where groove-mediated drainage dominates and droplet growth is strongly confined. However, the exact location of this minimum and its alignment with the model prediction remain uncertain. This is due to fabrication limits: in our study, groove patterns were engraved using a CO_2 laser cutter, whose resolution prevents precise control of the plateau width below 0.1 mm. To test the model's asymptotic predictions more robustly, and to resolve the minimum more accurately, finer manufacturing methods will be required. Photolithography, for example, could enable a more systematic exploration of extreme groove densities.

At the junction of the two models, near $s - w = 0.61\,\text{mm}$ (i.e., $s = 0.81\,\text{mm}$), the predicted maximum droplet radius is $(s-w)/2 \approx R_d/4$. This value appears much smaller than the detachment radius R_d. However, this gap can largely be attributed to the fact that drying events often produce straddling droplets, which span across two plateaus. These droplets reach a characteristic radius of $(2s+w)/2$, which for $s = 0.81\,\text{mm}$ gives $R = 0.9\,\text{mm}$, already close to R_d.

Why does a small difference remain? Part of the answer lies in the limitations of the model itself. First, R_d is an experimentally observed threshold rather than a sharply defined value, and its precise determination would require further analysis. Second, groove confinement constrains droplets into elongated shapes (Figure 3.3), making the spherical approximation inadequate. The groove edges may also act as pinning sites, increasing the apparent base angle and allowing confined droplets to hold more volume than spherical ones. Finally, the model does not capture the dynamics of droplets on grooved, and especially wet substrates, which may alter detachment thresholds.

Together, these effects highlight the complexity of the intermediate regime. Here, transport no longer follows a single dominant pathway: sweep droplets often originate mid-height during drying, their trajectories shaped by overflow and local wetting, and they may either slide or be reabsorbed. Neither asymptotic model fully captures this hybrid state, where coalescence, drying, and groove-mediated drainage overlap.

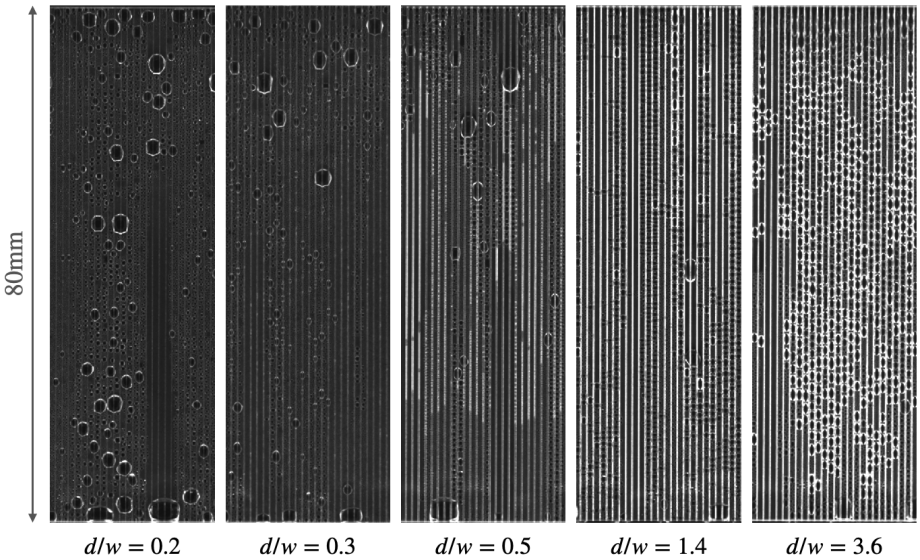

Figure 3.8: Snapshots of condensation patterns on grooved substrates with fixed spacing $s = 1.0\,\mathrm{mm}$ and increasing groove aspect ratios, from $d/w = 0.2$ to 3.6. As d/w increases, both droplet morphology and drainage mechanisms evolve. For shallow grooves ($d/w = 0.2$–0.5), droplet growth is still dominated by adsorption, coalescence, and gravitational shedding, but long-range coalescence (LRC) begins to play a role, producing large straddling droplets during the latency phase and gradually eroding drainage memory. Sweep droplets emerge lower on the substrate and with smaller radii as d/w increases. At larger aspect ratios ($d/w \geq 1$), lateral coalescence is strongly suppressed, and transport shifts to groove-mediated drainage. Droplets become geometrically confined to plateaus or grooves, while overflow-driven straddling droplets are only occasionally observed and typically reabsorbed. This progression highlights a transition from shedding-dominated to groove-dominated drainage as groove depth increases.

3.5 Groove aspect ratio variation

In the previous section, we showed that fixing the groove geometry in the F^- regime, favorable to impregnation (see Section 1.3.2), and varying the spacing s leads to distinct drainage mechanisms, each associated with different retention behaviors. One underlying assumption in the densely grooved model was that groove geometry does not significantly affect retention as d is absent of Equation(3.17). To test the robustness of this assumption, and to probe the limits of groove-controlled drainage, we now explore the role of groove aspect ratio d/w under drainage-dominated conditions ($s \leq R_d = 1\,\mathrm{mm}$). This section is deliberately exploratory: our aim is not to develop a full model, but to identify qualitative transitions in droplet morphology and transport dynamics as d/w increases.

Figure 3.8 presents a series of substrates with fixed spacing $s = 1\,\mathrm{mm}$ and increasing aspect ratios from $d/w = 0.2$ to 3.6. Let us first describe the visible changes induced by this variation. On a smooth substrate ($d/w = 0$), droplets grow through adsorption and coalescence, with no directional constraints. The early phase of condensation is marked by simultaneous and spatially uniform nucleation, leading to global synchronization. This collective growth triggers a burst of shedding during the intermediate regime. Transport is driven entirely by gravitational

shedding: droplets typically detach near the top of the substrate, sweep smaller droplets along their path, and leave behind a clean trail of width approximately 2λ. This trail resets nucleation locally, resulting in bands of similarly sized droplets, an expression of short-term drainage memory. The droplet population spans a broad range of sizes.

As the groove aspect ratio increases ($d/w = 0.2$ to 0.5), the system enters a more complex regime. Droplet growth still occurs via adsorption and coalescence, but long-range coalescence begins to play a significant role. Coalescence becomes increasingly constrained in the vertical direction as grooves deepen. LRC, combined with classical coalescence, leads to the early emergence of large straddling droplets during the latency phase. This process introduces local desynchronization of droplet sizes, which progressively erodes the drainage memory. Transport remains dominated by shedding but is now assisted by LRC, which enhances growth speed. Because LRC promotes the growth of downstream droplets, sweep droplets tend to initiate lower on the substrate. The radius of sweeping droplets also decreases with increasing d/w, narrowing from 4–5mm for $d/w = 0.2$ to 2–3mm ($\approx 2s$) at $d/w = 0.5$. The static droplet population becomes geometrically constrained as d/w increases. Plateau and groove droplets are clearly distinct, shaped by the substrate's topography. Straddling droplets appear more frequently, triggered by drying events, and their maximum diameter decreases with d/w, from 2λ down to approximately $2s$. These droplets can be stable or transient, momentarily involved in a drying phenomenon.

For large aspect ratios ($d/w \geq 1$), droplet growth occurs primarily through adsorption and vertical coalescence, with lateral interactions largely suppressed by the groove geometry. Transport is dominated by groove drainage, which becomes the main pathway for water removal. Occasionally, we observe overflow events, characterized by temporary straddling droplets appearing above the groove. These droplets are either reabsorbed shortly afterwards or, in rarer cases, grow large enough to become sweep droplets. However, the formation of such mobile droplets becomes increasingly rare as the aspect ratio increases. At high d/w, groove absorption is more localized and less frequent: overflow events tend to affect only short segments of the substrate. The static droplet population is clearly split between plateau and groove droplets, each constrained in shape and size by the underlying texture.

We analyze how groove geometry influences water retention by varying the aspect ratio d/w from 0.2 to 3.5, across three groove spacings representative of the densely grooved regime: $s = 1.0$, 0.5 and 0.3 mm. To isolate the role of geometry, we compare retention not in absolute terms, but by normalizing the excess mass relative to a smooth surface and scaling it to the plateau area. Specifically, we plot $(\Delta m - \Delta m_s)\, sL/L^2$, which quantifies how efficiently a groove–plateau unit evacuates water compared to an unstructured surface. Results are shown in Figure 3.9.

Two distinct regimes emerge. For low aspect ratios ($d/w \leq 1$), the curves remain flat and close to zero, indicating that groove geometry has little impact on retention. The differences observed between the s-dependent curves confirm that, in this regime, spacing governs drainage. This supports the assumption made in the densely grooved model: when $s \ll R_d$ and $d/w \approx 1$, the groove geometry can be neglected in the first approximation.

As d/w increases further, retention begins to rise, especially for $s = 1.0\,\text{mm} \approx R_d$.

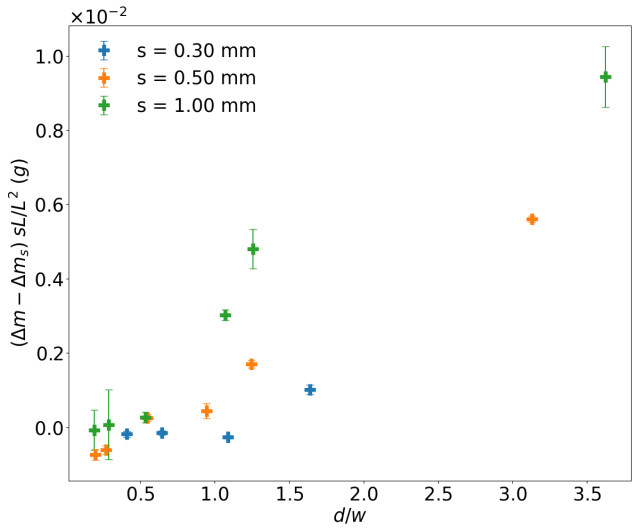

Figure 3.9: Normalized excess retention per plateau unit, $(\Delta m - \Delta m_s) \cdot s/L$, as a function of aspect ratio d/w, for three groove spacings ($s = 0.3$, 0.5, and $1.0\,\mathrm{mm}$). For small d/w, retention is comparable to that of smooth substrates and largely independent of groove geometry. For larger d/w, retention increases with groove depth, indicating a transition to geometry-controlled storage. The position of this transition depends on the spacing s, with smaller s delaying the onset of geometry sensitivity.

This marks the onset of a second regime where groove geometry does influence retention. In this case, the filled-groove model provides a better description, as more water accumulates within the groove volume. The transition from the flat to the sloped regime depends on spacing: the smaller the spacing s, the later this shift occurs. This behavior reflects the fact that, for a droplet to interact with the groove, it must grow large enough to span the plateau. Narrower spacing reduces this required size, increasing the frequency of groove–droplet interactions and enhancing drainage efficiency. As groove depth increases, so does its storage capacity, contributing to higher retention per groove–plateau unit.

However, care must be taken when interpreting these trends. Since retention is expressed per unit plateau, the total mass stored on a sample also depends on the number of grooves, which increases as spacing decreases.

Comparing Figures 3.7(left) and 3.8(right) reveals consistent patterns. Substrates with dense grooves ($s = 0.75\,\mathrm{mm}$, $d/w = 1$) and those with deeper grooves at slightly wider spacing ($s = 1.0\,\mathrm{mm}$, $d/w = 3.6$) both limit droplet size and channel transport through the grooves, suppressing gravitational shedding. The difference lies in where water is stored: higher d/w increases groove capacity, while larger s shifts storage toward the plateaus.

In contrast, wide-spacing, moderate-depth substrates ($s = 10.0\,\mathrm{mm}$, $d/w = 1$) and tight-spacing, shallow-grooved ones ($s = 1.0\,\mathrm{mm}$, $d/w = 0.2$) both sustain large, unconstrained droplets and gravity-driven drainage. Yet the pathways differ. Wide spacing promotes sweep droplet formation through classical coalescence, largely independent of the grooves. Shallow grooves encourage long-range coalescence (LRC), which accelerates local droplet growth and promotes faster shedding events.

Together, these comparisons highlight a central principle: drainage and retention

are governed by a balance of fluxes between how much water condenses and how efficiently it can be evacuated. In densely grooved substrates, where gravitational shedding may be suppressed, this balance becomes especially critical. The input flux is primarily set by the available condensing area, determined by the plateau width $s - w$, while the evacuation flux depends on the groove geometry, particularly the aspect ratio d/w.

3.6 Future works

Drying events emerged in this study as a decisive mechanism for reorganizing water within grooved substrates, yet several aspects of this process remain unresolved. We still do not know which groove geometry triggers drying most efficiently. Its behavior on more complex textures is equally unknown. Junctions or sudden depth changes may redirect, stop or fragment drying fronts, altering how water redistributes across the surface. Moreover, any optimal geometry may depend on the imposed condensing flux. A geometry that is effective at low flux might be overflowed at higher flux. Even the aspect-ratio criterion (Equation(3.1)), currently defined without gravity, is likely to shift on inclined substrates where hydrostatic pressure starts to matter. At the opposite extreme, very deep grooves may behave almost as independent channels, potentially decoupling groove drainage from surface drainage. Understanding how all these factors interact defines the next step toward a unified description of drying and groove-mediated transport.

Retention raises a different but equally important set of questions. We showed that grooves can increase the amount of water stored on a surface, a behavior similar to porous materials. This similarity naturally suggests that grooved substrates might be treated as a form of open porous medium. It means that grooved surfaces can store water like porous media, but can also redistribute it through long-range capillary pathways that pores simply cannot support, at least at the same speed. Identifying the consequences of this open interface, whether it enhances retention, facilitates drainage, or enables new modes of redistribution, is essential to clarify how grooved substrates should be conceptualized and modeled.

The behavior of shedding droplets also presents open questions. Our observations showed that coalescence can trigger sliding earlier than predicted because the contact line is already in motion, reducing resistance. We do not yet know how large a coalescence event must be to trigger motion. Moreover, sweeping droplets consistently interact with the droplets they meet on their path, but we lack a framework to predict whether these encounters will deflect or not a sliding droplet. A controlled collision experiment, where a sweeping droplet is guided into a resting one, could quantify these outcomes. If such interactions can be predicted or engineered, with identical or different fluid, they could form the basis for programmed droplet pathways [142], where droplets themselves act as temporary guides that steer sweep droplets across a surface.

A natural next step is a thermodynamic analysis of the system. The goal would be to quantify the real energy gain induced by geometrically constrained droplet growth. A first experiment could be straightforward: One could measure the power needed to keep a surface below the dew point and compare smooth and grooved substrates. This would already give a clear estimate of the energetic benefit of confinement. A full model would be more challenging as it would need to include

heat and mass transfer through droplets on the plateaus, but also through the liquid stored and flowing inside the grooves.

3.7 Summary

This chapter demonstrates that vertical grooves can fundamentally alter water retention during condensation, shifting the dominant drainage mode from gravitational shedding to groove drainage. By systematically varying groove spacing s with a fixed aspect ratio $d/w = 1$, we identified two limiting regimes. In the sparse-groove regime ($s > R_d$), retention is governed by gravitational shedding, with grooves acting primarily as passive reservoirs. In the dense-groove regime ($s < R_d$), droplets are confined to the plateaus and grooves are frequently activated, making groove-mediated drainage the primary pathway for water removal. Between these limits lies a transition zone, near the detachment radius R_d, where coalescence, drying, and groove transport overlap to produce hybrid drainage modes. Remarkably, water retention peaks in this intermediate region, illustrating the competition between transport modes.

We developed two asymptotic models, each capturing the scaling of retained mass in one of the limits, and showed that their divergence near R_d marks the boundary between the two dominant drainage mechanisms. Our results also reveal a previously unreported geometry-constrained condensation regime, in which droplets never exceed the plateau width. This confinement suppresses gravitational shedding and promotes groove-driven transport. Such surfaces could offer tailored thermal and optical properties, relevant for both passive water harvesting and functional heat-transfer surfaces.

Within the broader scope of this thesis, this chapter shows how surface geometry reorganizes not only droplet motion, as observed on fibers, but also droplet growth, coalescence, and long-range drainage across an entire two-dimensional substrate. The next chapter examines how this guided transport ultimately transitions into detachment at the lower edge, where geometry, pinning, and fluid influx interplay to determine when and where water is finally released.

4

Hanging droplets at the bottom edge of a condensing grooved plate

4.1 Motivation

Water flowing down vertical surfaces is a familiar sight in rainy climates, yet beneath this simplicity lies a remarkable diversity of morphologies. Depending on surface affinity and flow rate, water can appear as isolated droplets [15, 30], narrow rivulets [16, 52], or continuous films [156, 48, 81] These behaviors have been widely explored on different surfaces, from wide flat panes [157, 16] to cactus spines [144, 158] and fibers [74, 18, 71, 88, 159, 160], revealing how geometry and wetting properties shape drainage.

However, one region of these vertical surfaces has received far less attention: the lower edge, where the downward flow meets an abrupt discontinuity [83, 89]. At this boundary, the mode of water release depends on both the shape of the incoming liquid and the surface geometry [17, 161, 162, 163]. A droplet may stick to the edge, a rivulet may cling and drip, and a film may fragment [164]. Despite its prevalence in both natural and engineered systems, the transition from surface transport to detachment at an edge remains poorly studied [165].

This question becomes critical under condensation, where water forms continuously and must be removed efficiently [137, 154, 166]. In dew collectors and heat exchangers, the fate of condensed water at the lower edge influences both retention and efficiency. Surface structuring offers a way to influence this process. Grooves are known to influence liquids in both static and dynamic ways. Statically, they pin contact lines [33, 150], elongate droplets [167, 168], and draw liquid through capillary suction [40, 169, 170]; dynamically, they speed up transport along their length [171], guiding droplets [82, 86] or even stretching rivulets into thin films [172]. Under condensation, this dual role suppresses gravitational shedding and draws the liquid into the grooves, allowing drainage within the texture rather than

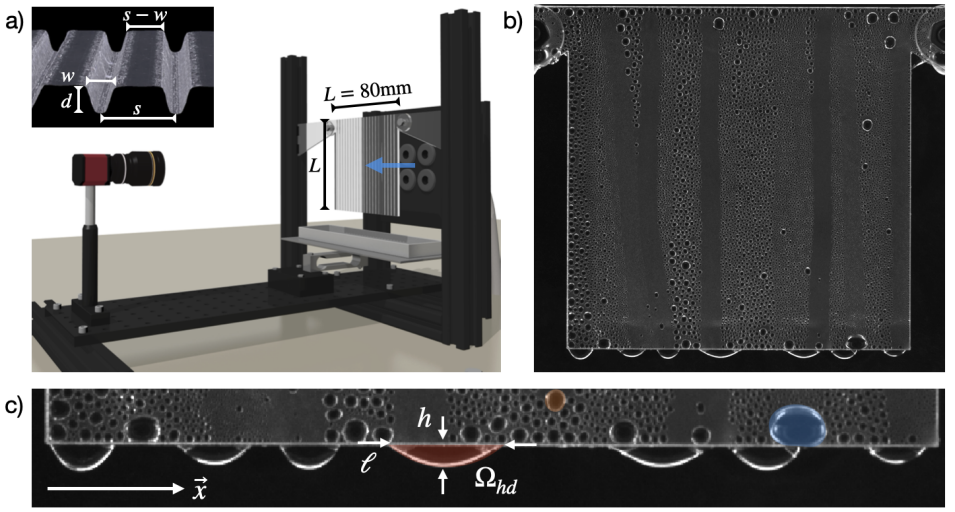

Figure 4.1: (a) Experimental setup. Warm, humid air is generated by bubbling compressed air through a heated water reservoir and directed toward the vertically mounted substrate via four nozzles (right). Condensation forms on a square acrylic plate of side length $L = 80.00\,\mathrm{mm}$, either smooth ($s = 80.00\,\mathrm{mm}$) or patterned with parallel vertical grooves. The grooves have depth d and width w, while the spacing s between grooves ranges from 0.30 to $10.00\,\mathrm{mm}$. The flat region between two adjacent grooves is called a plateau, with a width equal to $s - w$. (b) Steady-state condensation on a smooth substrate showing the characteristic band structure formed by successive sweeping droplets sliding down the surface. (c) Close-up view of the lower edge highlighting the three droplet types: orange, droplets fully on the vertical face; blue, flank droplets resting on the edge; and red, hanging droplets below the substrate.

on the surface. [173, 22].

The previous chapter showed that groove spacing reorganizes water growth and drainage along the vertical face, funneling condensate into the texture. The next open question in the thesis is therefore how this guided, groove-fed flow ultimately transitions into detachment at the lower edge. In particular, little is known about how edge geometry shapes the moment and location at which condensed water leaves the substrate. Addressing this question requires examining the lower boundary directly, where groove-driven transport meets gravity-driven release.

4.2 Experimental setup

The traditional method of forced condensation involves cooling a surface by bringing it into contact with a thermal exchanger. Like condensation forming on a cold water bottle out of the fridge, water condenses when a surface is cooled below the dew point. While reliable, this technique is slow, typically yielding condensation rates around $6\,\mathrm{g/m^2\,h}$ [96, 22, 100]. As a result, experiments often require several hours to complete.

Our approach takes the opposite route: instead of cooling the surface, we blow warm, humid air onto a room-temperature substrate, just like breathing on a cold window. Using this method, we achieve rates up to $900\,\mathrm{g/m^2\,h}$, 150 times faster,

thereby reducing experiment time and enabling multiple tests across a wide range of parameters. Experiments are performed in a climate-controlled chamber at $T = 20.0 \pm 0.5°\text{C}$ and relative humidity $RH = 65 \pm 2\%$. To generate the humid airflow, we heat a water reservoir to $75 \pm 2°\text{C}$. Compressed air is injected through a diffuser at the bottom of the reservoir. As it rises, the air warms up through thermal exchange and becomes saturated with water vapor. This warm, moist air exits through four nozzles located on the reservoir lid and flows perpendicularly toward the vertically suspended substrate at a velocity $v < 1\,\text{m/s}$ (see Figure 4.1). These velocities are comparable to those occurring in natural dew formation environments [137, 151].

The substrate reaches a temperature of $T = 45.0 \pm 1.5°\text{C}$ within about 100 seconds. At this temperature, liquid water has a density $\rho = 992\,\text{kg/m}^3$ and surface tension $\sigma = 69 \times 10^{-3}\,\text{N/m}$ [152], corresponding to a capillary length of $\lambda = \sqrt{\sigma/\rho g} = 2.67\,\text{mm}$. The substrate is a square acrylic plate (TroGlass Clear) with thickness $e = 3\,\text{mm}$ and side length $L = 80\,\text{mm}$. Its wetting properties are characterized by a static advancing contact angle $\theta_A = 78.0 \pm 4.5°$ and a receding angle $\theta_R = 48.0 \pm 4.7°$, yielding an average contact angle of $\theta = 63.0 \pm 4.6°$.

Surface structuring is done with a laser cutter (Trotec Speedy 100), producing grooves with spacing s ranging from 0.30 to 10.00 mm, with depth d and width w (specified when appropriate and measured using optical microscopy (Keyence VHX), see inset of Figure 4.1). We refer to the flat regions between adjacent grooves, of width equal to $s - w$, as plateaus. A smooth surface ($s = 80.00\,\text{mm}$) serves as the reference. Each experiment lasts 50 minutes (3000s) and is repeated three times to ensure reproducibility.

4.3 Results

Condensation on a smooth vertical surface proceeds in a well-known sequence. Nucleation begins at material imperfections, which act as preferential sites for droplet formation [97]. Droplets grow first by vapor adsorption and then by coalescence with neighbors. Once a droplet reaches the critical radius $R_c \approx 1\,\text{mm}$ [173], its weight exceeds the surface retention force, and it starts sliding downward [44, 153]. These sliding droplets, known as sweeping drops, collect smaller ones along their path [154], rapidly increasing in size. As they descend, droplets may become unstable and break up into smaller ones due to the Plateau-Rayleigh instability [29, 30], limiting their volume and leaving behind a narrow, nearly dry trail of width approximately 2λ wide. This dry wake provides a clean region for renewed nucleation, setting up a continuous condensation–drainage cycle. Because droplets near the top of the surface experience less frequent sweeping, they have more time to grow and are more likely to initiate a shedding event. As a result, drainage is managed progressively, droplet by droplet, from the top part of the surface, as illustrated by the vertical stripes in Figure 4.1(b). To understand how this drainage translates into dripping, we now focus on the lower edge of the substrate, shown in Figure 4.1(c). We identify three distinct droplet types: droplets entirely on the vertical surface (orange), flank droplets resting on the edge (blue), and hanging droplets located below the substrate (red).

We now examine how hanging droplets evolve. Figure 4.2(a) presents the spatio-temporal evolution of dripping on a smooth substrate ($s = 80.00\,\text{mm}$). The

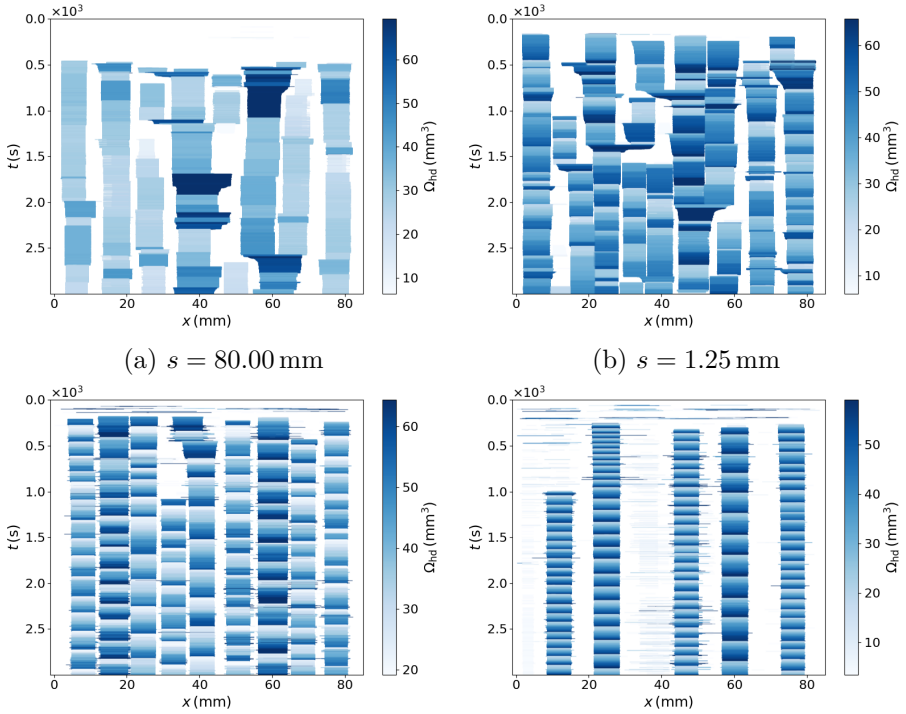

(a) $s = 80.00\,\mathrm{mm}$ (b) $s = 1.25\,\mathrm{mm}$

(c) $s = 0.50\,\mathrm{mm}$ (d) $s = 0.30\,\mathrm{mm}$

Figure 4.2: Spatio-temporal evolution of hanging droplets below the lower edge for decreasing groove spacing: (a) $s = 80.00\,\mathrm{mm}$, (b) $1.25\,\mathrm{mm}$, (c) $0.50\,\mathrm{mm}$, (d) $0.30\,\mathrm{mm}$. Each bar represents one droplet; its length corresponds to droplet width ℓ and its color to volume Ω_{hd}. The vertical axis is time t, while the horizontal axis corresponds to position x along the edge. At large spacing (a), hanging droplets appear after a latency of $\sim 500\,\mathrm{s}$ and form irregular, drifting bands produced by sporadic impacts of sliding droplets. As grooves are introduced (b–c), bands become thinner, straighter, and more numerous, reflecting increased positional stability and smoother volume evolution. For the most closely spaced grooves (d), the number of hanging droplets decreases, but their positions and volume variation frequencies become highly regular. The dripping pattern transitions from intermittent and impact-driven to structured and quasi-periodic as groove spacing decreases.

horizontal axis indicates droplet position x along the edge, the vertical one indicates time t evolution and the color refers to drop volume Ω_{hd}. We estimate the latter as a half-ellipsoid

$$\Omega_{hd} = \tfrac{1}{6}\pi \ell h e, \tag{4.1}$$

with drop width ℓ, height h, and thickness e approximated to the substrate thickness ($e = 3\,\mathrm{mm}$). At first glance, the figure shows a set of colored bands extending vertically across the plot. The pattern itself is composed of narrow horizontal bars, each representing one frame of observation (recorded every second), with its length proportional to the droplet width ℓ and its color scaled by the volume Ω_{hd}. Each band is thus a sequence of droplets appearing, growing and detaching as function of time. These bands reveal that droplets repeatedly form at the same location along the edge. Hanging droplets appear after a latency of about 500 s, once sweeping drops from the vertical face reach the lower edge. The resulting bands differ slightly in width and tilt, showing that new droplets often form near the same locations as their predecessors, but that these positions may shift gradually over time. Their color changes abruptly, revealing sudden variations in droplet volume due to coalescence or impact with a sweep droplet. Bands merge as neighboring hanging droplets coalesce, and reappear when there is sufficient room for a sweeping or flank droplet to convert into a new hanging one. The outcome is a self-organized yet unpredictable dripping pattern, governed by the intermittent supply of water from the vertical face.

To explore how grooves alter this behavior, we gradually decrease their spacing s. Groove geometry is $d = 211 \pm 7\,\mu\mathrm{m}$ and $w = 206 \pm 5\,\mu\mathrm{m}$ yielding a aspect ratio $d/w = 1.02$. When the first grooves are introduced ($s = 1.25\,\mathrm{mm}$), the dripping pattern changes noticeably. The bands become more numerous, thinner, and straighter, showing greater stability. Their color transitions are smoother, suggesting more gradual filling. Interactions between neighboring bands are more frequent, even if droplets now appear in a more continuous and evenly spaced way. At narrower spacing ($s = 0.50\,\mathrm{mm}$), the pattern becomes strikingly regular. Bands are thin, vertical, and closely packed, while color oscillations are strong and periodic, marking steady cycles of filling and drainage. The width of each band remains constant in time, and droplet positions no longer shift. At the smallest spacing ($s = 0.30\,\mathrm{mm}$), the number of hanging droplets strikingly decreases and their positions become highly stable. Bands are perfectly vertical and widely spaced, with rapid and repetitive color oscillations. Large inactive regions remain between them, and subtle correlations appear: the droplet located at $x \approx 25\,\mathrm{mm}$ at $t \approx 1000\,s$ on Figure 4.2(d) slows its dripping when a new droplet begins to fill at $x \approx 15\,\mathrm{mm}$. The dripping pattern settles into a stable rhythm, reflecting the geometric constraint imposed by the underlying texture.

Figure 4.3 quantifies how groove spacing influences the dripping regime. In panel (a), the mean number of hanging droplets N_d exhibits two distinct trends. For large spacings, decreasing groove spacing increases the number of droplets; but once spacing falls below 1 mm, N_d drops abruptly. Panel (b) shows that a systematic diminution in droplet size accompanies this shift. The mean width ℓ decreases from about 8 mm on the smooth surface to 6.5 mm for the most structured samples ($s < 1\,\mathrm{mm}$), remaining close to twice the capillary length (2λ). The mean inter-drop gap behaves similarly for $s > 1\,\mathrm{mm}$, hovering near λ, but widens again once the grooves are densely packed, reaching values comparable to droplet size.

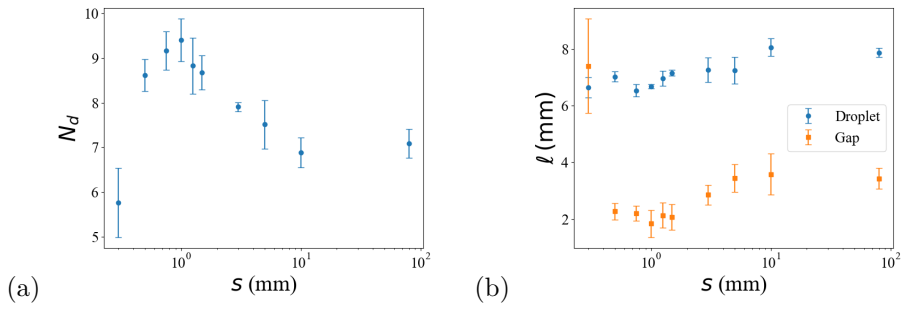

Figure 4.3: Evolution of hanging droplets in the steady regime ($t > 1000\,\mathrm{s}$). (a) Mean number of hanging droplets N_d as a function of groove spacing s. Two regimes appear: for large and intermediate spacings ($s > 1\,\mathrm{mm}$), the number of droplets increases as grooves are added; for narrow spacing ($s < 1\,\mathrm{mm}$), it decreases sharply as grooves become denser. This behavior closely mirrors the water-retention trend observed on the vertical face, with a transition near $s \approx R_c$. (b) Mean droplet width ℓ and mean inter-drop gap in the same steady regime. Droplet width decreases continuously as spacing narrows, from about $8\,\mathrm{mm}$ on the smooth surface to $6.5\,\mathrm{mm}$ on the most structured ones ($s < 1\,\mathrm{mm}$), corresponding roughly to twice the capillary length (2λ). The mean gap follows a similar trend for $s > R_c$ but shifted with a value around λ. Then it rises again for $s < R_c$, reaching values comparable to droplet size 2λ. Together, these measurements reveal a transition from intermittent, gravity-driven dripping to a geometrically constrained, periodic regime as groove spacing decreases.

Taken together, these measurements reveal a clear shift in dripping behavior with groove spacing: the system evolves from an erratic, gravity-fed pattern to a more gradual and stable one as the surface becomes more structured. The transition occurs around $s \approx R_c$, coinciding with the spacing where water transport along the vertical face changes from gravitational drainage to groove-guided flow. This correspondence suggests that the reorganization of dripping at the edge is not an isolated effect, but rather the continuation of a deeper transformation in how water moves across the entire surface, a transition whose mechanism becomes fully apparent when the grooves are most densely packed.

4.4 Discussion

To understand how groove structuring organizes dripping, we focus on the most densely patterned substrate ($s = 0.30\,\mathrm{mm}$), illustrated in Figure 4.4, with its spatiotemporal evolution shown in Figure 4.2(d). At this spacing, sweeping-drop drainage is completely suppressed, allowing us to isolate the sequence of events that transforms groove-fed flow into a stable dripping pattern at the lower edge.

At early times ($t = 160$–$254\,\mathrm{s}$), a first generation of flank droplets appears along the lower part of the vertical face. These droplets are fed through the grooves, which rapidly transport water downward, faster than it would with sweeping droplets. As they grow, the droplets often merge laterally, forming extended flank droplets that span several grooves. Some reach widths up to $33\,\mathrm{mm}$, over ten times the capillary length λ. Such droplets are unusual: based on the Bond number, which compares gravitational and capillary forces,

$$\mathrm{Bo} = \frac{\rho g \ell^2}{\sigma} = \frac{\ell^2}{\lambda^2} \approx 150, \tag{4.2}$$

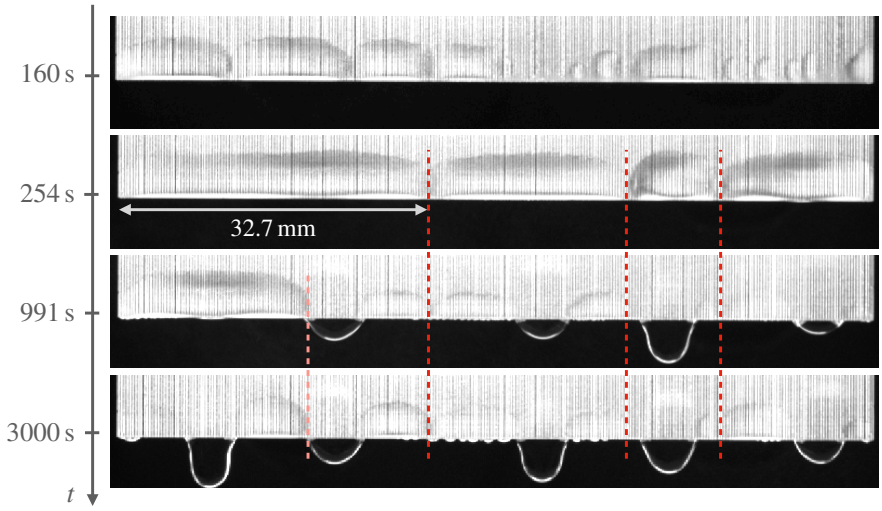

Figure 4.4: Time evolution of flank and hanging droplets on a densely grooved substrate ($s = 0.30\,\mathrm{mm}$, edge length $80\,\mathrm{mm}$). Snapshots at four key moments illustrate how groove-fed drainage gives rise to a stable dripping pattern at the lower edge. ($t = 160$–$254\,\mathrm{s}$): rapid formation and lateral merging of groove-fed flank droplets, some spanning over $30\,\mathrm{mm}$ in width; ($t = 991\,\mathrm{s}$): local detachment begins as the last large flank droplet is about to break, marking the final stage before the system settles; ($t = 3000\,\mathrm{s}$): the configuration remains unchanged long after the last breakup, reflecting the persistent steady state established shortly after $t = 991\,\mathrm{s}$. Red and rose dashed lines outline "fragmentation basins", zones where successive generations of flank droplets have broken up and stabilized. The groove network pins the boundaries of these basins, locking the spatial organization of the dripping pattern in place.

they should detach under their own weight. Instead, they remain pinned, stabilized by the grooves acting as capillary anchors [40, 41]. Yet, the slightly curved lower contours of these droplets suggest that gravity is beginning to overcome capillary pinning (visible at $t = 254\,\mathrm{s}$). A few seconds later, the heaviest flank droplets destabilize locally. The first hanging droplets appear directly below the points where the curved edges of the flank droplets begin to sag. Detachment is not necessarily symmetric; breakups occur at irregular locations along the droplet base, likely triggered by small imperfections at the substrate's lower edge. Each pendant droplet thus traces its origin to a previous and specific flank droplet, marking the coupling between the two types. Moreover, no flank droplet is ever observed directly above a hanging one. Once a groove supplies a hanging droplet, its capillary connection prevents the formation of a new flank droplet in the same vertical line.

After several minutes ($t = 991\,\mathrm{s}$), the last large flank droplet is about to break. This moment marks the final stage before the system settles into a stable, organized configuration. All the droplets that previously dominated the lower edge have fragmented, sometimes in multiple stages, into an alternating sequence of flank and hanging droplets. Through this cascade, each droplet progressively reaches equilibrium, resulting in a self-organized state that emerges from the balance between gravity and capillarity.

By the end of the experiment ($t = 3000\,\mathrm{s}$), more than $2000\,\mathrm{s}$ after the last major breakup, the droplet arrangement remains unchanged. The same flank droplets persist, continuously replenished through the grooves and periodically discharging into adjacent hanging droplets. The spatial distribution established after the first breakups persists, as highlighted by the red and rose dashed lines in Figure 4.4, which delineate "fragmentation basins". The competition between gravity and capillarity, observed on the smooth substrate, has thus evolved into cooperation for the grooved substrate: the grooves prevent sweeping drops and maintain capillary anchoring, the flank droplets buffer and redistribute water, and the hanging droplets provide a regular and localized release mechanism. Together, they form a groove-fed network that stabilizes dripping, making it regular and localized, yet still unpredictable in its precise position.

Having identified how dense grooving produces a stable dripping configuration, we now ask the reverse question: what happens as this structure gradually disappears? In other words, how does groove density control the stability and periodicity of the dripping regime? To address this, we compare substrates with progressively larger groove spacing ($s = 0.30$–0.50–1.25–$80.00\,\mathrm{mm}$) under steady condensation in Figure 4.5.

At the smallest spacing $s = 0.30\,\mathrm{mm}$, groove density is highest and sweeping-droplet drainage is entirely suppressed. As described earlier, flank droplets form first and are fed directly by the grooves. These elongated droplets are strongly stabilized by capillary anchoring: the dense network of grooves resists dewetting and holds them in place despite their large volume. In turn, these stable flank droplets act as boundaries for the hanging ones below, maintaining both their position and rhythm.

When spacing increases to $s = 0.50\,\mathrm{mm}$, the groove density decreases but remains sufficient to prevent sweeping droplets from forming. Water still arrives exclusively through the grooves, yet the anchoring weakens because each droplet now spans fewer grooves. As a result, flank droplets become smaller and more circular. Since

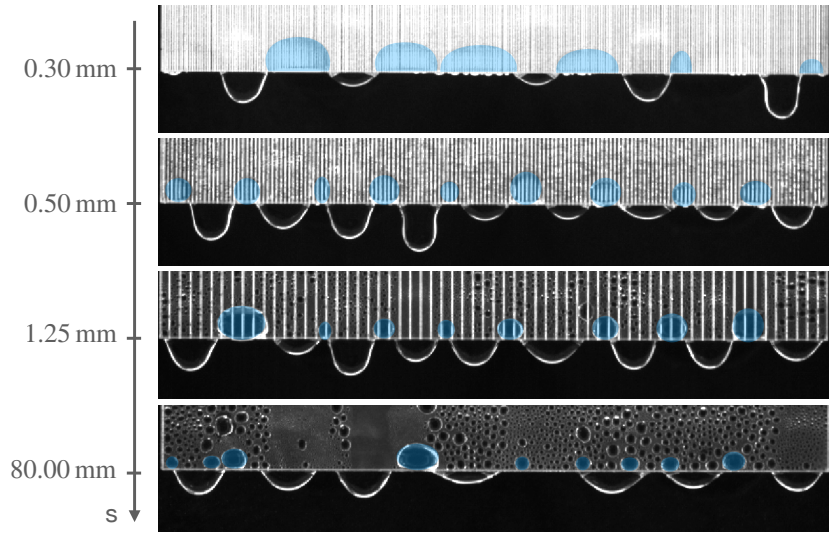

Figure 4.5: Snapshot of the bottom of the sample at $t = 2500\,\mathrm{s}$ for increasing groove spacing: $s = 0.30 - 0.50 - 1.25 - 80.00\,\mathrm{mm}$. Side-anchored (flank) droplets are highlighted in blue to aid visualization. As groove spacing increases, droplet organization evolves from an alternating arrangement of hanging and flank droplets to random deposition on the smooth substrate, reflecting the disappearance of groove-mediated capillary-driven drainage.

the lower boundary is entirely occupied, either by flank droplets or by hanging ones, any reduction in flank coverage leaves room for new hanging droplets to form. In other words, weakening the anchoring of flank droplets directly promotes the appearance of hanging ones. This explains the rising branch of the $N_d(s)$ curve for $s < 1\,\mathrm{mm}$ in Figure 4.3.

At $s = 1.25\,\mathrm{mm}$, groove anchoring weakens further, and gravitational drainage starts to compete again. Water now reaches the bottom edge intermittently, sometimes through grooves, sometimes through occasional sweeping droplets. Because the grooves are farther apart, each drainage event delivers larger, more sudden volumes of liquid. These abrupt inflows destabilize the flank droplets, which may either detach to form new hanging droplets or be swept away entirely. As a result, flank droplets lose their stabilizing role, and the dripping pattern becomes irregular. This transitional behavior near $s \approx R_c$ marks the point where gravity begins to overpower capillary organization.

On the smooth surface ($s = 80.00\,\mathrm{mm}$), no grooves remain, and capillary anchoring disappears entirely. Drainage is now dominated by fast sweeping droplets descending at about $100\,\mathrm{mm/s}$. Flank droplets can still form transiently at the corner, resting on the geometric discontinuity of the edge. Still, they are short-lived, with width $\leq \lambda$ and easily dislodged by the impact of descending droplets. The two populations, flank and hanging droplets, are thus completely decoupled and often appear superposed in the same region of the sample. Yet, despite this apparent disorder, the position of hanging droplets persist. Their stability is striking: rather than being torn away by the sweeping droplets, they merely fluctuate in position and size. This resilience originates from surface tension, which remains comparable

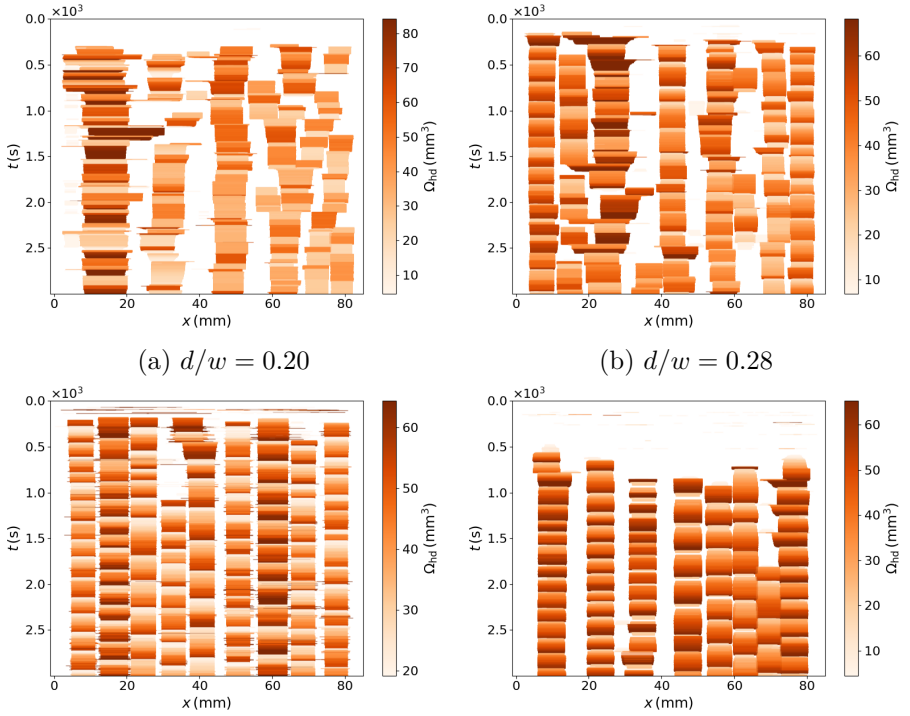

(a) $d/w = 0.20$ (b) $d/w = 0.28$

(c) $d/w = 0.95$ (d) $d/w = 3.01$

Figure 4.6: Spatio-temporal evolution of hanging droplets below the lower edge for increasing groove aspect ratio at fixed spacing $s = 0.5\,\mathrm{mm}$: (a) $d/w = 0.20$, (b) 0.28, (c) 0.95, and (d) 3.12. Each bar represents a droplet; its length corresponds to the droplet's width, and its color corresponds to the droplet's volume. As grooves deepen, the dynamics follow the same progression observed when decreasing spacing in Figure 4.2: Shallow grooves ($d/w < 0.3$) yield sparse, irregular dripping dominated by gravity, whereas deep grooves ($d/w > 1$) promote capillary confinement and produce regular, quasi-periodic dripping. The transition illustrates how increasing groove depth enhances anchoring strength, shifting the system from a gravity-driven to a capillary-organized regime.

to the inertial force of impacting droplets. A simple estimate of the Weber number

$$We = \frac{\rho r v^2}{\sigma} \approx 0.5 \tag{4.3}$$

confirms it. When a sweeping droplet hits a hanging one, it removes part of the volume of the hanging droplet, but not the whole droplet. In many cases, the reverse happens: the hanging droplet pulls the sweeping one toward itself and absorbs it. As a result, hanging droplets maintain a relatively stable position over time, as seen in Figure 4.2. Their mean width, about 2λ, and spacing, about λ, define a gravity–capillarity equilibrium that arises even without grooves. This explains the descending branch of $N_d(s)$ for large s, where dripping is sparse, uncoordinated, and governed purely by the balance between inertia and surface tension.

So far, we have varied the anchor density by changing the groove spacing. We now turn to their strength: each groove's geometry, through its depth and width, determines its ability to hold or release water, and, in turn, reshapes the dynamics

of dripping. To investigate this effect, we compare grooves of increasing aspect ratio d/w: 0.20 ($d = 28\,\mu$m, $w = 140\,\mu$m), 0.28 ($d = 58\,\mu$m, $w = 210\,\mu$m), 0.95 ($d = 204\,\mu$m, $w = 215\,\mu$m), and 3.01 ($d = 783\,\mu$m, $w = 260\,\mu$m).

The spatio-temporal patterns obtained when varying the groove aspect ratio (Figure 4.6) mirror those observed for spacing (Figure 4.2). Shallow grooves behave similarly to sparsely spaced ones: they provide weak anchorage while promoting sweep droplets, resulting in irregular, gravity-dominated dripping. Deep grooves, by contrast, act like closely packed ones, strengthening capillary anchors and suppressing gravitational drainage. It results in stable and periodic dripping. In both cases, the system moves through the same sequence of regimes as the balance between capillarity and gravity shifts. Groove spacing thus controls the density of anchors, while aspect ratio sets their strength, two complementary parameters that together define the architecture of the dripping pattern.

4.5 Convergent grooves

We have demonstrated that parallel grooves can affect the geometry and dynamics of dripping, but not its precise location. In other words, grooves organize drainage, yet the dripping points remain statistically distributed along the lower edge. To localize the dripping more precisely, water must not only be guided downward through capillary flow, but also directed toward predetermined positions. This can be achieved by replacing the parallel pattern with a convergent one.

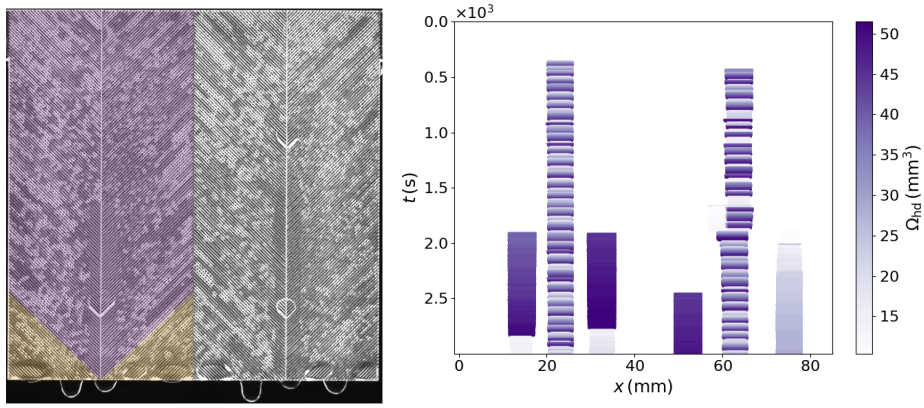

Figure 4.7: (a) Convergent groove pattern during steady condensation. One $40\,\mathrm{mm}$-wide pattern (highlighted in purple) is repeated twice across the $80\,\mathrm{mm}$ substrate. Each unit features a central vertical groove and multiple secondary grooves inclined at $45°$ and spaced by $0.50\,\mathrm{mm}$, converging toward the center. The two convergent basins collect water from both sides and channel it into the vertical grooves at $x = 20$ and $60\,\mathrm{mm}$. Triangular regions at the base of each pattern (highlighted in yellow) remain unconnected to the main basin. (b) Spatio-temporal diagram of hanging droplets below the convergent substrate. Two dominant vertical bands correspond to the dripping points located beneath the vertical grooves. Rapid color oscillations indicate intense and periodic drainage cycles, while faint, slowly varying bands outside these regions correspond to peripheral droplets. Nearly all condensed water exits through the two central outlets, demonstrating precise localization of dripping.

Figure 4.7(a) shows a convergent groove pattern composed of repeating 40 mm-

wide units (one highlighted in purple for clarity). The substrate, 80 mm wide, therefore contains two such units. Each pattern consists of a central vertical groove flanked by multiple secondary grooves inclined at 45°, spaced by 0.50 mm and of aspect ratio $d/w = 0.53$ ($d = 138\,\mu$m and $w = 260\,\mu$m) which ensures efficient capillary drainage. On each side, the inclined grooves converge toward the central one, of the same geometry as the secondary ones, forming two drainage basins centered at $x = 20$ and 60 mm.

Within each basin, condensed water first joins one of the inclined grooves, which channels it toward the central vertical groove. There, the accumulated flow sometimes exceeds the drainage capacity, producing droplets astride the central groove, visible in the picture. As a result, water reaches the bottom edge in two ways: continuously through the groove channels, and intermittently via these overflowing droplets. In both cases, the flow converges to a single point on the edge. The position of dripping is thus no longer determined by random breakups of flank droplets, but by the imposed groove geometry itself.

Outside the main basins, the inclined grooves leave two small triangular regions at the base of each pattern, unconnected to the vertical groove (highlighted in yellow in Figure 4.7(a)). Water condensing in these peripheral areas is directed straight to the lower edge, where it accumulates as small flank droplets that can occasionally evolve into hanging ones. However, because these regions collect only a minor fraction of the total condensed water, the resulting droplets grow very slowly and contribute little to the overall drainage.

The spatio-temporal diagram in Figure 4.7(b) confirms the effectiveness of the convergent design. Two dominant bands appear, each corresponding to one vertical groove. These bands exhibit rapid, regular color oscillations, reflecting high-frequency filling and discharge cycles, and remain fixed in position within one capillary length (λ) of the groove axis. A few secondary bands also appear outside these main regions, but their color variations are much slower, indicating that the associated droplets evolve weakly. These correspond to the peripheral zones described earlier. Thus, while isolated droplets may still appear elsewhere, nearly all the condensed water is channeled to the two main outlets. The dripping is fully localized.

Finally, we examine how the size of the convergent basin influences the duration of the dripping period. Figure 4.8(a) shows the average dripping period and the position of the active bands for three different basin widths: 40, 20, and 10 mm (one experiment shown per configuration). We extract the data from the stable dripping bands identified in the spatio-temporal diagrams. Within a given pattern, all basins display nearly identical dripping periods. Higher median values and occasional large error bars stem from the 1 fps acquisition rate, which can miss fast dripping events. This effect is most pronounced in the central region ($x \in [20, 60]$ mm), where the condensation rate may be slightly higher than near the edges due to the geometry of the experimental setup. The number of active dripping sources directly matches the number of basins, and their positions coincide, within $\ell/2$, with the vertical grooves that define each basin.

Figure 4.8(b) plots the mean dripping period τ as a function of basin width b on a log–log scale. The data reveal a clear inverse relationship: narrower basins collect less water and therefore produce longer dripping periods. To rationalize this trend, we consider the time τ required for condensation to generate the mass m_{hd} of a single hanging droplet ready to detach. The effective condensing area S of one

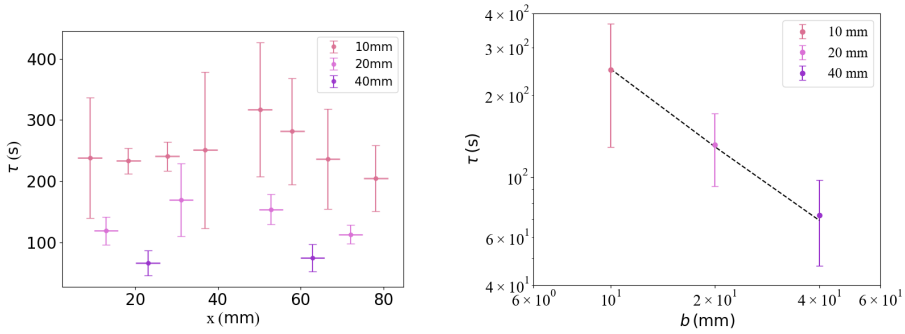

Figure 4.8: (a) Average dripping period and position of the active bands for three basin widths (40, 20, and 10 mm). Each point corresponds to a stable dripping source identified in the spatio-temporal diagrams. The number and position of active sources match the vertical grooves defining each basin, within mean droplet width ℓ which is indicated by the horizontal line. (b) Mean dripping period τ as a function of basin width b plotted on a log–log scale. The data show an inverse relationship: narrower basins collect less water and thus experience longer dripping periods. The black dotted line shows the prediction of the simple condensation–capillarity model (Equation 4.6). The agreement confirms that each basin behaves as a capillary attractor, with its geometry determining the frequency of water release.

basin, of width b and height L, excluding the triangular regions at its base, is

$$S = b(L - b/4). \tag{4.4}$$

Given a measured condensation rate $c = 0.208\,\mathrm{g\,s^{-1}\,m^{-2}}$, the total accumulated mass over time τ is $m_{hd} = cS\tau$. We estimate the characteristic droplet mass through a capillary–gravity balance,

$$m_{hd} = \frac{2(\ell + e)\sigma}{g}, \tag{4.5}$$

where ℓ and e denote the droplet width and substrate thickness, respectively. Equating both expressions yields the expected dripping period,

$$\tau = \alpha \, \frac{m_{hd}}{c\, b(L - b/4)}, \tag{4.6}$$

where $\alpha = 0.25$ is an empirical prefactor. On the one hand, this factor accounts for the fact that only a fraction of each hanging droplet's mass actually detaches during each cycle. On the other hand, it reconciles the discrepancy between the simple capillary–gravity mass estimation of $m \approx 0.15\,\mathrm{g}$ and the measured droplet mass of $m \approx 0.05\,\mathrm{g}$ obtained using a balance placed beneath the condensing plate. We plot the corresponding model in Figure 4.8(b) as a black dotted line.

Convergent grooves, therefore, provide a robust and straightforward strategy to control not only the geometry of dripping but also its position and frequency. By defining the geometry of the drainage basins, one can dictate both where water leaves the substrate and how often it does so.

4.6 Future work

The present work shows that groove geometry can both organize dripping and localize it, but the patterns explored so far still leave room for optimization. A first

natural extension is to refine convergent designs in order to eliminate peripheral zones. In the current patterns, small triangular regions at the base of each basin are not connected to the main drainage channel and therefore host slow filling droplets. One could redesign the texture so that all grooves, including those near the edges of the basin, ultimately converge toward the central vertical groove. Comparing the resulting spatio-temporal diagrams with those of the present chapter would test how completely one can suppress peripheral retention and concentrate all drainage into a prescribed set of outlets.

A second direction is to quantify groove anchoring more systematically by isolating and controlling geometric discontinuities. In the current configuration, flank droplets feel both the groove termination and the plate's lower edge. One could stop the grooves a controlled distance above the edge so that only one discontinuity, the groove termination, remains. This would allow direct measurement of the pinning strength associated solely with the groove, for instance, through the maximum puddle width and height sustained before breakup. More generally, a systematic exploration of groove spacing and aspect ratio could quantify their effect on puddle formation and destabilization. Varying the lateral arrangement of grooves would then test whether one can not only set the size of the puddles, but also trigger specific fragmentation patterns and, in the limit, program the dripping pattern through the array geometry.

A third important control parameter is surface wettability. In this chapter, the substrate was moderately hydrophilic, yielding sweeping droplets with an intermediate Weber number. Moving to superhydrophobic substrates would result in faster droplets, potentially destroying the spatio-temporal stability observed on the smooth plate. At the other extreme, superhydrophilic substrates would favor extended films and extremely robust puddles that are hard to destabilize. Exploring these two limits would test how far geometric control can compensate for or amplify the influence of wettability and help disentangle the respective roles of chemical and topographic patterning in setting dripping dynamics.

Finally, it is worth looking at the horizontal lower edge, where droplets hang and grow before detaching. Surprisingly, this configuration has received little attention in the literature [165], apart from the related case of droplets suspended from fibers [17, 88]. Yet an edge differs from a fiber in one key way. It introduces corners, which can pin the contact line and enhance stability. This immediately raises a first question. How does the maximum mass of a suspended droplet depend on the edge thickness and on the angles that bound the horizontal surface? The next question follows naturally in the context of this thesis. How would this detachment threshold change if the edge were textured, with grooves parallel to the long edge for example? In our setup, now that we are well aware that liquid transfer occurs within grooves, how would texture reshape the organization of hanging droplets, in particular their size and spacing?

4.7 Summary

This chapter demonstrates that the groove texturing governs not only the drainage of condensed water along a vertical substrate but also its detachment at the lower edge. By combining controlled condensation with high-resolution imaging, we identified how groove spacing, depth, and orientation dictate the emergence,

stability, and coordination of hanging droplets.

When grooves are widely spaced, sweep droplet impacts dominate drainage, leading to sudden and irregular dripping. As spacing decreases or grooves deepen, capillary forces at the groove edges stabilize flank droplets that feed the hanging ones below, transforming random dripping into a periodic and organized regime. The groove spacing thus sets the density of pinning sites, while the aspect ratio tunes their strength. Finally, convergent groove patterns enable complete control over the dripping position and frequency, turning the lower edge into an engineered array of capillary outlets.

The next chapter builds on this insight by isolating the mechanism behind groove-guided release. In the present work, dripping arose from the interplay of two geometric discontinuities, the groove termination and the substrate edge. This naturally raises the question of what happens when only one discontinuity remains, a groove that simply ends. To explore this, we turn to an even simpler configuration in which water is not supplied by condensation but injected in a controlled manner from a syringe.

5

Stretching water between two grooves

5.1 Motivation

Controlling how water spreads, drains, or accumulates on surfaces is crucial for applications ranging from passive atmospheric water harvesting [113, 105, 137] and heat exchanger design [5, 174] to antifogging and surface cleaning [175, 176, 177, 178]. In many of these systems, thin water films are the most desirable morphology: they offer continuous coverage, maximize surface–volume ratio, and enhance drainage or heat transfer [9]. Yet maintaining such films, especially on vertical or inclined substrates, remains a persistent challenge in fluid physics and surface engineering [179, 180].

Pure water, with its high surface tension, naturally retracts into droplets or rivulets on most surfaces. Creating and sustaining thin films typically demands extreme wettability, achieved through nano-scale roughness or chemical coatings [33, 181]. These approaches, while effective, often suffer from fragility, limited durability, and fabrication complexity, particularly when applied over large areas. As a result, there remains no robust, scalable method to stabilise thin films without resorting to complex surface treatments. Could a simple and purely geometric strategy overcome this limitation?

Imagine a stretched elastic sheet: when you let go of its sides, it snaps back. A water film behaves similarly, unless it is somehow laterally anchored. This chapter explores whether a minimal geometric feature, such as a pair of parallel grooves, could provide the necessary anchoring to stretch and maintain a stable film of pure water on an otherwise untreated vertical surface.

5.2 Material and methods

To explore this idea, we designed a minimal and robust experimental setup represented in Figure 5.1(a). The substrate is a transparent acrylic plate (TroGlass

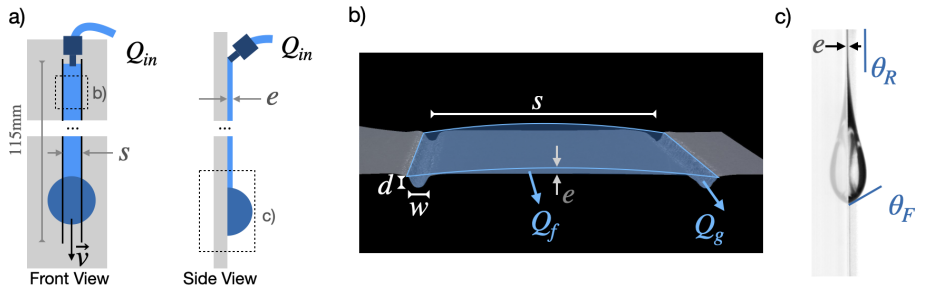

Figure 5.1: Experimental setup and groove geometry. (a) Front and side views of the acrylic substrate (TroGlass Clear, 3 mm thick) engraved with two vertical grooves spaced by a distance s. The grooves, 115 mm long, terminate a few centimeters above the bottom edge to trigger film rupture. A syringe pump delivers water between the grooves through a 0.8 mm nozzle at a flow rate Q_{in}. The side view illustrates how the thin film of thickness e connects the syringe tip to the droplet near the groove termination. (b) Groove geometry visualized using a Keyence VHX optical microscope. The three defining parameters are groove depth d, width w, and center-to-center spacing s. The example shown corresponds to a substrate with $s = 1.75$ mm and $d/w = 0.54$. Arrows illustrate the partitioning of the injected flow Q_{in} into a film contribution Q_{f} and groove contribution Q_{g}. (c) A droplet stretches vertically the lower end of the film as represented in 5.1 (c). This droplet is characterized by a front contact angle θ_F and the rear contact angle $\theta_R = 0$, given the continuous and smooth connection with the film.

Clear, 3 mm thick, colored in light gray) engraved with two vertical grooves using a CO_2 laser (Trotec Speedy 100). Each groove extends over 115 mm and terminates several centimeters above the lower edge, as represented in Figure 5.1 (a). The plates are moderately hydrophilic, with receding and advancing contact angles of $\theta_R = 48 \pm 4°$ and $\theta_A = 78 \pm 5°$, respectively, measured using the droplet inflation/deflation method on horizontal plates.

We define the groove geometry by three key parameters: the groove depth d, width w, and center-to-center spacing s, represented in Figure 5.1 (b). We studied three groove geometries with physical dimensions $(d, w) = (0.08, 0.15)$, $(0.21, 0.19)$, and $(0.38, 0.21)$ mm, corresponding to shallow ($d/w = 0.54$), intermediate (1.13), and deep (1.80) aspect ratios, respectively. The groove spacing s was varied independently from 0.75 to 2.25 mm. These dimensions were measured with a Keyence VHX optical microscope.

Water was injected between the upper grooves extremities through a 0.8 mm diameter nozzle connected to a syringe pump, with flow rates Q_{in} ranging from 0.33 to 10.00 mm^3/s. To ensure reproducibility, grooves were prewetted before each trial by sliding droplets along their length, either manually or by gravity. In some experiments, we added 0.01 g of Sodium Dodecyl Sulfate (SDS) per litre of water to reduce surface tension from $\sigma_{\text{water}} = 72$ mN/m to $\sigma_{\text{SDS}} = 63$ mN/m.

To estimate film thickness, we used particle tracking velocimetry (PTV). 20 μm tracer particles were suspended in the water and imaged using a high-resolution charged coupled device (CCD) camera at 113 fps. The field of view spanned a 25 mm segment centered within the grooved region. Velocity fields were extracted by subdividing the film into rectangular bins and averaging particle velocities within each region.

To track film destabilization at lower groove ends, we used a second CCD camera (13.6 fps) placed behind the substrate, with front lighting to enhance the droplet edges. We also captured additional side-view recordings at 300 fps. Each experiment

was repeated three times, with careful cleaning (isopropanol and deionized water) between trials.

5.3 Flow regimes

Because this system introduces new dynamics, we first describe how the fluid interacts with the substrate, which is initially smooth and then grooved, for different flow rates Q_{in}. This overview, summarized in Figure 5.2, highlights the richness of behaviors that emerge. Thin fluid layers are difficult to visualise directly, so we placed a checkered pattern between the light source and the substrate. Pattern deformation by refraction provides a qualitative view of the film: compressed pattern regions indicate greater interface curvature and correspond to a thicker fluid layer.

5.3.1 Smooth substrate

Injecting water onto a smooth vertical surface results in two stable morphologies: droplets at low flow rates and rivulets at high ones, illustrated in purple in Figure 5.2 (a) and (f). At low flow rates, the liquid forms a droplet pinned by contact angle hysteresis between the plate and the syringe tip. As the droplet grows under the continuous inflow, its weight eventually overcomes this capillary resistance and the droplet starts to slide. [14, 44, 45]. The droplet shape reflects its velocity: slow-moving droplets maintain an oval profile, while faster ones develop a rear corner or even a sharp cusp.

As the flow rate increases further, this sequence of individual droplets gives way to a continuous stream, a rivulet. This transition is energetically favorable as a connected stream reduces the total interfacial energy [48]. Initially, the rivulet flows straight along the direction of gravity, stabilized by surface tension and contact line pinning. At even higher flow rates, however, inertial effects and local disturbances can destabilize the thread, leading to meandering. These two morphologies, droplets and rivulets, define the full range of stable behaviors accessible on a smooth vertical substrate. On our substrate, the transition between these two morphologies is at a flow rate about $Q_{\text{in}} \approx 80\,\text{mm}^3/\text{s}$. A schematic diagram shows a cross-section of the system at the colored line in the Figure 5.2.

5.3.2 Two vertical grooves

We now consider substrates patterned with a pair of vertical grooves, represented by orange schematics in Figure 5.2. To appreciate order of magnitude, we will consider the sample whose groove aspect ratio is $d/w = 1.80$, corresponding to the most significant groove cross-section.

First, we apply a low flow rate $Q_{\text{in}} \in [0.33, 1.66]\ \text{mm}^3/\text{s}$. When the grooves are dry, they act as barriers that constrain the droplet footprint. The base of the droplet has a width equal to the spacing s between the grooves, as illustrated on the schematic of Figure 5.2 (b). As the droplet exits the grooved zone, its footprint relaxes and it slows down. This deceleration is consistent with what is observed for droplets on vertical strips, an analogous system, since dry grooves behave like geometric boundaries. In such systems, droplet velocity is inversely proportional to

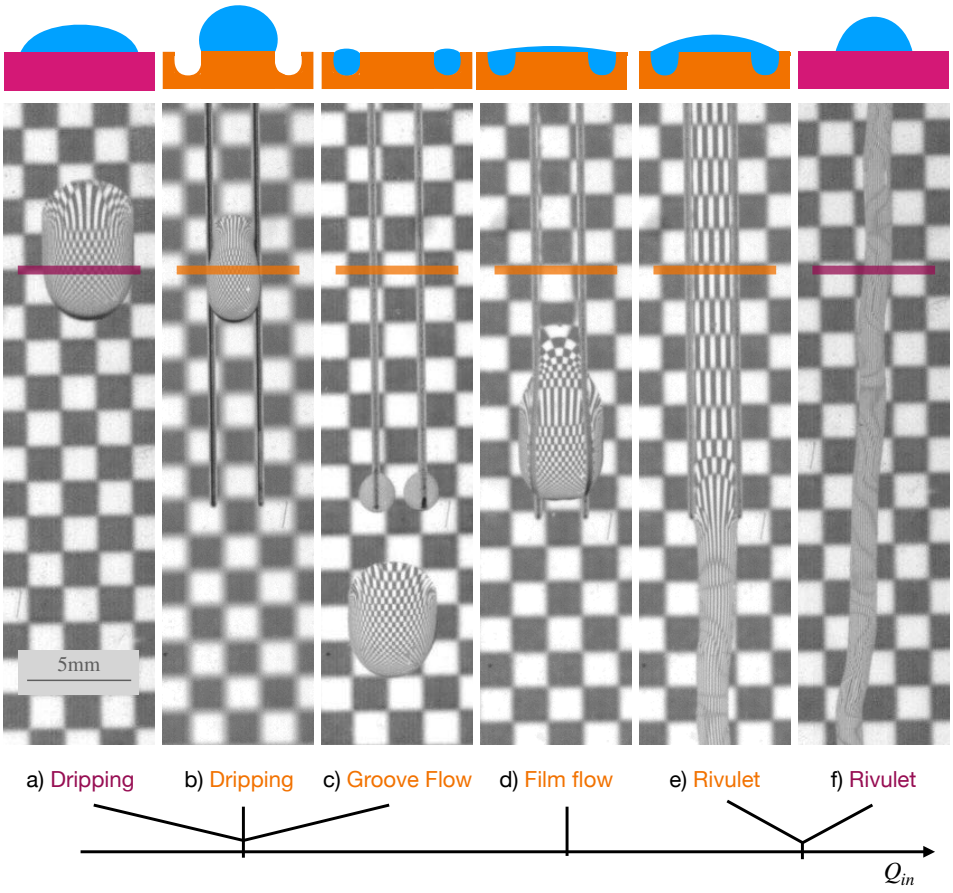

Figure 5.2: Sequence of flow regimes observed on vertical substrates as a function of flow rate Q_{in}. Each image displays the fluid morphology for increasing Q_{in}, with a checkered background that reveals film thickness via refraction: compressed patterns indicate higher curvature and thicker liquid layers. Schematics above each image illustrate the fluid cross-section at the location marked by the colored line in the corresponding photo. Smooth surfaces are shaded purple, and grooved cross-sections are shaded orange. At low flow rate on a smooth substrate, droplets form and slide once their weight overcomes contact angle hysteresis (a). At high flow rates, these droplets merge into a rivulet that eventually meanders due to inertial effects (f). On grooved substrates, new regimes emerge. When grooves are dry, they confine droplet width and do not transport liquid (b). Once wet, the same Q_{in} yields Groove Flow, where a puddle at the syringe tip feeds the grooves and generate droplets at groove lower extremities (c). At a higher flow rate, a stabilized film stretches between the grooves and periodically ruptures at their termination, releasing a droplet, and initiating the Film Flow regime (d). At very high flow, successive emitted droplets merge into a rivulet. This rivulet, first anchored by the grooves, follows a straight path. Then, once unconstrained, tight into a smaller flow with an increased thickness (e).

strip width [116]. Therefore, even when dry, the grooves already influence droplet dynamics.

Once the grooves are wet by sliding droplets along them, injecting the same flow rate as before yields a different behavior. Instead of dripping from the syringe tip, we observe a small and stable puddle at the syringe–groove junction. This connecting puddle bridges the syringe tip to both groove and has a constant volume. No water is visible elsewhere on the whole inter-groove region, meaning that water is entirely transported through the grooves. At the lower end of the substrate, two small droplets emerge, one per groove, and gradually grow until they merge and detach as a single droplet, visible in Figure 5.2(c). Immediately after detachment, two new droplets begin to form at the groove tips, initiating the cycle again. This dripping is decoupled from the syringe tip properties or position and relies only on groove characteristics. The grooves thus transition from constraints (when dry) to fluid conveyors, with the connecting puddle acting as a fluid junction. We refer to this regime as Groove Flow.

As the flow rate increases further, with $Q_{\text{in}} \in [1.66, 3.33]\,\text{mm}^3/\text{s}$, the connecting puddle, previously stationary, begins to swell. Once it grows large enough, it slides down the grooves, leaving behind a new connecting puddle. The sliding puddle, once at groove termini, collides with and entrains the droplets already present at the lower ends. However, even during the puddle swelling and sliding, droplets continue to form at the lower groove extremities. Consequently, the imposed flow rate Q_{in} is partitioned into two: one through the grooves and another into the connecting puddle. The flow rate threshold at which the connecting puddle begins to swell depends on groove geometry. Intuitively, the larger the groove cross-section, the more liquid it can transport before reaching saturation.

When the input flow rate approaches $Q_{\text{in}} \approx 3\,\text{mm}^3/\text{s}$, the dynamics shift once again. Occasionally, the sliding puddle leaves behind a thin liquid sheet confined between the syringe tip, the grooves and itself. At first, this film is unstable and ruptures quickly. But with increasing flow rate, the sheet stretches further before breaking. Eventually, we reach a critical threshold where the film stabilizes along the entire groove length. We performed successful experiments with grooves length over 250 mm. This continuous sheet is represented in the schematic of Figure 5.2 (d).

This stabilized film marks the onset of the third regime, the Film Flow regime, observed for $Q_{\text{in}} \in [3.33, 80.00]\,\text{mm}^3/\text{s}$ (Figure 5.2 (d)). In this state, a connecting puddle transforms into a sliding one, leaving behind a continuous film. Importantly, this film connects the sliding puddle to the syringe pump. Hence, the film prevents further puddle swelling at the top by feeding directly the sliding puddle. Once the rear of the sliding puddle exits the grooved zone, the film loses its lateral confinement and breaks. Remarkably, this breakup does not occur chaotically: the sheet retracts upward. Because water continues to flow in, the film does not fully collapse up to the syringe tip. Instead, it retracts until a new puddle forms at a height $H_{\max}$, where gravitational weight balances surface tension. The system then enters a repeatable cycle, illustrated in Figure 5.3 for $s = 2.25\,\text{mm}$, $d/w = 1.8$ and $Q_{\text{in}} = 3.33\,\text{mm}^3/\text{s}$. We first see a rapid film retraction accompanied by a growing puddle in half a second. Then the puddle stops at $H_{\max}$ and further grows during 2.5 s. At that point, its weight overcomes capillary force and it begins to slide down for 5 s. Ultimately, the rear of the puddle reaches the end of the groove, leading to film breakup. What is striking in these figures is how imperceptible the film

appears behind the puddle: the checkered pattern is barely disturbed, giving the impression that no film is present at all. Yet the smooth connection between the puddle and the film, together with the full sequence of events, leaves no doubt. The film is indeed there, stretched at a thickness that borders on the undetectable to the naked eye.

Within this regime, we identify two behaviors. At lower flow rates ($Q_{\text{in}} \in [3.33, 10.00]\,\text{mm}^3/\text{s}$), the film repeatedly retracts and reforms, producing a well-defined cyclic instability governed by $H_{\max}$. At higher flow rates ($Q_{\text{in}} \in [10, 80]\,\text{mm}^3/\text{s}$), the retraction height progressively diminishes until it vanishes. In this limit, droplets form directly from the continuous film at the groove tips, resembling remote dripping, once again independent of syringe tip properties.

Finally, at very high flow rates, $Q_{\text{in}} > 80\,\text{mm}^3/\text{s}$, droplet emission becomes so rapid that individual drops no longer drip from the liquid sheet. Instead, they merge into a continuous rivulet. Comparing the pattern density between grooves in Figures 5.2 (d) and (e) reveals that increasing the flow rate also thickens the film. The transition toward rivulet for a grooved substrate occurs at a comparable flow rate to that on a smooth one, as shown in Figure 5.2(e) and (f). Yet the presence of grooves introduces a crucial difference. Within the grooved region, the rivulet remains perfectly linear, strictly aligned with the groove direction. The grooves act as lateral anchors, suppressing transverse capillary instabilities and enforcing a straight flow path, clearly visible in Figure 5.2 (e). Once the rivulet exits the structured zone, however, its cross-section narrows under the pull of surface tension, further demonstrating how the grooves sustain a broader and thinner film.

The present study focuses exclusively on this Film Flow regime. Specifically, we examine the flow range $Q_{\text{in}} \in [0.6, 6.7]$, where the film remains stable between the grooves and where an apparent film retraction characterizes the instability. Our goal is to study the morphology, stability, and retraction dynamics of the film in this regime.

5.4 Film thickness

We first examine the stable portion of the film and look at how the imposed flow rate Q_{in} impacts its thickness e. Understanding this link is crucial for two reasons. It enables us to predict and control film thickness directly from substrate geometry and flow conditions. Second, this thickness plays a role in the cyclic breakup of the film, happening at the lower groove extremities.

5.4.1 Results

Our goal is to quantify film thickness; however, direct optical techniques are poorly suited for our system. Interferometry loses resolution in the 50–100 μm range, while profilometry requires reflectivity or scattering contrast, which transparent water films on acrylic lack. Instead, we use Particle Tracking Velocimetry (PTV), a robust and non-invasive method. By measuring internal velocity fields and applying a Stokes-flow model, we infer thickness indirectly yet reliably.

Figure 5.4 summaries the velocity field measured within the stabilized film. In a typical flow illustrated in Figure 5.4 (a), tracers concentrate near the film center, indicating faster motion in this region. The reconstructed velocity profiles,

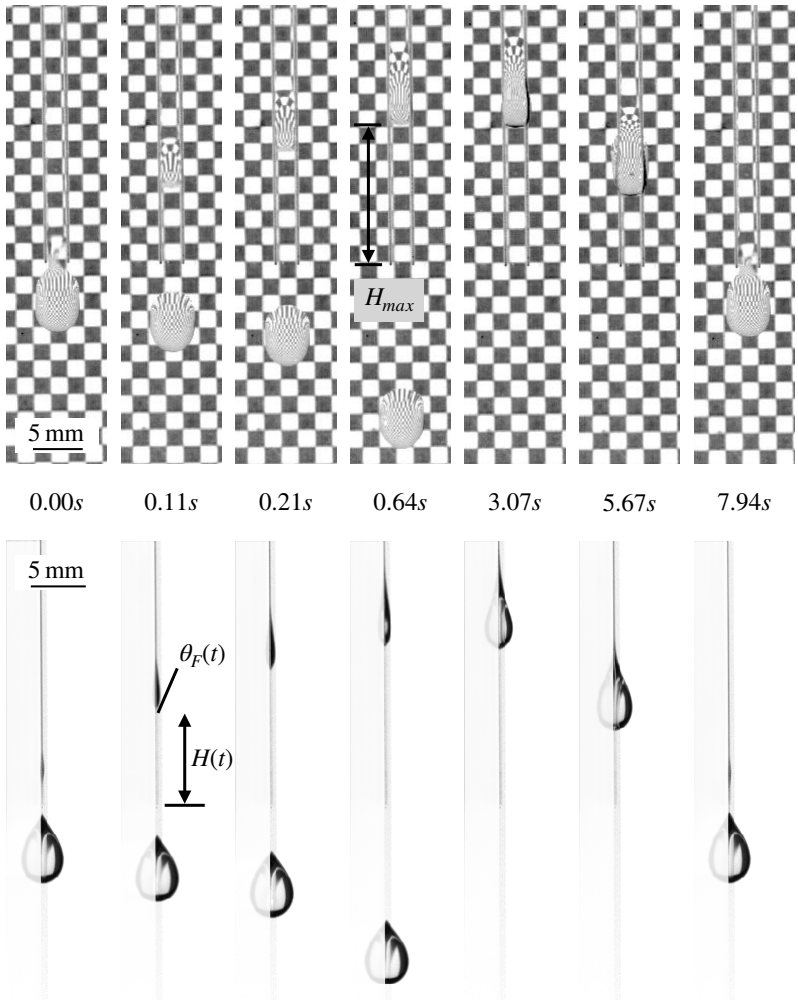

Figure 5.3: Cyclic dynamics of film rupture and droplet release in the stabilized film regime. Top and bottom rows show synchronized front and side views of the same experiment: groove spacing of $s = 2.25\,\mathrm{mm}$, an aspect ratio $d/w = 1.80$, and an input flow rate of $Q_{\mathrm{in}} = 3.33\,\mathrm{mm}^3/\mathrm{s}$. (Top) A checkered pattern is placed between the backlight and the substrate to visualize film curvature via refraction: strong pattern deformation signals thicker fluid layers. Yet the film behind the droplet is nearly imperceptible; the pattern remains barely distorted, highlighting how thin the film is. As the droplet slides and crosses the groove termini, at $t = 0\,\mathrm{s}$, lateral confinement disappears and the film ruptures. The film retracts upward, forming at its base a new puddle that grows as the film pulls back. Retraction and early puddle growth occur within $0.64\,\mathrm{s}$. The puddle then pins at a stable retraction height H_{max}, where capillary forces balance its weight, and continues to inflate for another $2.5\,\mathrm{s}$ (until $t = 3.07\,\mathrm{s}$). Once the puddle becomes heavy enough, it depins and slides downward over approximately $5\,\mathrm{s}$. When the rear of the droplet reaches the end of the groove, the film ruptures again, restarting the cycle. (Bottom) Side view emphasizing puddle inflation and the evolution of the front contact angle θ_{F}, which increases steadily until the droplet detaches.

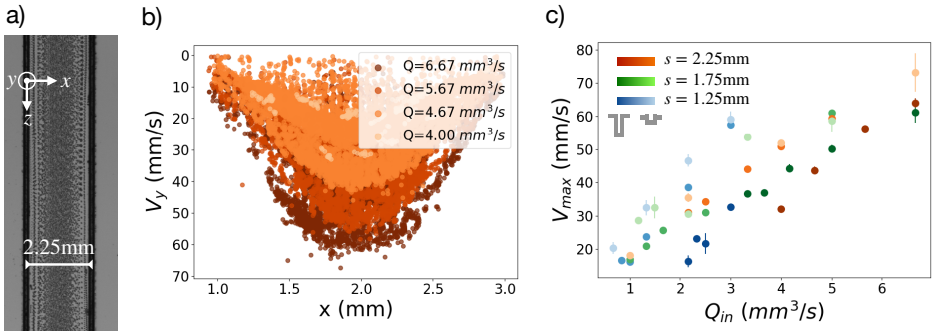

Figure 5.4: Film velocity measurements using particle tracking velocimetry (PTV). (a) Superposition of 2000 consecutive frames showing $20\,\mu$m tracer particles flowing through a thin film confined between two grooves spaced by $s = 2.25\,\text{mm}$ with $Q_{\text{in}} = 6.67\,\text{mm}^3/\text{s}$. Tracers cluster near the center, indicating faster flow in this region. (b) Reconstructed horizontal velocity profiles across the film, exhibiting a parabolic shape consistent with confined Stokes flow. The apparent "filled" profiles reflect the 3D nature of the flow: particles occupy different heights, resulting in multiple velocities being detected at each horizontal position. (c) Maximum velocity V_{max}, averaged from the 10 fastest particles, plotted as a function of Q_{in} for various groove spacings s and geometries d/w. Velocity increases with Q_{in} and reveals two trends: (i) at fixed groove geometry (same shade), smaller spacings (blue) yield higher V_{max} due to thicker films; (ii) at fixed spacing (same color), deeper grooves (darker tones) reduce V_{max}, consistent with flow being diverted into the grooves.

plotted in Figure 5.4(b), show a parabolic shape, with maximum speed at the center and slower flow near the edges, reflecting the confinement imposed by the groove boundaries. The apparent "filled" character of the profile arises from the three-dimensional nature of the flow: tracer particles are distributed across different heights within the film, so multiple velocities are detected at a given horizontal position. As the imposed flow rate Q_{in} increases, the maximum velocity within the film increases accordingly.

We then average the speed of the 10 fastest particles for various groove geometries and spacings and plotted them as a function of the imposed flow rate Q_{in} in Figure 5.4 (c). As expected, V_{max} increases with Q_{in}. Two additional trends emerge. First, at a given flow rate and fixed groove geometry (same shade), smaller spacings (blue points) yield higher velocities than larger ones (orange points). When the film is stretched across a wider spacing, its thickness decreases, which in turn reduces the maximum speed that can be sustained by the film. Second, at fixed spacing (same color), we observe that deeper grooves (darker tones) result in lower maximum velocities. This suggests that more fluid is diverted into the grooves, leaving less available to form the film, resulting in a thinner film and reduced flow speed.

5.4.2 Model

We now develop two complementary approaches to estimate the film thickness. The first method relies on velocity profiles extracted from PTV measurements, while the second predicts thickness based on the imposed flow rate and substrate geometry. Comparing both models allows us to validate the theoretical scaling and refine its predictive accuracy.

In the first approach, we assume that inertial effects are negligible ($\text{Re} < 10$), so the flow within the film can be described as a gravity-driven Stokes flow. The

motion of thin liquid films is primarily governed by viscous friction, which renders the lubrication approximation particularly suitable [146]. The balance between gravity and viscosity yields

$$\rho g = \eta \frac{d^2V}{dy^2}, \tag{5.1}$$

where $V(y)$ is the out of plane velocity, ρ the fluid density, η the dynamic viscosity, and y the height perpendicular to the substrate. Solving this equation with a no-slip condition at the substrate and a zero-shear condition at the air–liquid interface gives the velocity profile

$$V(y) = \frac{\rho g}{\eta}\left(ey - \frac{y^2}{2}\right), \tag{5.2}$$

where e denotes the film thickness. The maximum velocity occurs at the free surface, $y = e$, leading to:

$$V_{\max} = \frac{\rho g e^2}{2\eta}. \tag{5.3}$$

This relation provides a way to estimate the film thickness from the measured peak velocity

$$e_{\mathrm{PTV}} = \sqrt{\frac{2\eta V_{\max}}{\rho g}}. \tag{5.4}$$

We want to build a predictive model based solely on the imposed flow rate as it is the easiest variable to adjust in real conditions. To do so, we consider the total input flow rate as a combination of flow through the film and through the grooves

$$Q_{\mathrm{in}} = Q_f + 2Q_g, \tag{5.5}$$

where Q_f is the flow rate through the film and $2Q_g$ represents the maximum flow that can be entirely transported through the grooves. This threshold $2Q_g$ value is determined experimentally in the Groove Flow regime by gradually increasing Q_{in} until a visible puddle begins to grow at the syringe–groove junction. We find that $2Q_g$ depends on groove geometry: for shallow grooves ($d/w = 0.54$), $2Q_g = 0.08 \pm 0.02\,\mathrm{mm}^3/\mathrm{s}$; for intermediate grooves ($d/w = 1.13$), $2Q_g = 0.42 \pm 0.05\,\mathrm{mm}^3/\mathrm{s}$; and for deep grooves ($d/w = 1.80$), $2Q_g = 1.67 \pm 0.17\,\mathrm{mm}^3/\mathrm{s}$.

We then express the film flow rate as

$$Q_f = es\widetilde{V}, \tag{5.6}$$

with $\widetilde{V}$ the mean velocity in the film, assuming uniform thickness. We get this mean velocity by integrating Equation(5.2) over the film thickness

$$\widetilde{V} = \rho g e^2/3\eta. \tag{5.7}$$

We substitute this result into the expression of Q_f such as thickness is expressed in term controllable parameters

$$e_{\mathrm{flow}} = \left(\frac{3\eta(Q_{\mathrm{in}} - 2Q_g)}{\rho g s}\right)^{1/3}. \tag{5.8}$$

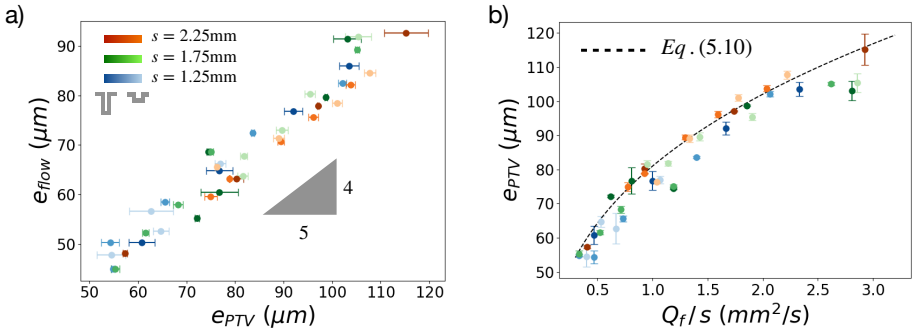

Figure 5.5: Film thickness measurements and model validation. (a) Comparison between experimental film thickness e_{PTV}, inferred from particle tracking velocimetry (Equation (5.4)), and the theoretical prediction e_{flow} based on a uniform Stokes flow model (Equation 5.8). A systematic offset (slope $\xi = 4/5$) is attributed to the finite width of the film, which reduces the effective flow area. (b) Collapse of all measured film thicknesses e_{PTV} as a function of scaled film flow rate Q_f/s. This collapse confirms the model central assumption: once groove flow saturates, the remaining input is redirected entirely into the inter-groove film (Equation 5.5). The dashed line represents the predicted model (Equation 5.10), which is validated across various groove geometries and spacings.

A comparison between the experimental method e_{PTV} and theoretical one e_{flow} is presented in Figure 5.5 (a). While the predicted and measured values are strongly correlated, a systematic factor is observed. This is corrected by introducing an approximated prefactor $\xi = 4/5$, such that

$$e_{\mathrm{flow}} = \xi\, e_{\mathrm{PTV}}. \tag{5.9}$$

This correction accounts for model simplifications, such as the assumption of infinite film width. In reality, the film is confined between two grooves and exhibits curvature at the edges, which reduces the effective flow area. Incorporating this correction, the final expression for film thickness becomes

$$e = \frac{1}{\xi}\left(\frac{3\eta}{\rho g}\frac{Q_f}{s}\right)^{1/3}. \tag{5.10}$$

This final expression provides a compact relationship between film thickness, flow parameters and groove geometry. The measured maximum film thickness was consistently greater than 50 μm, whereas thin-film instability theory predicts a critical thickness on the order of 1μm [182]. This discrepancy can be understood by noting that our model assumes a uniform film thickness, while in reality the confined geometry imposes a parabolic profile. Consequently, the thickness near the edges can approach values comparable to the limit of the thin-film instability.

5.4.3 Discussion

Figure 5.5(b) compares the experimental film thickness e_{PTV} (Equation (5.4)) with the scaled film flow rate Q_{f}/s. Remarkably, data from all groove geometries and spacings collapse onto a single curve. This collapse supports the central assumption of the model: once groove flow saturates, the remaining input is entirely redirected into a stabilized inter-groove film (Equation (5.5)). The dashed line shows the

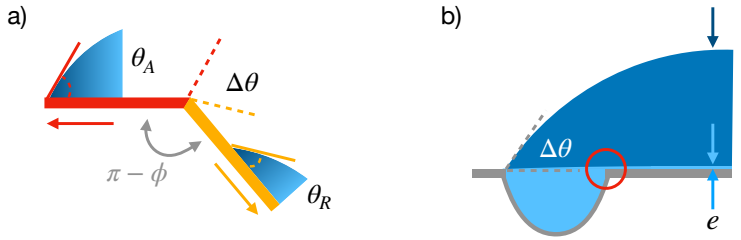

Figure 5.6: (a) Schematic showing how a corner enables the triple line to accommodate a range of contact angles $\Delta\theta$, enhancing pinning and film stability. (b) Vertical cross-section of the outer groove edge. Despite thinning at low Q_{in}, the film remains pinned as the contact angle stays within the hysteresis range (gray dashed lines). The red circle highlights a region of steep velocity gradients between film and groove flow, where small perturbations may trigger dewetting.

theoretical prediction e based on a adjusted Stokes flow model (Equation (5.10)). The strong agreement across conditions confirms the validity of the scaling and demonstrates that film thickness can be reliably inferred from the input flow rate and groove geometry alone. The resulting films can be extremely thin, down to 50 μm, despite being composed of pure water, without surfactants. Such thicknesses are typically unstable on smooth surfaces, yet here, they are robust and fully tunable via syringe flow rate alone.

Still, we note that no direct thickness measurements were made for reasons explained earlier. Our model assumes an ideal Stokes flow with uniform thickness. In reality, the flow cross-section is not rectangular but curved near the groove edges. This lateral curvature reduces the effective flow area, resulting in a slight overestimation of the average velocity in the model. As a result, the actual film thickness is likely even thinner than predicted, an outcome that further underscores the ability of grooves to support thin water films.

The next question is why the liquid film is stable. On a completely smooth surface, water films of similar thickness are prone to instabilities. Here, however, the film resists destabilization over surprisingly long distances. To understand this behavior, it is helpful to consider the role of edge pinning, illustrated by the corner shown in Figure 5.6(a).

Consider a droplet moving leftward along a red surface. To advance, its front contact angle must reach θ_{F}. Now imagine a droplet moving backward to the right on a yellow surface; its rear contact angle will take the value θ_{R}. Finally, suppose the droplet is located on the yellow surface with its contact line precisely at the corner where the yellow and red surfaces meet with an angle ϕ. For the droplet to advance onto the red surface, its front angle must match θ_{F}, and to recede on the yellow surface, its rear angle must match θ_{R}. Thus, when the triple line sits at the corner, it can remain pinned across a wide range of angles $\Delta\theta$, accommodating changes in droplet volume without moving. The total angular range allowed by the corner is given by $\Delta\theta = (\theta_{\text{A}} - \theta_{\text{R}}) + \phi$, where ϕ is the corner angle. A sharper corner extends this range, making pinning even more robust.

We can now interpret the film stability. As the flow rate increases, the film thickens according to Equation (5.10), and the contact angle at the film edge rises. As long as this angle remains within the contact angle hysteresis range $\Delta\theta$, the triple line stays pinned at the groove corner, and the film remains laterally confined.

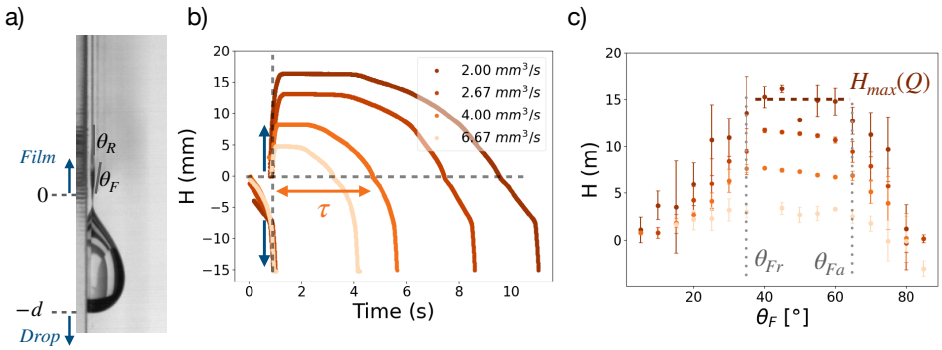

Figure 5.7: Cyclic dynamics of film retraction, puddle inflation, and droplet release. (a) Representative frame showing the start of a new cycle, triggered when the rear of the droplet passes the groove termination ($H = 0$). At this point, the film loses its lateral confinement, ruptures, and retracts upward. A new puddle forms at the rupture point and inflates as the film retracts. It is characterized by a front contact angle θ_{F} and a vanishing rear angle $\theta_{\mathrm{R}} = 0°$, due to the smooth connection with the film. (b) Time evolution of the puddle lower boundary $H(t)$ as a function of time, for various flow rates on the substrate $d/w = 1.80$ and $s = 2.25\,\mathrm{mm}$. All trajectories follow the same sequence: rapid retraction, a plateau during which the puddle inflates, sliding, and detachment. Kinks at $H = 0$ and $H = -d$ correspond to the passage of the front and rear across the groove termination. Lower Q_{in} leads to taller retractions and longer inflation times. The cycle period τ is defined as the time between two successive film ruptures; the following cycle is not shown. (c) Evolution of the front contact angle θ_{F} over one cycle. After rupture, θ_{F} increases with puddle growth until reaching the receding threshold $\theta_{\mathrm{Fr}} \approx 35°$, where the contact line pins. As the angle continues to increase, it reaches the critical threshold of around $65°$, at which point the droplet slides. Dashed lines indicate these thresholds. Only θ_{F} is measured; the rear angle is assumed to be $\theta_{\mathrm{R}} = 0°$ due to the smooth film connection.

Conversely, for an extremely thin film, the receding contact angle is very small. However, since the grooves remain filled in the Film Flow regime, the contact angle at the triple line never reaches the receding threshold θ_{R}, and depinning does not occur. As a result, the groove edge acts as a robust pinning site, enabling the film to remain stable over a wide range of thicknesses.

But what happens when the film finally destabilizes? In practice, this typically occurs at the film extremities, whether the syringe side or the puddle one. The precise mechanism remains difficult to capture, but a likely hypothesis involves the inner edges of the grooves as illustrated in Figure 5.6 (b) with a red circle. These locations concentrate velocity gradients between the film and the groove. A small perturbation, especially under low-flow conditions, may be sufficient to trigger dewetting from these points, initiating whole-film rupture.

5.5 Periodic film retraction

While grooves provide robust lateral pinning throughout the confined region, this stabilization is inherently local. At the downstream end, where the grooves terminate and lateral confinement abruptly vanishes, the film loses its geometric anchors. This discontinuity acts as a passive trigger for destabilization. We now turn to this stage, where the system enters a self-sustained cycle of puddle retraction, inflation, sliding, and finally detachment.

5.5.1 Cycle description

To characterize the cyclic dynamics in the stabilized film regime, we track the vertical motion of the droplet's lower boundary across flow rates Q_{in} (Figure 5.7(a–c)). The cycle begins when the rear of the droplet crosses the groove termination ($H = 0$ in Figures 5.3 & 5.7(a)). At this moment, the front continues its descent, while the thin connecting film ruptures and retracts upward. A puddle forms at the breaking point, marked by a low front angle θ_{F}, and initiates the next cycle.

Figure 5.7(b) details this process as a function of time. At $t = 0$, the front has already exited the grooves, while the rear remains connected by a thin film. When the rear reaches the groove end, the film breaks. Two paths then emerge: one traces the front as it slides downward, the other follows the upward retraction of the film. This retraction occurs in two stages: a rapid phase driven by surface tension, then a plateau where the retraction front pins and the puddle inflates, constantly fed by Q_{in}. Once the puddle is heavy enough, the lower contact line depins and sliding begins. The descent itself unfolds in stages. The droplet initially accelerates, then slows when the front reaches $H = 0$ (bottom of the grooves). It then moves at nearly constant velocity until the rear exits the grooves at $H = -d$, where the film break. This moment is marked by a renewed acceleration as the droplet isn't pulled up by the film anymore. Across flow rates, this sequence is preserved: lower Q_{in} produces taller, faster retractions and longer static inflation phases, while higher Q_{in} shortens the cycle. Once the droplet has fully exited, trajectories converge to a similar acceleration profile.

While these trajectories reveal when transitions occur, they do not explain what controls them. To answer that, we examine the front contact angle θ_{F} throughout the cycle (see Figure 5.7(c)). In the retraction phase, both front angle and height rise together until θ_{F} reaches about 35°. At this point, the puddle pins: its height freezes while θ_{F} keeps increasing as water accumulates. We define this threshold as θ_{Fr}, with r for "receding." The terminology echoes classical hysteresis tests, where a droplet recedes once its angle falls below a critical value. Here, the logic is inverted: below θ_{Fr} the line recedes, but once it reaches θ_{Fr} it abruptly pins. A second threshold appears near 65°, when the dynamics reverse. The contact angle continues to grow, but the puddle height decreases as the droplet begins to slide. We label this θ_{Fa}, with a for "advancing," mirroring classical inflation tests where motion starts at an advancing angle. Beyond this point, the droplet keeps gaining mass from the inflow and accelerates as it leaves the grooves, which pushes θ_{F} toward 90° at exit.

Despite large variations in Q_{in}, these thresholds are remarkably consistent. Retraction always halts at $\theta_{\text{Fr}} \approx 35°$, while sliding always starts at $\theta_{\text{Fa}} \approx 65°$. Both are slightly lower than advancing/receding values measured on smooth horizontal substrates. This discrepancy may reflect the influence of the grooves, either during retraction by confining the puddle or during descent by guiding the droplet. Together, θ_{Fr} and θ_{Fa} provide robust geometric markers that govern the puddle cycle.

5.5.2 Results

Figure 5.8(a) presents the experimentally measured retraction height H_{max} as a function of the film flow rate $Q_{\text{f}} = Q_{\text{in}} - 2Q_{\text{g}}$. Two key trends emerge. First, for

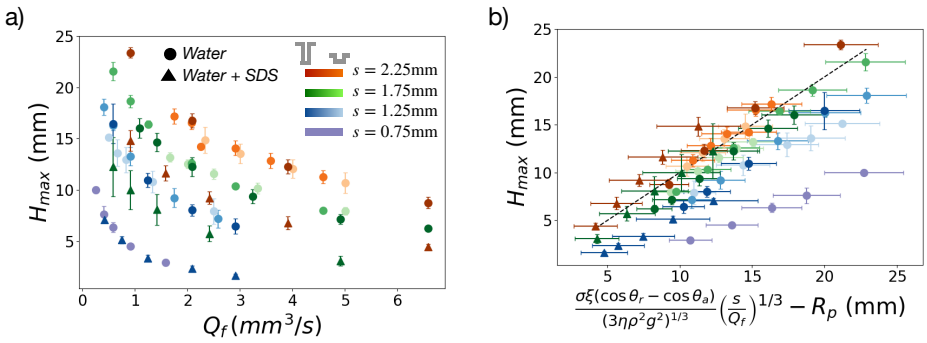

Figure 5.8: Retraction height as a function of film flow rate and model validation. (a) Experimental measurements of the maximum retraction height $H_{\max}$ as a function of film flow rate $Q_{\mathrm{f}} = Q_{\mathrm{in}} - 2Q_{\mathrm{g}}$. Each color represents a different groove spacing s; darker shades correspond to deeper grooves (larger d/w). Filled circles indicate pure water, while filled triangles correspond to SDS-added water (lower surface tension). Two trends emerge: increasing Q_{f} reduces $H_{\max}$, as thicker films reach weight–capillarity balance more quickly; meanwhile, increasing s increases $H_{\max}$, as wider films support stronger upward surface tension forces. SDS data (triangles) shift downward, consistent with a reduced surface tension lowering the capillary force required for balance. (b) Experimental data plotted as function of the model $H_{\max}$ based on a gravity–capillarity force balance (Equation (5.14)). The dashed line of slope 1 confirms the good agreement. However, at the smallest spacing $s = 0.75\,\mathrm{mm}$, the model over-predicts $H_{\max}$, likely because groove geometry begins to influence drainage and curvature, violating the flat-film assumption.

a fixed spacing s, the retraction height $H_{\max}$ decreases with increasing flow rate. Second, for a fixed Q_{f}, the retraction height increases with groove spacing. Finally, data for identical spacing s but different groove aspect ratios superimpose on one another. This supports the relevance of Q_{f} as a unifying parameter: once the grooves saturate, $Q_{\mathrm{in}} > 2Q_g$, any additional injected flow is routed through the film, and its effect on $H_{\max}$ depends only on the inter-groove flow Q_f. Importantly, experiments performed with SDS (filled triangles) show a systematic downward shift compared to pure water (filled circles). Since SDS lowers surface tension, this shift suggests that $H_{\max}$ is sensitive to capillary effects. Altogether, these observations suggest that $H_{\max}$ depends on both the weight of the accumulated water and the surface tension pulling it upward. In the next section, we develop a theoretical model to capture this behavior quantitatively.

5.5.3 Modelisation

At the end of the retraction phase, the puddle pins at its maximum height. We interpret this as the point where surface tension balances gravitational weight. The capillary force is approximated as

$$F_\sigma = \sigma s \left(\cos\theta_R - \cos\theta_F\right), \tag{5.11}$$

where σ is the surface tension, s the groove spacing, and θ_{R} (resp. θ_{F}) the puddle rear (resp. front) contact angles. We use $\theta_R = 0°$ to reflect the smooth rear connection with the film, and set $\theta_F = \theta_{\mathrm{Fr}}$, the front contact angle at the end of the retraction phase, measured experimentally. For water, we find $\theta_{\mathrm{Fr}} = 38.5° \pm 3°$; for SDS, $\theta_{\mathrm{Fr}} = 34° \pm 6°$. The opposing force arises from the mass of the puddle.

We assume that it corresponds to mass of the film over a length $H_{\max} + R_p$, with R_p denoting half the puddle height. This leads to the expression

$$F_g = \rho g e s (H_{\max} + R_p). \tag{5.12}$$

The puddle height remains approximately constant across experiments, with $2R_p = 7.0 \pm 0.4\,\text{mm}$. Equating the two forces yields

$$\sigma s\,(1 - \cos\theta_{\text{Fr}}) = \rho g e s\,(H_{\max} + R_p)\,. \tag{5.13}$$

To express the film thickness e in terms of controllable parameters, we insert Equation (5.10) (film thickness vs flow rate) into the force balance. This yields the final expression for the maximum retraction height:

$$H_{\max} = \frac{\sigma\xi\,(1 - \cos\theta_{\text{Fr}})}{(3\eta\rho^2 g^2)^{1/3}} \left(\frac{s}{Q_{\text{f}}}\right)^{1/3} - R_p. \tag{5.14}$$

This model predicts that retraction height $H_{\max}$ increases with groove spacing s and surface tension σ, and decreases with inter-groove flow rate Q_{f}.

5.5.4 Discussion

Figure 5.8(b) compares this theoretical prediction with the experimental data. The agreement is striking: across groove geometries, spacings, and fluid compositions, the data collapse onto a single straight line when plotted as a function of predictive model (Equation (5.14)). This collapse confirms that the retraction height $H_{\max}$ is primarily governed by a balance between gravity and capillarity. The model captures the observed trends: $H_{\max}$ decreases with increasing flow rate (via thicker films) and increases with groove spacing (via stronger capillary support). It also predicts the downward shift caused by the addition of SDS, reflecting reduced surface tension.

Despite its success, the model rests on several simplifying assumptions that begin to break down at the extremes. At the smallest groove spacing tested ($s = 0.75\,\text{mm}$), the model systematically over-predicts $H_{\max}$. As the groove width becomes comparable to that of the film, grooves may actively participate during retraction of the film. These effects alter the dynamic in ways not captured by our flat-film approximation. At the opposite extreme, our data approach but do not exceed the capillary length $\lambda = 2.67\,\text{mm}$, beyond which Plateau-Rayleigh instabilities are expected to appear. In this regime, continuous wetting becomes difficult to maintain, as the 0.8 mm diameter nozzle struggles to bridge wide groove spacings reliably.

Another limitation lies in the assumption of a static force balance. In practice, the puddle continues to grow as it retracts, accumulating additional fluid from Q_{in}. While this inflow is likely small compared to the final puddle mass, it introduces a temporal component that could subtly shift $H_{\max}$, especially if we consider higher input flow rates Q_{in}.

In summary, the model captures the essential physics driving the retraction height, a gravity–capillarity balance shaped by groove spacing, film thickness, and surface tension. Its success demonstrates that $H_{\max}$ provides a robust, experimentally accessible observable for probing thin-film dynamics. Yet at the limits of small

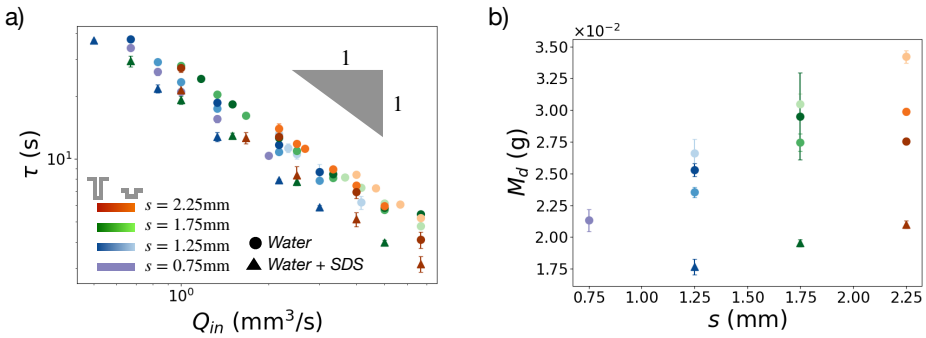

Figure 5.9: (a) Log-log plot of the average cycle duration τ as a function of imposed flow rate Q_{in}, compiled across groove geometries (d/w), spacings (s), and fluid compositions (pure water vs. SDS). Surfactant addition reduces τ across all conditions, while increasing groove spacing tends to delay detachment. (b) Corresponding droplet mass $M_d = \rho Q_{\text{in}} \tau$ as a function of groove spacing s. Wider groove spacing tends to produce larger droplets, while SDS reduces droplet mass across all spacings.

groove spacing and low surface tension fluid, we may take into account additional mechanisms. Such as groove–film coupling during film retraction, time-dependent puddle feeding, and film curvature on the lateral edges. These warrant further investigation in future work.

5.6 Droplet generation

We now turn to the droplet generation following each film rupture. We measure the time between successive film ruptures τ, and from this, infer the mass of the released droplet. The duration of one cycle τ is represented in Figure 5.7 (b) for one of the flow rates.

Figure 5.9(a) presents the average cycle duration τ as a function of the imposed flow rate Q_{in}, compiled across all experiments varying groove geometry (d/w), spacing (s), and fluid composition (pure water vs. SDS). All data align along parallel lines of slope -1 in a log–log plot, revealing a robust inverse relation

$$\tau \propto Q_{\text{in}}^{-1}. \tag{5.15}$$

This relationship confirms that the rate of mass accumulation governs the timescale of droplet formation: at lower flow rates, it takes longer to build a droplet large enough to detach. Here, unlike previous regimes where only the film flow rate Q_f mattered, the total input flow Q_{in} sets the pace, because the entire injected volume is redirected toward the droplet, which becomes the system sole sink.

Despite this scaling, secondary trends emerge. For pure water, increasing the groove spacing s leads to longer cycle durations. Conversely, SDS reduces τ across all spacings and geometries. As a consequence, τ is a function of both spacing s and surface tension σ. Assuming that all incoming flow contributes to droplet growth between ruptures, the droplet mass can be directly estimated as

$$M_d = \rho Q_{\text{in}} \tau(s, \sigma). \tag{5.16}$$

Figure 5.9(b) presents the measured droplet mass M_d as a function of groove spacing s. Larger spacings consistently yield heavier droplets, while the addition

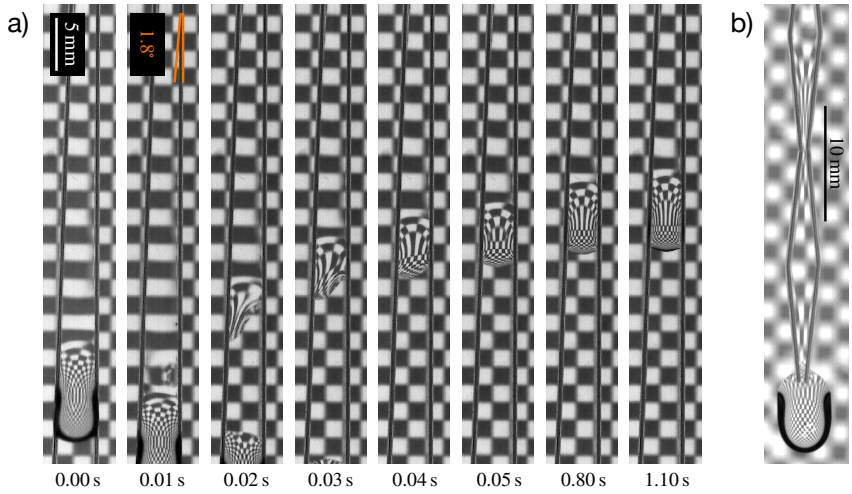

Figure 5.10: (a) Controlled retraction of a thin water film between divergent grooves (opening angle $1.8°$). Film rupture is triggered not by a geometric discontinuity but by lateral stretching beyond the stability limit ($s \approx 5\text{mm} \approx 2\lambda$). (b) Grooves with periodically varying spacing generate local modulations of film thickness: the film thickens at constrictions (necks) and thins at widened regions (bellies), as revealed by the deformation of the background pattern.

of SDS reduces it across all spacings. These observations suggest that droplet release arises again from a balance between gravity and capillarity. Wider groove spacings increase the film width, strengthening surface tension forces and delaying release. Lowering surface tension with SDS promotes earlier detachment. Both effects modulate the critical mass needed to initiate sliding and, therefore, set the final droplet mass.

In summary, this final stage completes the picture of the destabilization cycle. While Q_{in} controls the rhythm of droplet formation, groove spacing and surface tension fine-tune the release.

5.7 Future researches

Many aspects of this system remain to be explored, particularly regarding how groove geometry can be used to shape and control confined films. A first direction is to vary the groove spacing continuously. By engraving grooves with a slight opening angle, for instance $1.8°$, one can provoke film rupture not through a geometric discontinuity but through an fluid instability, as the film becomes laterally overstretched. This phenomenon is illustrated in Figure 5.10(a). This instability typically occurs when the spacing reaches $s \approx 5\,\text{mm} \approx 2\lambda$, providing an experimental estimate for the upper stability limit $s_{\max}$. The deformation of the background pattern reveals that the film thickness decreases smoothly with increasing spacing, consistent with the behavior identified earlier. This result suggests that local control of film thickness can be achieved through the use of non-parallel grooves. Experimentally, this effect is confirmed using structures with alternating convergent and divergent grooves represented in Figure 5.10(b).

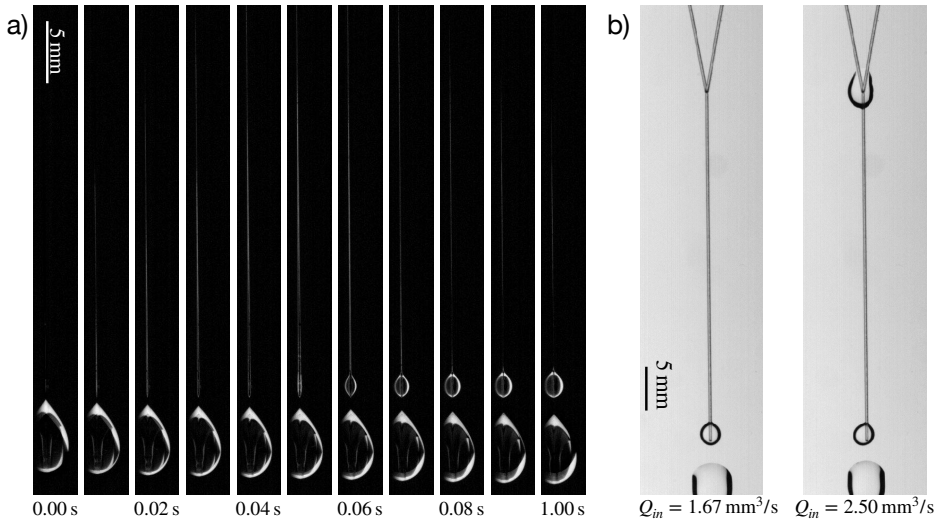

Figure 5.11: (a) Time sequence (frames separated by $0.01\,\mathrm{s}$) showing the creation of a droplet at the lower edge of a single groove. Liquid first accumulates inside the groove, forming a bulge that rises until hydrostatic pressure forces the emergence of a droplet at $t = 0.05\,\mathrm{s}$. After the droplet appears, the groove gradually drains back into it before detachment. (b) Interaction between two converging grooves. For a combined flow rate below the downstream capacity ($Q = 1.67\,\mathrm{mm}^3/\mathrm{s}$), the merged flow remains steady. When the inflow exceeds this capacity ($Q = 2.50\,\mathrm{mm}^3/\mathrm{s}$), a transient droplet forms at the junction, producing a localized popping event before sliding downstream while remaining connected to the underlying groove flow.

The film thickens at constrictions and thins in the widened regions, following the geometry with remarkable fidelity. A similar modulation of film properties could be obtained by varying groove depth instead of spacing. Shallower grooves should produce thicker films, while deeper ones should thinner them, allowing fine spatial control of film thickness and stability.

Beyond this local modulation, a broader question arises about scale. In the present configuration, the film width remains limited by the capillary length, which defines the distance over which lateral confinement can sustain a stable sheet. It is worth asking whether this limit could be overcome by designing a network of parallel grooves that collectively stabilize the film over a much larger width. A simple basic estimate shows that covering a $1\,\mathrm{m}^2$ grooved surface would require a water flow rate of about $1.5\,\mathrm{L/h}$. This could serve as a simple and elegant room humidifier. It could also offer a new way to evaporate seawater for freshwater production, for example.

At the opposite extreme, the fundamental case of a single groove also deserves closer attention. A theoretical framework remains to be developed to describe the flow rate through an open groove as a function of its geometry and its inclination. This would provide the foundation for predicting how individual grooves collect, guide, and release water, and how they might interact when arranged in networks.

The dynamics at the lower end of a groove also raise interesting questions. After each droplet detachment, there is a delay before a new droplet forms at the groove tip, shown in Figure 5.11(a). During this period, liquid accumulates within the groove, gradually rising until the hydrostatic pressure becomes sufficient to create

a new droplet at the base of the groove. Once the droplet emerges, it continues to grow as both groove flow Q_{in} and temporary accumulated water feeds it from above until detachment occurs again.

Moreover, the interaction between grooves offers another promising direction. When two grooves merge into a single downstream channel, the resulting behavior depends on whether the combined inflow exceeds the maximum flow capacity of the outlet groove. If it does not (case $Q = 1.67\,\mathrm{mm}^3/\mathrm{s}$ in Figure 5.11(b)), the flow proceeds smoothly; if it does (case $Q = 2.50\,\mathrm{mm}^3/\mathrm{s}$), a localized droplet forms at the intersection, caused by a flow overload rather than a groove discontinuity. This droplet then slides downstream while remaining connected to the liquid flow within the groove. Such configurations open new avenues for studying droplets that travel atop active grooves, exploring how the groove guides their trajectory, influences their volume, and mediates fluid exchange between the droplet and the confined flow beneath it. This naturally echoes the results presented in Chapter 2 where a droplet slides over fluid trapped inside the grooves such as it decreases the dissipation factor ξ.

Finally, the dynamics of a sweeping droplet confined between two dry grooves are also of interest (Figure 5.2(b)). Such confinement could provide a purely geometric way to control droplet speed and direction. It may also offer a new method to probe dissipation inside the droplet.

5.8 Summary

We demonstrated that geometry alone, specifically, a pair of laser-engraved grooves, is sufficient to stabilize, shape, and control thin water films on vertical or inclined substrates. By pinning the film edges like the extremities of a stretched sheet, these grooves prevent film collapse, enabling the formation of a continuous water layer. This is achieved without chemical coatings or nanoscale surface texturing, offering a fundamentally new and scalable strategy for water control.

Once anchored between the grooves, the water film stretches vertically over more than 100 capillary lengths. Its thickness is continuously tunable through the imposed flow rate and groove geometry, and remains stable until it reaches the groove terminus. There, the sudden loss of lateral pinning triggers a clean, localized rupture, initiating a self-sustained cycle of film retraction, puddle inflation, and droplet release. Both film thickness and retraction height follow predictive scaling laws, while the droplet mass also varies systematically with spacing.

6 Conclusion and Perspectives

6.1 Conclusion

Water management on vertical surfaces is central to many environmental and technological challenges, from atmospheric water harvesting to heat-transfer efficiency. Addressing these challenges requires surfaces that can collect, transport, and release small volumes of water efficiently, without relying on fragile coatings or complex chemical treatments. The central question of this thesis was therefore the following: Can simple geometric features, in particular grooves, govern droplet growth, transport, and release on vertical substrates?

We first addressed this question on one-dimensional substrates. On vertical fibers and fiber bundles, droplets slide under gravity while continuously losing liquid through film deposition. By measuring droplet speed and volume in real time, we showed that their dynamics result from a balance between gravity, surface tension, and viscous dissipation. The grooves formed between fibers trap liquid and modify the dissipation mechanism. As a result, droplets on grooved bundles move systematically faster than on smooth fibers, with speed increases reaching about 20 %.

We then turned to condensation on a vertical plate, where water continuously nucleates, grows, and drains. Here, groove spacing emerged as a key control parameter that selects the dominant drainage mode. For large spacings, condensation proceeds similarly to a smooth surface, with gravitational shedding by sweeping droplets. For small spacings, droplet growth becomes geometrically confined to the plateaus, suppressing classical shedding and redirecting transport into the grooves. Between these two limits, a transition regime appears in which groove drainage and gravitational shedding coexist. This competition produces hybrid drainage dynamics and results in maximal surface water retention.

At the lower edge of the condensing surface, water drained through the grooves must ultimately detach. The organization of dripping is again influenced by the

groove layout on the vertical surface. Depending on groove spacing and depth, dripping ranges from irregular and intermittent to highly organized, with stable detachment points and dripping frequencies. Converging groove patterns fix the location of droplet release precisely. In this way, the lower edge becomes an array of passive capillary outlets whose behavior is programmed by surface geometry alone.

Finally, we reduced the problem to its simplest possible configuration: two grooves engraved on an otherwise smooth vertical plate. This minimal geometry proved sufficient to stabilize a thin film of pure water, a morphology that is intrinsically unstable on a smooth vertical surface at the same flow rate. Anchored laterally by the grooves, the film extended vertically over more than one hundred capillary lengths and remained stable until it reached the groove termination. There, the loss of confinement triggered a clean and periodic rupture, followed by film retraction, puddle inflation, and droplet release. Film thickness, retraction height, and droplet mass obeyed simple scaling laws set by the imposed flow rate and groove geometry.

Taken together, these results establish a unified picture. Grooves act as a minimal infrastructure that governs water behavior on vertical surfaces. They regulate dissipation on fibers, select drainage pathways during condensation, organize dripping at edges, and stabilize or destabilize film. Across all configurations, geometry does not merely influence the flow, it defines where liquid accumulates, how it moves, and when it is released.

Beyond their fundamental interest, these results directly reconnect with the applied motivations outlined in the introduction. In atmospheric water harvesting, where retained droplets limit net yield, the ability of grooves to ease and guide drainage, constrain droplet growth, and localize release provides a purely geometric route to reduce retention without coatings or active control. In cooling systems and heat exchangers, where condensate management governs thermal performance, the demonstration that thin water films can be stabilized, shaped, and made to rupture at prescribed locations using geometry alone offers a new way to think about dropwise and filmwise regimes beyond chemical patterning. More broadly, by showing that gravity-driven droplets and films can be guided, stabilized, and released through simple surface design, this work establishes a physical basis for passive, robust strategies to manage water on open vertical surfaces. In this sense, grooves are not only a model system for studying capillary phenomena, but a scalable design element through which microscale fluid physics can be translated into macroscopic function.

6.2 Perspectives

Taken together, these results show that simple geometric motifs can be combined into a coherent set of operations forming the basis of a millifluidic platform. This section outlines how such a platform emerges from the findings of this thesis and how grooves enable fluid manipulation at the millimeter scale in a simple and scalable way.

Microfluidics is particularly well suited for applications requiring extreme miniaturization, precise control, and very low flow rates. In contrast, this work explores how analogous operations can be achieved at the millimeter scale, where larger

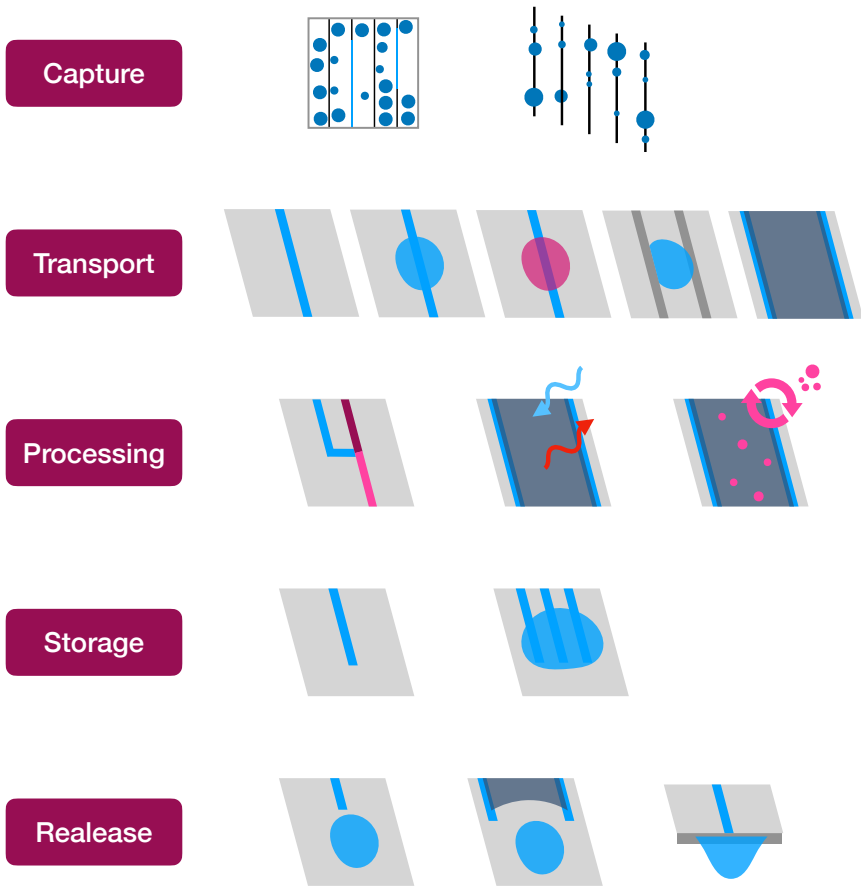

Figure 6.1: Schematic overview of the elementary operations that emerge from geometric confinement. Grooves enable fluid capture through condensation and interception of airborne droplets, transport of liquid along, within, or between grooves under gravity and capillary forces, and processing at groove junctions or at liquid–air interfaces where enhanced exchange or interaction occurs. Liquid may be temporarily stored either inside grooves or above them through capillary pinning. Finally, controlled droplet release occurs at geometric terminations, such as groove ends, film edges, or substrate boundaries. Together, these operations illustrate how surface geometry alone can structure, sequence, and localize fluid behavior on open surfaces.

volumes and flow rates are acceptable and where robustness, simplicity, and cost become dominant constraints. Operating on open geometries further allows direct interaction with the surrounding environment, enabling processes such as evaporation or adsorption that are difficult to integrate within closed-channel systems. Within this regime, devices can be fabricated rapidly and at low cost using laser engraving or mechanical cutting on materials such as PMMA, without specialized facilities. Typical flow rates, from 0.1 to 10 mm^3/s, match situations where water is abundant or continuously supplied. At this scale, systems tolerate complex liquids, operate naturally under gravity, and can extend over centimeters or meters while retaining local control.

Fluid acquisition is the first step. Beyond direct feeding by a syringe pump, the systems developed here also use fully passive inputs. Under condensation, appropriate groove spacing collects and routes droplets directly into the network. Fog capture provides a complementary mechanism, as fibers and grooved structures intercept airborne droplets and guide them downstream. Acquisition, therefore, becomes a built-in function of the geometry.

Once acquired, liquid is transported through modes shaped by geometric confinement. Grooves can channel fluid as one-dimensional capillary pathways, enabling directed transport along the surface. Geometry also allows transport in discrete packets, as droplets slide along grooved fibers or plates with speeds and volumes set by the groove design. A third mode emerges when liquid is confined between paired grooves, which stabilize a continuous thin film with tunable thickness.

Grooves also enables processing. At their junctions, incoming streams merge, producing passive liquid–liquid mixing. Thin films anchored between grooves maximize the liquid–gas interface and serve as sites for evaporation, adsorption, or heat exchange. Geometry therefore governs not only motion but also the interactions that occur along the path.

Storage arises naturally in grooved systems and plays a key role in enabling sequential operations. Droplets pinned at groove ends form stable reservoirs that temporarily hold liquid, while capillary filaments trapped within grooves can store fluid over extended times. These storage modes decouple acquisition, transport, and release in time, allowing downstream processes to proceed before liquid is evacuated. In this way, geometry provides not only pathways for flow, but also built-in buffering that regulates timing within the millifluidic network.

Droplet generation and release follow from the same principles. At the lower edge of a groove, geometry and localization set where and how droplets detach. When a thin film reaches the end of paired grooves, the loss of lateral confinement triggers periodic rupture and produces droplets of reproducible volume. These two mechanisms provide controlled outputs without external actuation.

Together, these capabilities outline how a full millifluidic cycle can be built from simple geometric features. Fluid is acquired, routed, transformed, stored, and released through operations that follow directly from groove layout and gravity. Because the entire sequence is geometry-driven, it requires minimal equipment and few external inputs. This creates a platform where fluid behavior can be programmed through surface design.

Building such a platform raises several challenges. Predictive models for open-groove networks remain incomplete, especially when channels interact or when capillary and gravitational flows compete. The effect of environmental variations such as humidity, temperature, or contamination must be quantified. Many

applications will require coupling between thermal and capillary effects, which remains an open problem. Addressing these questions is essential for turning individual operations into a mature technology.

The operations enabled by geometric confinement become particularly relevant in applications where fluid handling must remain open, robust, and scalable. Groove networks could collect water in fog or dew harvesters and route it directly toward water-quality analysers, integrating acquisition and processing on the same surface. Stable thin films or controlled droplet growth offer new strategies for enhancing heat transfer on surfaces where coatings are undesirable. At smaller scales, grooved substrates provide a low-cost alternative to microfluidic chips in contexts where clean-room fabrication or complex instrumentation is impractical. These examples illustrate how geometry-driven millifluidics naturally extends fluid manipulation into environments that lie beyond the reach of conventional approaches.

Bibliography

[1] K. Calvin, D. Dasgupta, G. Krinner, E. Poloczanska, N. Leprince-Ringuet, and C. Péan, "Climate Change 2023: Synthesis Report," tech. rep., Intergovernmental Panel on Climate Change (IPCC), 2023.

[2] C. Laura and G. Tim, "World Energy Outlook," tech. rep., International Energy Agency, 2025.

[3] B. Dean, J. dulac, T. Morgan, and U. Remme, "The Future of Cooling," tech. rep., International Energy Agency, 2018.

[4] W. Shi, M. J. Anderson, J. B. Tulkoff, B. S. Kennedy, and J. B. Boreyko, "Fog Harvesting with Harps," *ACS Applied Materials & Interfaces*, vol. 10, no. 14, pp. 11979–11986, 2018.

[5] X. Hu, Q. Yi, X. Kong, and J. Wang, "A Review of Research on Dropwise Condensation Heat Transfer," *Applied Sciences*, vol. 11, no. 4, p. 1553, 2021.

[6] H. Jarimi, R. Powell, and S. Riffat, "Review of sustainable methods for atmospheric water harvesting," *International Journal of Low-Carbon Technologies*, vol. 15, no. 2, pp. 253–276, 2020.

[7] A. Moncuquet, A. Mitranescu, O. C. Marchand, S. Ramananarivo, and C. Duprat, "Collecting fog with vertical fibres: Combined laboratory and in-situ study," *Atmospheric Research*, vol. 277, p. 106312, 2022.

[8] D. Monga, P. S. Dosawada, D. Boylan, K. Wyke, P. Wang, and X. Dai, "Designing slippery rough surfaces to enhance dropwise condensation of low surface tension fluid," *International Journal of Heat and Mass Transfer*, vol. 247, p. 127105, 2025.

[9] P. Pou-Álvarez, A. Mongruel, N. Lavielle, A. Riveiro, T. Bourouina, L. Royon, J. Pou, and D. Beysens, "Efficient Autonomous Dew Water Harvesting by Laser Micropatterning: Superhydrophilic and High Emissivity Robust Grooved Metallic Surfaces Enabling Filmwise Condensation and Radiative Cooling," *Advanced Materials*, vol. 37, no. 18, p. 2419472, 2025.

[10] P. Comanns, G. Buchberger, A. Buchsbaum, R. Baumgartner, A. Kogler, S. Bauer, and W. Baumgartner, "Directional, passive liquid transport: the Texas horned lizard as a model for a biomimetic 'liquid diode'," *Journal of The Royal Society Interface*, vol. 12, no. 109, p. 20150415, 2015.

[11] Y. Zheng, H. Bai, Z. Huang, X. Tian, F.-Q. Nie, Y. Zhao, J. Zhai, and L. Jiang, "Directional water collection on wetted spider silk," *Nature*, vol. 463, no. 7281, pp. 640–643, 2010.

[12] J. Ju, H. Bai, Y. Zheng, T. Zhao, R. Fang, and L. Jiang, "A multi-structural and multi-functional integrated fog collection system in cactus," *Nature Communications*, vol. 3, no. 1, p. 1247, 2012.

[13] T. Otitoju, A. Ahmad, and B. Ooi, "Superhydrophilic (superwetting) surfaces: A review on fabrication and application," *Journal of Industrial and Engineering Chemistry*, vol. 47, pp. 19–40, 2017.

[14] C. G. L. Furmidge, "The sliding of liquid drops on solid surfaces and a theory for spray retention," *Journal of Colloid Science*, vol. 17, pp. 309–324, 1962.

[15] J. H. Snoeijer, N. Le Grand-Piteira, L. Limat, H. A. Stone, and J. Eggers, "Cornered drops and rivulets," *Physics of Fluids*, vol. 19, no. 4, p. 042104, 2007.

[16] N. Le Grand-Piteira, A. Daerr, and L. Limat, "Meandering Rivulets on a Plane: A Simple Balance between Inertia and Capillarity," *Physical Review Letters*, vol. 96, no. 25, 2006.

[17] E. Lorenceau, C. Clanet, and D. Quéré, "Capturing drops with a thin fiber," *Journal of Colloid and Interface Science*, vol. 279, no. 1, pp. 192–197, 2004.

[18] T. Gilet, D. Terwagne, and N. Vandewalle, "Droplets sliding on fibres," *The European Physical Journal E*, vol. 31, no. 3, pp. 253–262, 2010.

[19] J. Bico, U. Thiele, and D. Quéré, "Wetting of textured surfaces," *Colloids and Surfaces A: Physicochemical and Engineering Aspects*, vol. 206, no. 1-3, pp. 41–46, 2002.

[20] J. Y. Chung, J. P. Youngblood, and C. M. Stafford, "Anisotropic wetting on tunable micro-wrinkled surfaces," *Soft Matter*, vol. 3, no. 9, p. 1163, 2007.

[21] R. D. Narhe and D. A. Beysens, "Nucleation and Growth on a Superhydrophobic Grooved Surface," *Physical Review Letters*, vol. 93, no. 7, p. 076103, 2004.

[22] P.-B. Bintein, H. Lhuissier, A. Mongruel, L. Royon, and D. Beysens, "Grooves Accelerate Dew Shedding," *Physical Review Letters*, vol. 122, no. 9, p. 098005, 2019.

[23] P.-G. De Gennes, F. Brochard-Wyart, and D. Quéré, *Capillarity and wetting phenomena: drops, bubbles, pearls, waves*. Springer Science & Business Media, 2003.

[24] J. A. F. Plateau, *Statique expérimentale et théorique des liquides soumis aux seules forces moléculaires*, vol. 2. Gauthier-Villars, 1873.

[25] L. Reyleigh, "On the Instability of a Cylinder of Viscous Liquid under Capillary Force.," *The London, Edinburgh, and Dublin Philosophical Magazine and Journal of Science*, vol. 34, no. 207, pp. 145–154, 1892.

[26] J. Van Hulle, *Droplet dynamics on curved substrates*. PhD thesis, Uliège, 2024.

[27] N. Le Grand-Piteira, *Ruissellement avec effets de mouillage: Gouttes et méandres sur un plan incliné*. PhD Thesis, Université Paris-Diderot-Paris VII, 2006.

[28] A. L. Yarin, A. Oron, and P. Rosenau, "Capillary instability of thin liquid film on a cylinder," *Physics of Fluids A: Fluid Dynamics*, vol. 5, no. 1, pp. 91–98, 1993.

[29] T. Podgorski, J.-M. Flesselles, and L. Limat, "Corners, Cusps, and Pearls in Running Drops," *Physical Review Letters*, vol. 87, no. 3, p. 036102, 2001.

[30] N. Le Grand-Piteira, A. Daerr, and L. Limat, "Shape and motion of drops sliding down an inclined plane," *Journal of Fluid Mechanics*, vol. 541, no. -1, p. 293, 2005.

[31] A. Yarin, "DROP IMPACT DYNAMICS: Splashing, Spreading, Receding, Bouncing…," *Annual Review of Fluid Mechanics*, vol. 38, no. 1, pp. 159–192, 2006.

[32] The Engineering ToolBox, "Surface Tension," 2005.

[33] D. Quéré, "Wetting and Roughness," *Annual Review of Materials Research*, vol. 38, no. 1, pp. 71–99, 2008.

[34] L. H. Tanner, "The spreading of silicone oil drops on horizontal surfaces," *Journal of Physics D: Applied Physics*, vol. 12, no. 9, pp. 1473–1484, 1979.

[35] A. M. Cazabat and M. A. C. Stuartt, "Dynamics of Wettlng: Effects of Surface Roughness," *The Journal of Physical Chemistry*, vol. 90, no. 22, pp. 5845–5849, 1986.

[36] M. N. Popescu, G. Oshanin, S. Dietrich, and A.-M. Cazabat, "Precursor films in wetting phenomena," *Journal of Physics: Condensed Matter*, vol. 24, no. 24, p. 243102, 2012.

[37] T. Young, "An essay on the cohesion of fluids," *Philosophical Transactions of the Royal Society of London*, vol. 95, pp. 65–87, 1805.

[38] W. Barthlott and C. Neinhuis, "Purity of the sacred lotus, or escape from contamination in biological surfaces," *Planta*, vol. 202, no. 1, pp. 1–8, 1997.

[39] H. Chen, P. Zhang, L. Zhang, H. Liu, Y. Jiang, D. Zhang, Z. Han, and L. Jiang, "Continuous directional water transport on the peristome surface of Nepenthes alata," *Nature*, vol. 532, no. 7597, pp. 85–89, 2016.

[40] R. Seemann, M. Brinkmann, E. J. Kramer, F. F. Lange, and R. Lipowsky, "Wetting morphologies at microstructured surfaces," *Proceedings of the National Academy of Sciences*, vol. 102, no. 6, pp. 1848–1852, 2005.

[41] R. Seemann, M. Brinkmann, S. Herminghaus, K. Khare, B. M. Law, S. McBride, K. Kostourou, E. Gurevich, S. Bommer, C. Herrmann, and D. Michler, "Wetting morphologies and their transitions in grooved substrates," *Journal of Physics: Condensed Matter*, vol. 23, no. 18, p. 184108, 2011.

[42] R. N. Wenzel, “RESISTANCE OF SOLID SURFACES TO WETTING BY WATER,” *Industrial & Engineering Chemistry*, vol. 28, no. 8, pp. 988–994, 1936.

[43] P. G. De Gennes, “Wetting: statics and dynamics,” *Reviews of Modern Physics*, vol. 57, no. 3, pp. 827–863, 1985.

[44] C. Extrand and A. Gent, “Retention of liquid drops by solid surfaces,” *Journal of Colloid and Interface Science*, vol. 138, no. 2, pp. 431–442, 1990.

[45] D. Quéré, M.-J. Azzopardi, and L. Delattre, “Drops at Rest on a Tilted Plane,” *Langmuir*, vol. 14, no. 8, pp. 2213–2216, 1998.

[46] P. G. De Gennes, “Deposition of Langmuir-Blodgett layers,” *Colloid and Polymer Science*, vol. 264, no. 5, pp. 463–465, 1986.

[47] J. H. Snoeijer and B. Andreotti, “Moving Contact Lines: Scales, Regimes, and Dynamical Transitions,” *Annual Review of Fluid Mechanics*, vol. 45, no. 1, pp. 269–292, 2013.

[48] T. A. Ghezzehei, “Constraints for flow regimes on smooth fracture surfaces,” *Water Resources Research*, vol. 40, no. 11, p. 2004WR003164, 2004.

[49] S. Kuronuma and M. Sano, “Stability and Bifurcations of Tube Conveying Flow,” *Journal of the Physical Society of Japan*, vol. 72, no. 12, pp. 3106–3112, 2003.

[50] B. Birnir, K. Mertens, V. Putkaradze, and P. Vorobieff, “Meandering Fluid Streams in the Presence of Flow-Rate Fluctuations,” *Physical Review Letters*, vol. 101, no. 11, p. 114501, 2008.

[51] B. Birnir, K. Mertens, V. Putkaradze, and P. Vorobieff, “Morphology of a stream flowing down an inclined plane. Part 2. Meandering,” *Journal of Fluid Mechanics*, vol. 607, pp. 401–411, 2008.

[52] K. Mertens, V. Putkaradze, and P. Vorobieff, “Braiding patterns on an inclined plane,” *Nature*, vol. 430, no. 6996, pp. 165–165, 2004.

[53] F. Brochard, “Spreading of liquid drops on thin cylinders: The ‘‘manchon/droplet’’ transition,” *The Journal of Chemical Physics*, vol. 84, no. 8, pp. 4664–4672, 1986.

[54] B. Carroll, “The accurate measurement of contact angle, phase contact areas, drop volume, and Laplace excess pressure in drop-on-fiber systems,” *Journal of Colloid and Interface Science*, vol. 57, no. 3, pp. 488–495, 1976.

[55] G. McHale, N. Käb, M. Newton, and S. Rowan, “Wetting of a High-Energy Fiber Surface,” *Journal of Colloid and Interface Science*, vol. 186, no. 2, pp. 453–461, 1997.

[56] K. A. Brakke, “The Surface Evolver,” *Experimental Mathematics*, vol. 1, no. 2, pp. 141–165, 1992.

[57] G. Mchale, M. I. Newton, and B. J. Carroll, "The Shape and Stability of Small Liquid Drops on Fibers," *Oil & Gas Science and Technology*, vol. 56, no. 1, pp. 47–54, 2001.

[58] G. McHale and M. I. Newton, "Global geometry and the equilibrium shapes of liquid drops on fibers," *Colloids and Surfaces A: Physicochemical and Engineering Aspects*, vol. 206, no. 1-3, pp. 79–86, 2002.

[59] T.-H. Chou, S.-J. Hong, Y.-E. Liang, H.-K. Tsao, and Y.-J. Sheng, "Equilibrium Phase Diagram of Drop-on-Fiber: Coexistent States and Gravity Effect," *Langmuir*, vol. 27, no. 7, pp. 3685–3692, 2011.

[60] B. J. Carroll, "Equilibrium conformations of liquid drops on thin cylinders under forces of capillarity. A theory for the roll-up process," *Langmuir*, vol. 2, no. 2, pp. 248–250, 1986.

[61] H. B. Eral, J. De Ruiter, R. De Ruiter, J. M. Oh, C. Semprebon, M. Brinkmann, and F. Mugele, "Drops on functional fibers: from barrels to clamshells and back," *Soft Matter*, vol. 7, no. 11, p. 5138, 2011.

[62] D. Quéré, "FLUID COATING ON A FIBER," *Annual Review of Fluid Mechanics*, vol. 31, no. 1, pp. 347–384, 1999.

[63] L. Landau and B. Levich, "Dragging of a Liquid by a Moving Plate," in *Dynamics of Curved Fronts*, pp. 141–153, Elsevier, 1988.

[64] F. P. Bretherton, "The motion of long bubbles in tubes," *Journal of Fluid Mechanics*, vol. 10, no. 2, pp. 166–188, 1961.

[65] D. White and J. Tallmadge, "Theory of drag out of liquids on flat plates," *Chemical Engineering Science*, vol. 20, no. 1, pp. 33–37, 1965.

[66] R. V. Sedev and J. G. Petrov, "Influence of geometry on steady dewetting kinetics," *Colloids and Surfaces*, vol. 62, no. 1-2, pp. 141–151, 1992.

[67] A. De Ryck and D. Quéré, "Quick Forced Spreading," *Europhysics Letters (EPL)*, vol. 25, no. 3, pp. 187–192, 1994.

[68] A. De Ryck and D. Quéré, "Inertial coating of a fibre," *Journal of Fluid Mechanics*, vol. 311, pp. 219–237, 1996.

[69] S. Haefner, M. Benzaquen, O. Bäumchen, T. Salez, R. Peters, J. D. McGraw, K. Jacobs, E. Raphaël, and K. Dalnoki-Veress, "Influence of slip on the Plateau–Rayleigh instability on a fibre," *Nature Communications*, vol. 6, no. 1, p. 7409, 2015.

[70] Z. Huang, X. Liao, Y. Kang, G. Yin, and Y. Yao, "Equilibrium of drops on inclined fibers," *Journal of Colloid and Interface Science*, vol. 330, no. 2, pp. 399–403, 2009.

[71] C. T. Gabbard and J. B. Bostwick, "Asymmetric instability in thin-film flow down a fiber," *Physical Review Fluids*, vol. 6, no. 3, p. 034005, 2021.

[72] T. Shlang and G. Sivashinsky, "Irregular flow of a liquid film down a vertical column," *Journal de Physique*, vol. 43, no. 3, pp. 459–466, 1982.

[73] A. L. Frenkel, "Nonlinear Theory of Strongly Undulating Thin Films Flowing Down Vertical Cylinders," *Europhysics Letters (EPL)*, vol. 18, no. 7, pp. 583–588, 1992.

[74] D. Quéré, "Thin Films Flowing on Vertical Fibers," *Europhysics Letters (EPL)*, vol. 13, no. 8, pp. 721–726, 1990.

[75] I. L. Kliakhandler, S. H. Davis, and S. G. Bankoff, "Viscous beads on vertical fibre," *Journal of Fluid Mechanics*, vol. 429, pp. 381–390, 2001.

[76] C. Duprat, C. Ruyer-Quil, and F. Giorgiutti-Dauphiné, "Spatial evolution of a film flowing down a fiber," *Physics of Fluids*, vol. 21, no. 4, p. 042109, 2009.

[77] A. Cazaubiel and A. Carlson, "Influence of wind on a viscous liquid film flowing down a thread," *Physical Review Fluids*, vol. 8, no. 5, p. 054002, 2023.

[78] A. Sadeghpour, Z. Zeng, and Y. S. Ju, "Effects of Nozzle Geometry on the Fluid Dynamics of Thin Liquid Films Flowing down Vertical Strings in the Rayleigh–Plateau Regime," *Langmuir*, vol. 33, no. 25, pp. 6292–6299, 2017.

[79] D. K. Maity, Christopher Wagstaff, S. Dighe, and T. Truscott, "Rayleigh-Plateau instability on an angled and eccentric wire," *Physical Review Fluids*, vol. 10, no. 11, p. 113901, 2025.

[80] S. Protiere, C. Duprat, and H. A. Stone, "Wetting on two parallel fibers: drop to column transitions," *Soft Matter*, vol. 9, no. 1, pp. 271–276, 2013.

[81] C. T. Gabbard and J. B. Bostwick, "Thin film flow between fibers: Inertial sheets and liquid bridge patterns," *Physical Review Fluids*, vol. 8, no. 11, p. 110505, 2023.

[82] V. R. Kern and A. Carlson, "Twisted fibers enable drop flow control and enhance fog capture," *Proceedings of the National Academy of Sciences*, vol. 121, no. 32, p. e2402252121, 2024.

[83] F. Weyer, A. Duchesne, and N. Vandewalle, "Switching behavior of droplets crossing nodes on a fiber network," *Scientific Reports*, vol. 7, no. 1, p. 13309, 2017.

[84] J. Bico, É. Reyssat, and B. Roman, "Elastocapillarity: when surface tension deforms elastic solids," *Annual Review of Fluid Mechanics*, vol. 50, no. 1, pp. 629–659, 2018.

[85] C. T. Gabbard and J. B. Bostwick, "Gravity-driven flow of liquid bridges between vertical fibres," *Journal of Fluid Mechanics*, vol. 997, p. A74, 2024.

[86] J. Van Hulle, C. Delforge, M. Léonard, E. Follet, and N. Vandewalle, "Droplet Helical Motion on Twisted Fibers," *Langmuir*, vol. 40, no. 48, pp. 25413–25419, 2024.

[87] Z. Pan, F. Weyer, W. G. Pitt, N. Vandewalle, and T. T. Truscott, "Drop on a bent fibre," *Soft Matter*, vol. 14, no. 19, pp. 3724–3729, 2018.

[88] Y. Zhang and Z. Pan, "Droplets Suspended Beneath a Fiber Hub," *Langmuir*, p. acs.langmuir.5c01175, 2025.

[89] T. Gilet, D. Terwagne, and N. Vandewalle, "Digital microfluidics on a wire," *Applied Physics Letters*, vol. 95, no. 1, p. 014106, 2009.

[90] H. K. Khattak, A. Shanzeela, E. Raphael, and K. Dalnoki-Veress, "Directed droplet motion along thin fibers," *PNAS Nexus*, vol. 3, no. 3, p. 86, 2024.

[91] C. Duprat, S. Protière, A. Y. Beebe, and H. A. Stone, "Wetting of flexible fibre arrays," *Nature*, vol. 482, no. 7386, pp. 510–513, 2012.

[92] J. Bico, B. Roman, L. Moulin, and A. Boudaoud, "Elastocapillary coalescence in wet hair," *Nature*, vol. 432, no. 7018, pp. 690–690, 2004.

[93] B. Roman and J. Bico, "Elasto-capillarity: deforming an elastic structure with a liquid droplet," *Journal of Physics: Condensed Matter*, vol. 22, no. 49, p. 493101, 2010.

[94] S. H. Tawfick, J. Bico, and S. Barcelo, "Three-dimensional lithography by elasto-capillary engineering of filamentary materials," *MRS Bulletin*, vol. 41, no. 2, pp. 108–114, 2016.

[95] M. P. Anisimov, "Nucleation: theory and experiment," *Russian Chemical Reviews*, vol. 72, no. 7, pp. 591–628, 2003.

[96] J. Trosseille, A. Mongruel, L. Royon, M.-G. Medici, and D. Beysens, "Roughness-enhanced collection of condensed droplets," *The European Physical Journal E*, vol. 42, no. 11, p. 144, 2019.

[97] N. Lavielle, D. Beysens, and A. Mongruel, "Memory Re-Condensation," *Langmuir*, vol. 39, no. 5, pp. 2008–2014, 2023.

[98] D. Beysens, "Dew nucleation and growth," *Comptes Rendus. Physique*, vol. 7, no. 9-10, pp. 1082–1100, 2006.

[99] M.-G. Medici, A. Mongruel, L. Royon, and D. Beysens, "Edge effects on water droplet condensation," *Physical Review E*, vol. 90, no. 6, p. 062403, 2014.

[100] Y. Jin, L. Zhang, and P. Wang, "Atmospheric Water Harvesting: Role of Surface Wettability and Edge Effect," *Global Challenges*, vol. 1, no. 4, p. 1700019, 2017.

[101] D. Nioras, K. Ellinas, V. Constantoudis, and E. Gogolides, "How Different Are Fog Collection and Dew Water Harvesting on Surfaces with Different Wetting Behaviors?," *ACS Applied Materials & Interfaces*, vol. 13, no. 40, pp. 48322–48332, 2021.

[102] C. Hiatt, D. Fernandez, and C. Potter, "Measurements of Fog Water Deposition on the California Central Coast," *Atmospheric and Climate Sciences*, vol. 02, no. 04, pp. 525–531, 2012.

[103] D. J. Straub, J. W. Hutchings, and P. Herckes, "Measurements of fog composition at a rural site," *Atmospheric Environment*, vol. 47, pp. 195–205, 2012.

[104] J. K. Domen, W. T. Stringfellow, M. K. Camarillo, and S. Gulati, "Fog water as an alternative and sustainable water resource," *Clean Technologies and Environmental Policy*, vol. 16, no. 2, pp. 235–249, 2014.

[105] A. Ritter, C. M. Regalado, and G. Aschan, "Fog Water Collection in a Subtropical Elfin Laurel Forest of the Garajonay National Park (Canary Islands): A Combined Approach Using Artificial Fog Catchers and a Physically Based Impaction Model," *Journal of Hydrometeorology*, vol. 9, no. 5, pp. 920–935, 2008.

[106] S. Montecinos, D. Carvajal, P. Cereceda, and M. Concha, "Collection efficiency of fog events," *Atmospheric Research*, vol. 209, pp. 163–169, 2018.

[107] T. E. Dawson, "Fog in the California redwood forest: ecosystem inputs and use by plants," *Oecologia*, vol. 117, no. 4, pp. 476–485, 1998.

[108] E. del Val, J. J. Armesto, O. Barbosa, D. A. Christie, A. G. Gutiérrez, C. G. Jones, P. A. Marquet, and K. C. Weathers, "Rain Forest Islands in the Chilean Semiarid Region: Fog-dependency, Ecosystem Persistence and Tree Regeneration," *Ecosystems*, vol. 9, no. 4, pp. 598–608, 2006.

[109] J. R. Henschel and M. K. Seely, "Ecophysiology of atmospheric moisture in the Namib Desert," *Atmospheric Research*, vol. 87, no. 3-4, pp. 362–368, 2008.

[110] A. Lummerich and T. Kai, "Conference on International Research on Food Security, Natural Resource Management and Rural Development," 2009.

[111] S. LaDochy and M. Witiw, "The Continued Reduction in Dense Fog in the Southern California Region: Possible Causes," *Pure and Applied Geophysics*, vol. 169, no. 5-6, pp. 1157–1163, 2012.

[112] R. S. Schemenauer and P. Cereceda, "Fog collection's role in water planning for developing countries," *Natural Resources Forum*, vol. 18, no. 2, pp. 91–100, 1994.

[113] M. J. Estrela, J. A. Valiente, D. Corell, D. Fuentes, and A. Valdecantos, "Prospective use of collected fog water in the restoration of degraded burned areas under dry Mediterranean conditions," *Agricultural and Forest Meteorology*, vol. 149, no. 11, pp. 1896–1906, 2009.

[114] J. D. D. Rivera, "Aerodynamic collection efficiency of fog water collectors," *Atmospheric Research*, vol. 102, no. 3, pp. 335–342, 2011.

[115] K.-C. Park, S. S. Chhatre, S. Srinivasan, R. E. Cohen, and G. H. McKinley, "Optimal Design of Permeable Fiber Network Structures for Fog Harvesting," *Langmuir*, vol. 29, no. 43, pp. 13269–13277, 2013.

[116] P.-B. Bintein, A. Cornu, F. Weyer, N. De Coster, N. Vandewalle, and D. Terwagne, "Kirigami fog nets: how strips improve water collection," *npj Clean Water*, vol. 6, no. 1, p. 54, 2023.

[117] S. Li, J. Zhu, C. Liu, R. Zhang, J. Liu, and Z. Guo, "Load-responsive bionic kirigami structures for high-efficient fog harvesting," *Chemical Engineering Journal*, vol. 464, p. 142549, 2023.

[118] H. Bai, T. Zhao, X. Wang, Y. Wu, K. Li, C. Yu, L. Jiang, and M. Cao, "Cactus kirigami for efficient fog harvesting: simplifying a 3D cactus into 2D paper art," *Journal of Materials Chemistry A*, vol. 8, no. 27, pp. 13452–13458, 2020.

[119] C. M. Regalado, C. F. Carballo, and M. T. Arencibia, "A Bioinspired Ladder-Like Harp Fog Water Collector. I. Model Design, Simulations and Laboratory Testing," 2025.

[120] M. Mosa, F. Radwan, H. Al-Ghobari, H. Fouli, and A. A. Alazba, "Impact of varied fog collector designs on fog and rainwater harvesting under fluctuating wind speed and direction," *Earth Science Informatics*, vol. 17, no. 1, pp. 617–631, 2024.

[121] M. A. K. Azad, D. Ellerbrok, W. Barthlott, and K. Koch, "Fog collecting biomimetic surfaces: Influence of microstructure and wettability," *Bioinspiration & Biomimetics*, vol. 10, no. 1, p. 016004, 2015.

[122] J. K. Kaindu, L. E. Olejnicki, B. S. Kennedy, and J. B. Boreyko, "Anti-clogging and anti-tangling fog harvesting with 3D-printed mesh-harp hybrids," *Journal of Materials Chemistry A*, p. 10.1039.D5TA02686E, 2025.

[123] M. Azeem, M. T. Noman, J. Wiener, M. Petru, and P. Louda, "Structural design of efficient fog collectors: A review," *Environmental Technology & Innovation*, vol. 20, p. 101169, 2020.

[124] S. A. Abdul-Wahab, H. Al-Hinai, K. A. Al-Najar, and M. S. Al-Kalbani, "Feasibility of fog water collection: a case study from Oman," *Journal of Water Supply: Research and Technology-Aqua*, vol. 56, no. 4, pp. 275–280, 2007.

[125] O. Klemm, R. S. Schemenauer, A. Lummerich, P. Cereceda, V. Marzol, D. Corell, J. Van Heerden, D. Reinhard, T. Gherezghiher, J. Olivier, P. Osses, J. Sarsour, E. Frost, M. J. Estrela, J. A. Valiente, and G. M. Fessehaye, "Fog as a Fresh-Water Resource: Overview and Perspectives," *AMBIO*, vol. 41, no. 3, pp. 221–234, 2012.

[126] J. D. D. Rivera and D. Lopez-Garcia, "Mechanical characteristics of Raschel mesh and their application to the design of large fog collectors," *Atmospheric Research*, vol. 151, pp. 250–258, 2015.

[127] O. Klemm, A. Bachmeier, R. Talbot, and K. Klemm, "Fog chemistry at the new england coast: Influence of air mass history," *Atmospheric Environment*, vol. 28, no. 6, pp. 1181–1188, 1994.

[128] C. D. Ritchie, W. Richards, and P. A. Arp, "Mercury in fog on the Bay of Fundy (Canada)," *Atmospheric Environment*, vol. 40, no. 33, pp. 6321–6328, 2006.

[129] D. Beysens, *Dew Water*. River Publishers, 1st ed., 2018.

[130] Y. Cui, X. Luo, F. Zhang, L. Sun, N. Jin, and W. Yang, "Progress of passive daytime radiative cooling technologies towards commercial applications," *Particuology*, vol. 67, pp. 57–67, 2022.

[131] I. Haechler, H. Park, G. Schnoering, T. Gulich, M. Rohner, A. Tripathy, A. Milionis, T. M. Schutzius, and D. Poulikakos, "Exploiting radiative cooling for uninterrupted 24-hour water harvesting from the atmosphere," *Science Advances*, vol. 7, no. 26, p. eabf3978, 2021.

[132] S. Ahmad, A. R. Siddiqui, K. Yang, M. Zhou, H. M. Ali, R. Hardian, G. Szekely, D. Daniel, S. Yang, and Q. Gan, "Lubricated Surface in a Vertical Double-Sided Architecture for Radiative Cooling and Atmospheric Water Harvesting," *Advanced Materials*, vol. 36, no. 51, p. 2404037, 2024.

[133] C. G. Granqvist and A. Hjortsberg, "Radiative cooling to low temperatures: General considerations and application to selectively emitting SiO films," *Journal of Applied Physics*, vol. 52, no. 6, pp. 4205–4220, 1981.

[134] I. Lekouch, K. Lekouch, M. Muselli, A. Mongruel, B. Kabbachi, and D. Beysens, "Rooftop dew, fog and rain collection in southwest Morocco and predictive dew modeling using neural networks," *Journal of Hydrology*, vol. 448-449, pp. 60–72, 2012.

[135] D. Beysens, I. Milimouk, V. Nikolayev, M. Muselli, and J. Marcillat, "Using radiative cooling to condense atmospheric vapor: a study to improve water yield," *Journal of Hydrology*, vol. 276, no. 1-4, pp. 1–11, 2003.

[136] G. Sharan, O. Clus, S. Singh, M. Muselli, and D. Beysens, "A very large dew and rain ridge collector in the Kutch area (Gujarat, India)," *Journal of Hydrology*, vol. 405, no. 1-2, pp. 171–181, 2011.

[137] M. Muselli, D. Beysens, M. Mileta, and I. Milimouk, "Dew and rain water collection in the Dalmatian Coast, Croatia," *Atmospheric Research*, vol. 92, no. 4, pp. 455–463, 2009.

[138] O. Clus, J. Ouazzani, M. Muselli, V. Nikolayev, G. Sharan, and D. Beysens, "Comparison of various radiation-cooled dew condensers using computational fluid dynamics," *Desalination*, vol. 249, no. 2, pp. 707–712, 2009.

[139] M. Ebner, T. Miranda, and A. Roth-Nebelsick, "Efficient fog harvesting by Stipagrostis sabulicola (Namib dune bushman grass)," *Journal of Arid Environments*, vol. 75, no. 6, pp. 524–531, 2011.

[140] H. G. Andrews, E. A. Eccles, W. C. E. Schofield, and J. P. S. Badyal, "Three-Dimensional Hierarchical Structures for Fog Harvesting," *Langmuir*, vol. 27, no. 7, pp. 3798–3802, 2011.

[141] Z. Pan, W. G. Pitt, Z. Y. Zhang YuanMing, W. N. Wu Nan, T. Y. Tao Ye, and T. T. Truscott, "The upside-down water collection system of Syntrichia caninervis.," vol. 2, no. 7, p. 16076, 2016.

[142] F. Weyer, M. Ben Said, J. Hötzer, M. Berghoff, L. Dreesen, B. Nestler, and N. Vandewalle, "Compound Droplets on Fibers," *Langmuir*, vol. 31, no. 28, pp. 7799–7805, 2015.

[143] A. Jones, *Pappus of Alexandria Book 7 of the Collection*, vol. 8 of *Sources in the History of Mathematics and Physical Sciences*. Springer, 1 ed., 1986.

[144] J. Van Hulle, F. Weyer, S. Dorbolo, and N. Vandewalle, "Capillary transport from barrel to clamshell droplets on conical fibers," *Physical Review Fluids*, vol. 6, no. 2, p. 024501, 2021.

[145] E. Lorenceau and D. Quéré, "Drops on a conical wire," *Journal of Fluid Mechanics*, vol. 510, pp. 29–45, 2004.

[146] P.-G. d. Gennes, F. Brochard-Wyart, and D. Quéré, *Gouttes, bulles, perles et ondes*. Echelles, Paris: Belin, nouvelle éd. avec cd ed., 2013.

[147] J. Van Hulle, N. Vandewalle, and Z. Pan, "Multiple droplets dynamics on cylindrical fiber," 2025.

[148] W. Shi, T. W. Van Der Sloot, B. J. Hart, B. S. Kennedy, and J. B. Boreyko, "Harps Enable Water Harvesting under Light Fog Conditions," *Advanced Sustainable Systems*, vol. 4, no. 6, p. 2000040, 2020.

[149] Y. Jiang, C. Machado, S. Savarirayan, N. A. Patankar, and K.-C. Park, "Onset time of fog collection," *Soft Matter*, vol. 15, no. 34, pp. 6779–6783, 2019.

[150] K. Luan, M. He, B. Xu, P. Wang, J. Zhou, B. Hu, L. Jiang, and H. Liu, "Spontaneous Directional Self-Cleaning on the Feathers of the Aquatic Bird *Anser cygnoides domesticus* Induced by a Transient Superhydrophilicity," *Advanced Functional Materials*, vol. 31, no. 26, p. 2010634, 2021.

[151] A. Jacobs, B. Heusinkveld, and S. Berkowicz, "Passive dew collection in a grassland area, The Netherlands," *Atmospheric Research*, vol. 87, no. 3-4, pp. 377–385, 2008.

[152] G. Gittens, "Variation of surface tension of water with temperature," *Journal of Colloid and Interface Science*, vol. 30, no. 3, pp. 406–412, 1969.

[153] N. Gao, F. Geyer, D. W. Pilat, S. Wooh, D. Vollmer, H.-J. Butt, and R. Berger, "How drops start sliding over solid surfaces," *Nature Physics*, vol. 14, no. 2, pp. 191–196, 2018.

[154] J. W. Rose, "Dropwise condensation theory and experiment: A review," *Proceedings of the Institution of Mechanical Engineers, Part A: Journal of Power and Energy*, vol. 216, no. 2, pp. 115–128, 2002.

[155] R. D. Narhe and D. A. Beysens, "Water condensation on a super-hydrophobic spike surface," *Europhysics Letters (EPL)*, vol. 75, no. 1, pp. 98–104, 2006.

[156] P. Schmuki and M. Laso, "On the stability of rivulet flow," *Journal of Fluid Mechanics*, vol. 215, no. -1, p. 125, 1990.

[157] M. Rietz, B. Scheid, F. Gallaire, N. Kofman, R. Kneer, and W. Rohlfs, "Dynamics of falling films on the outside of a vertical rotating cylinder: waves, rivulets and dripping transitions," *Journal of Fluid Mechanics*, vol. 832, pp. 189–211, 2017.

[158] H. Chen, T. Ran, Y. Gan, J. Zhou, Y. Zhang, L. Zhang, D. Zhang, and L. Jiang, "Ultrafast water harvesting and transport in hierarchical microchannels," *Nature Materials*, vol. 17, no. 10, pp. 935–942, 2018.

[159] E. Jambon-Puillet, W. Bouwhuis, J. Snoeijer, and D. Bonn, "Liquid Helix: How Capillary Jets Adhere to Vertical Cylinders," *Physical Review Letters*, vol. 122, no. 18, p. 184501, 2019.

[160] B. Darbois Texier and S. Dorbolo, "Droplets climbing a rotating helical fiber," *The European Physical Journal E*, vol. 38, no. 12, p. 131, 2015.

[161] S. Wang and O. Desjardins, "Numerical study of the critical drop size on a thin horizontal fiber: Effect of fiber shape and contact angle," *Chemical Engineering Science*, vol. 187, pp. 127–133, 2018.

[162] J. Park and S. Kumar, "Droplet Sliding on an Inclined Substrate with a Topographical Defect," *Langmuir*, vol. 33, no. 29, pp. 7352–7363, 2017.

[163] E. Jambon-Puillet, "Gravito-capillary trapping of pendant droplets under wet uneven surfaces," *Physical Review Fluids*, vol. 9, no. 8, p. L081601, 2024.

[164] N. Bremond, C. Clanet, and E. Villermaux, "Atomization of undulating liquid sheets," *Journal of Fluid Mechanics*, vol. 585, pp. 421–456, 2007.

[165] A. Lee, M.-W. Moon, H. Lim, W.-D. Kim, and H.-Y. Kim, "Water harvest via dewing," *Langmuir*, vol. 28, no. 27, pp. 10183–10191, 2012.

[166] S. Kim and K. J. Kim, "Dropwise Condensation Modeling Suitable for Superhydrophobic Surfaces," *Journal of Heat Transfer*, vol. 133, no. 8, p. 081502, 2011.

[167] Y. Chen, B. He, J. Lee, and N. A. Patankar, "Anisotropy in the wetting of rough surfaces," *Journal of Colloid and Interface Science*, vol. 281, no. 2, pp. 458–464, 2005.

[168] X. Dai, N. Sun, S. O. Nielsen, B. B. Stogin, J. Wang, S. Yang, and T.-S. Wong, "Hydrophilic directional slippery rough surfaces for water harvesting," *Science Advances*, vol. 4, no. 3, p. eaaq0919, 2018.

[169] G. Bamorovat Abadi and M. Bahrami, "A general form of capillary rise equation in micro-grooves," *Scientific Reports*, vol. 10, no. 1, 2020.

[170] J. Van Hulle and N. Vandewalle, "Effect of groove curvature on droplet spreading," *Soft Matter*, vol. 19, no. 25, pp. 4669–4675, 2023.

[171] M. Léonard, J. Van Hulle, F. Weyer, D. Terwagne, and N. Vandewalle, "Droplets sliding on single and multiple vertical fibers," *Physical Review Fluids*, vol. 8, no. 10, p. 103601, 2023.

[172] M. Léonard, D. Maity, N. Vandewalle, and T. Truscott, "Stretching water between two grooves,"

[173] M. Leonard and N. Vandewalle, "Grooves spacing govern water retention during condensation," *Physical Review Fluids*, vol. 10, no. 11, p. 114001, 2025.

[174] D. Orejon, O. Shardt, N. S. K. Gunda, T. Ikuta, K. Takahashi, Y. Takata, and S. K. Mitra, "Simultaneous dropwise and filmwise condensation on hydrophilic microstructured surfaces," *International Journal of Heat and Mass Transfer*, vol. 114, pp. 187–197, 2017.

[175] H. Zhu, Y. Huang, S. Zhang, S. Jin, X. Lou, and F. Xia, "A universal, multifunctional, high-practicability superhydrophobic paint for waterproofing grass houses," *NPG Asia Materials*, vol. 13, no. 1, p. 47, 2021.

[176] J. Drelich, E. Chibowski, D. D. Meng, and K. Terpilowski, "Hydrophilic and superhydrophilic surfaces and materials," *Soft Matter*, vol. 7, no. 21, p. 9804, 2011.

[177] F. Geyer, M. D'Acunzi, A. Sharifi-Aghili, A. Saal, N. Gao, A. Kaltbeitzel, T.-F. Sloot, R. Berger, H.-J. Butt, and D. Vollmer, "When and how self-cleaning of superhydrophobic surfaces works," *Science Advances*, vol. 6, no. 3, p. eaaw9727, 2020.

[178] M. Choi, L. Xiangde, J. Park, D. Choi, J. Heo, M. Chang, C. Lee, and J. Hong, "Superhydrophilic coatings with intricate nanostructure based on biotic materials for antifogging and antibiofouling applications," *Chemical Engineering Journal*, vol. 309, pp. 463–470, 2017.

[179] S. Couvreur and A. Daerr, "The role of wetting heterogeneities in the meandering instability of a partial wetting rivulet," *EPL (Europhysics Letters)*, vol. 99, no. 2, p. 24004, 2012.

[180] A. Vrij and J. T. G. Overbeek, "Rupture of thin liquid films due to spontaneous fluctuations in thickness," *Journal of the American Chemical Society*, vol. 90, no. 12, pp. 3074–3078, 1968.

[181] S. Shibuichi, T. Onda, N. Satoh, and K. Tsujii, "Super Water-Repellent Surfaces Resulting from Fractal Structure," *The Journal of Physical Chemistry*, vol. 100, no. 50, pp. 19512–19517, 1996.

[182] A. M. I. Mezic, "Stability regimes of thin liquid films," *Microscale Thermophysical Engineering*, vol. 2, no. 3, pp. 203–213, 1998.